An Explanation for Anode Voltage Drops in an MPD Thruster

by

Eliahu H. Niewood

S.B., Massachusetts Institute of Technology (1987)
S.M., Massachusetts Institute of Technology (1989)

Submitted to the Department of Aeronautics and Astronautics
in partial fulfillment of the requirements for the degree of

Doctor of Science

at the

MASSACHUSETTS INSTITUTE OF TECHNOLOGY

June 1993

Author .....
Department of Aeronautics and Astronautics
April 27, 1993

Certified by .....
Professor Manuel Martinez-Sanchez, Professor of Aeronautics and Astronautics
Thesis Supervisor

Certified by .....
Professor Mark Drela, Associate Professor of Aeronautics and Astronautics

Certified by .....
Professor Daniel E. Hastings, Professor of Aeronautics and Astronautics

Certified by .....
Professor Leon Trilling, Professor of Aeronautics and Astronautics

Accepted by .....
Professor Harold Y. Wachman
Chairman, Departmental Graduate Committee

An Explanation for Anode Voltage Drops in an MPD Thruster

by

Eliahu H. Niewood

Submitted to the Department of Aeronautics and Astronautics
on April 27, 1993, in partial fulfillment of the
requirements for the degree of
Doctor of Science

Abstract

A theory to explain the cause and predict the magnitude of near anode voltage drops in magnetoplasmadynamic thrusters has been developed. According to this theory, voltage drops arise because the Hall effect leads to axial current. This axial current interacts with the azimuthal magnetic field to produce a radial Lorentz force which pushes the plasma away from the anode. Anode starvation increases the Hall parameter, increasing the axial current.

This theory is examined using a numerical simulation of an MPD thruster. The simulation is axisymmetric and three fluid, having separate equations for ion and neutral continuity and momentum and heavy species and electron energy. The various quantities are coupled using non-equilibrium source terms for ionization, recombination, and elastic and inelastic collisional momentum and energy coupling. The simulation also includes an equation for the magnetic field as well as source terms for Ohmic dissipation and Lorentz force. The simulation predicts near anode voltage drops which show good agreement with experimental data. Total voltage predictions also agree well with experiment at the higher current levels simulated.

Thesis Supervisor: Professor Manuel Martinez-Sanchez
Title: Professor of Aeronautics and Astronautics

Contents

List of Figures

Acknowledgements

Perhaps the best part of my six years as a graduate student is the people I have been privileged to work for and with. Foremost among these people has been my advisor, Professor Manuel Martinez-Sanchez. He has taught me not only physics and engineering, but also, more importantly, how to do research. He has given me the freedom to choose my own path and make my own mistakes but has always been there to help me get back on the right track. As this research is a product of my work, I, as an engineer, am a product of his work. Professor Daniel Hastings has also been an example and a source of knowledge for me. His insights into both the physics and politics of aerospace engineering have been as invaluable to me as the computer resources he has provided. I would like to thank Professors Leon Trilling and Mark Drela for sitting through so many committee meetings and exams and staying awake enough to provide helpful comments. Professor Judson Baron took the time to read a draft carefully and make many helpful suggestions.

If I been sitting in an office alone these past years without officemates and friends, I would not have made it to this point. Rodger Biasca put up with endless questions about computers, numerics, and fluid dynamics, and answered them all with patience and friendship. Scott Miller, whose work often paralleled mine, provided a sounding board for ideas about research and various other topics. Knox Millsaps provided daily breaks from work to air his views on various subjects and took me skiing when I really needed to get away. Eric Sheppard was always there to exert a calming influence on me and as a repository of MPD knowledge. Their friendship and support, as well as that of Jackie Auzias de Turenne, Pamela Barry, Pat Chang, Jean-Marc Chanty, John Conger, Nick Gatsonis, Alex Gioulekas, Bob Haimes, Mohanjit Jolly, Jim Kalamas, Chris Lentz, Renee Mong, David Oh, David Rivas, Robie Samanta-Roy, and Ray Segwick have made coming to work every day almost fun. I would also like to thank Roger Myers and Mike Lapointe for helping me to focus on broader issues in MPD research and for their very generous grant of supercomputer time, without which this research might never have been completed.

This work was supported for the last three years by an Air Force Laboratory Graduate Fellowship. Before that, it was supported by a fellowship from the National Science Foundation. Computer time was provided by a grant from the Air Force Office of Scientific Research. The NASA-Lewis Research Center provided many hours of free supercomputer time.

All my work before graduate school was supported by my parents, Harry and Beryl Niewood. They gave me the freedom and the financing to go my own way and find my own niche. Their patience, understanding, and love are gifts I can not repay. I would also like to thank Sylvan and Rhoda Kamens for welcoming me into their family and for their support and love.

This thesis is dedicated to my wife, Joanne.

Nomenclature

An attempt was made to use each symbol to represent only one quantity. However, that left many common quantities represented by meaningless symbols, so some symbols represent two or more quantities and must be understood in context.

a	Sound wave speed.
a_i	Ratio of collision integrals.
A	Collisional momentum transfer term, Channel crossectional area.
b	Impact parameter, Product of rB_θ
B	Magnetic field strength.
c	Random velocity, Source term vector.
$\bar{C}$	Thermal velocity.
D_a	Ambipolar diffusion coefficient.
E	Electric field strength.
E_i	Ionization energy.
f	Transverse fluxes.
F	Particle distribution function.
g	Relative velocity for collision integrals.
G	Jacobian.
h_{t0}	Inlet total enthalpy.
H	Heat flux.
I	Identity matrix.
I	Input total current.
I_{sp}	Specific impulse.
i, j	Grid indices.
J	Current density.
k	Boltzman's constant.
K_{st}	Mass of particles of type s colliding with particles of type t per unit volume per unit time.
L	Channel length.
l	Left eigenvector.

m Molecular weight.

$\dot{m}$ Mass flow.

M Mach number.

n Number of particles per unit volume.

$\dot{n}$ Rate of creation of particles per unit volume per unit time.

P Pressure.

q Species charge per particle, Damping term.

q_i Denominator of viscosity coefficients.

Q Collision cross section.

r Right eigenvector.

R Recombination coefficient.

R_m Magnetic Reynold's number.

S Momentum source term due to viscosity, Saha factor.

$S_{r1,...}$ Grid metrics for viscosity source terms.

$S_{z1,...}$ Grid metrics for viscosity source terms.

T Temperature, Thrust.

U Ion-neutral slip velocity, Variable vector.

V Fluid velocity of species or bulk, Voltage.

$\hat{V}$ Contravariant velocity.

$V1$ Grid metric.

$V2$ Grid metric.

V_b Bohm velocity.

α Ionization fraction.

β Hall parameter.

Γ Coulomb cutoff parameter.

Δ Energy density change due to collisions.

$\Delta r, z$ Radial and axial cell dimensions.

Δt Simulation time step.

Δv Velocity increment for rocket mission.

ϵ_0 Permittivity of vacuum.

Θ Heat conduction coefficient.

κ Energy source term due to heat conduction.

λ Mean free path.

Λ Eigenvalue.

μ_0 Permeability of vacuum.

ν Collision frequency.

Ξ Morozov replacement parameter.

ϖ Variable conductivity for grid calculation.

Π Traceless part of pressure tensor.

ρ Mass density per unit volume.

σ Electrical conductivity.

Σ Total energy.

τ Time scale.

υ Viscosity coefficient.

Υ Symmetric traceless gradient of velocity.

Φ Viscous dissipation function.

χ Scattering angle.

Ω Collision integral.

Note: The subscripts e,n,i, and g refer to electrons, neutrals, ions, and heavy species respectively. When used as subscripts or otherwise, r, θ, and z refer to the coordinate directions in physical space while ξ and η refer to the coordinate directions in computational space. The subscripts I and R refer to ionization and recombination respectively. The subscripts a and c refer to the anode and cathode. Vectors are written in **boldface** type while tensors are written in serif type.

Chapter 1

Introduction

To most people, space propulsion means chemical rocket propulsion, as used in the Apollo missions or on the Space Shuttle. Most of the rocket engines with which we are familiar, from the huge solid rocket boosters strapped to the Space Shuttle to the small hydrazine rocket used to launch the lunar module from the moon, are chemical rockets. However, chemical rockets are best suited for launch from gravitational wells, where the thrust must be greater than the rocket's weight, or when the total velocity increment, or Δv, to be applied to the rocket is relatively small. Although the thrust of these devices is limited only by their mass flow rate, their specific impulse, a measure of the velocity of the fuel as it exits the rocket, is limited by the chemical energy of the fuel. The lower the specific impulse of the engine, the more fuel needed to produce a given amount of thrust or velocity increment. For operations in space, where gravitational forces are much smaller, engines with lower thrust but higher specific impulse can be competitive and even superior to their high thrust chemical cousins, because they require less fuel mass.

1.1 Electric Propulsion

One family of low thrust high specific impulse engines are electric propulsion devices. These devices use electrical power to increase the energy of the fuel, thereby increasing the exit velocity which can be obtained. Of course, a price must be paid for

this increase in specific impulse. The electrical energy used to accelerate the flow must come from somewhere, and in space it can not come from the local electric company. Electric propulsion devices produce low thrust in part because the thrust is proportional to the power available. The amount of power available in space is quite limited. Power generation in space can come from solar cells, nuclear reactors, batteries, or some other means. Typically, low power electric propulsion devices are or would be run off of large arrays of solar cells. Higher power devices can not now be used in space because no power source exists, but someday might be powered by space nuclear reactors such as descendants of the SP-100.

There are basically three types of electric propulsion, distinguished by how they add electrical energy to the fuel. Electrothermal devices, such as arcjets, add energy to the fuel by heating it. In arcjets, for example, an electric arc is passed through the flowing fuel, ionizing it and heating it to temperatures on the order of a few thousand degrees K. The fuel is then expanded in a nozzle, converting the thermal energy to kinetic energy. The maximum temperature of the fuel is limited by the melting temperature of the material used to make the electrodes and the nozzle. This maximum temperature limit places a ceiling on the specific impulse of electrothermal engines. Typical specific impulse for an arcjet is between 500 and 1200 seconds.

Electrostatic devices, such as ion engines, use electric fields to directly accelerate the fuel. In electron bombardment ion engines, ions are created by bombarding the neutral fuel with high energy electrons. The ions then escape from the thruster chamber through a pair of grids at different voltages. The voltage difference between the grids accelerates the ions to high velocities. Outside the thruster, the ion beam is neutralized. The ions can be accelerated to extremely high velocities, leading to very large specific impulse ratings. The main drawback to ion engines is that the power density of the exhaust is limited by space charge effects as given by the Child-Langmuir law. This limits the thrust that can be produced by a given size device. Hall thrusters, another electrostatic device, are of increasing interest because they are not space charge limited. These devices have been used extensively in space by the former Soviet Union. Neutrals are injected into a chamber open to vacuum at one end

and with an anode at the other end. The chamber walls are formed by insulators and a cathode is placed outside the chamber near the exit. The ions are accelerated out the open end of the channel while the electrons corkscrew back towards the anode. Specific impulse for these devices range up to 2000 sec.

Finally, electromagnetic devices, such as magnetoplasmadynamic (MPD) thrusters, the subject of this thesis, use electric and magnetic forces to add energy to the propulsive fluid. The specific impulse of MPD thrusters falls between that of arcjets and ion engines, but they can produce more thrust than either of these other thrusters.

1.2 Basics of MPD Thrusters

In thirty words or less, MPD thrusters work by accelerating the fuel, an ionized gas, using the Lorentz force due to the current created by applying an electric field across the plasma flow. A typical MPD device is shown in Figure 1-1. The actual hardware of the device is quite simple, consisting of a pair of electrodes, usually in the form of concentric cylinders, with some type of injector to allow gas into the channel formed by the electrodes. Probably the most complicated part of the device is the electrical circuit which carries current to the anode and takes it from the cathode. This current is primarily carried across the channel by the plasma electrons. The moving electrons and ions create a magnetic field perpendicular to the plasma flow. In the self field devices studied in this research, this is the only magnetic field. In applied field devices additional magnetic field is supplied by external currents or magnets. The Lorentz force, perpendicular to both the current and the magnetic field, pushes the electrons and ions in the thruster's axial direction. The ions collide with the neutral particles and push them in the same direction, leading to bulk acceleration of the plasma in the axial direction.

This simple explanation perhaps underplays the complex physics which govern the MPD flow. MPD thrusters seem to sit at the cross roads of many disciplines and limits. Because of their highly ionized nature, they can not be completely represented by the standard descriptions of compressible fluid mechanics so familiar to

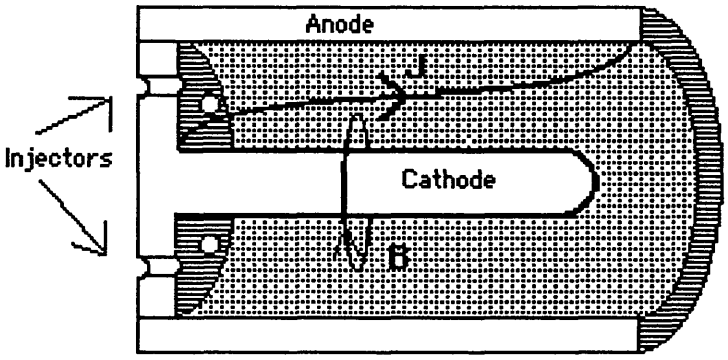

Figure 1-1: Typical MPD Thruster

aerospace engineers. They are highly collisional, and are therefore not tractable to the collisionless approximations of the space plasma scientists and their particle in cell simulations. Compared to the millions of degrees of the plasmas of the fusion community, MPD thrusters are cold, low temperature devices. One must be able to model both the collision of two atomic particles and the bulk flow of 10^{18} particles in order to understand MPD physics.

Because of their theoretical complexity, the bulk of the research into MPD thrusters has been experimental. Experimental devices fall into two main classes, steady and quasi-steady, or pulsed, devices. To steadily produce the megawatts of power used by a high power MPD thruster and to maintain vacuum pressures in the test tank as 4 or more g/s of fuel are being pumped into the tank by the thruster are daunting tasks. Therefore, many tests use quasi-steady devices, where a bank of capacitors supply a pulse of millisecond length and the vacuum tank is large enough to absorb the thruster mass flow for the test duration and stay at low pressure. It is believed, or perhaps hoped, that most aspects of the behavior of these pulsed devices are similar to their steady state cousins. Some thruster characteristics, such as electrode lifetime, can not be studied in this manner. Also, some experimentalists, particularly those who run steady state facilities, maintain that other characteristics of the discharge are also different, such as the current attachment at the cathode. However, direct comparison between the two types of devices has until now been rare, because most

steady state experiments are run at relatively low power and mass flow levels. Also, it is possible that excessive tank pressure levels in some steady state experiments has artificially improved thruster performance.

In spite of all the experiments which have been done, steady and quasi steady, there has been little improvement in the understanding or performance of MPD thrusters since the first experiments were undertaken. Lifetime and efficiency are not in the range needed for space applications of these devices and there are few valid ideas about why the devices perform so poorly or what needs to be done to improve them. Within the last five years however, the theoretical and numerical work being done on MPD thrusters has expanded considerably. Starting from simple one dimensional models with analytical solutions and moving towards quasi one dimensional, two dimensional, and axisymmetric equations with numerical solutions, a number of advances have been made in understanding what controls the physics of these engines. This increased comprehension of MPD physics is leading to the ability to see why thruster performance is poor. Within the next five years it is possible that theoretical work will lead to better thrusters, and that numerical codes will be good enough to assist in improving thruster design.

Of course, what is really necessary is for experiment, theory, and computation to advance hand in hand. No numerical simulation or theory can be trusted until it has been validated against experimental data. Computational solutions are better understood when examined in light of simpler analytical solutions. Numerical solutions help to point out the limits of the validity of the assumptions made to derive analytical solutions. Computational and theoretical results are useful to explain experiments and to design better experiments and better thrusters.

1.3 Thesis Overview

One of the main goals of current MPD research is the development of more efficient thrusters. The efficiency of an MPD thruster is the ratio of the power in the exhaust to the electrical power input to the thruster. Since MPD thrusters are usually run at

constant input current levels, the power input is determined by the potential drop, or voltage difference, between the electrodes. Lower potential drop for the same thrust means higher efficiency.

A number of experiments have shown the existence of substantial voltage drops less than 2 mm from the anode [16, 25, 32, 35, 37]. If a substantial fraction of this voltage drop is not converted to useful work but instead causes heating of the anode, then the efficiency of the device will be decreased. Substantial power fractions into the anode have indeed been measured [16, 19, 20]. Also, thruster efficiency in experiments is significantly below expected levels. These experiments are described in somewhat more detail in Chapter 2 along with other experiments which provide data relevant to this research.

This thesis describes an attempt to use computational methods, along with some analysis, to explain these anode voltage drops and to suggest ways to improve thruster efficiency based on a better understanding of the drops. Computational methods have been applied to one dimensional [31, 38, 41, 42, 45, 50, 53, 60, 68] and two dimensional models [2, 7, 9, 11, 39, 46, 47, 52, 56, 62] of MPD thrusters. These efforts are also discussed in Chapter 2. In general, these numerical simulations yield efficiencies much higher than experimental data and do not show any anode drops or near anode effects.

This thesis explores the possibility that these voltage drops could be due to a starved region near the anode. This starved region has been discussed before by a number of researchers [4, 23, 34, 44, 61]. Starvation occurs because the Hall effect leads to axial current near the anode. The Lorentz force produced by this current pushes the plasma away from the anode, lowering the density there. Because of this low density, the Hall parameter, which is inversely proportional to electron number density, is quite high. Therefore, as the density decreases the axial current increases, pushing more plasma away from the anode. The anode eventually reaches a starved condition where the number density there can be several orders of magnitude lower than in the bulk. The hypothesis of this thesis is that the high axial current and low electron number density combine to produce extremely high radial electric fields, and that these fields occur over a wide enough region to result in large potential drops.

This theory is investigated by using numerical methods to compute a solution to the equations governing the plasma flow in the thruster. An axisymmetric three fluid description of a geometrically simple thruster is used. The model is considered three fluid because it contains separate conservation equations for electron number density and temperature, ion vector momentum, neutral number density and vector momentum, and heavy species energy. A vector form of Ohm's Law is derived based on the electron momentum equations. A magnetic field equation is derived by combining Ohm's Law with Maxwell's equations. The model contains as much, if not more, of the relevant physics as any previous research. The numerical scheme produces convergent solutions at higher power levels than other two dimensional solutions. The governing equations are derived in Chapter 3. Chapter 4 is about the numerical method and boundary conditions used for the two dimensional solutions. Anode models and their use as a boundary condition for the simulation are the subjects of Chapter 5. Chapter 6 describes the anode voltage drops and starvation seen in modeling the CAC thruster of Heimerdinger, Kilfoyle, and Martinez-Sanchez [25]. Chapter 7 describes other phenomena of interest seen in the modeling results. Finally, Chapter 8 describes conclusions and suggestions for future work.

Chapter 2

Existing Research

MPD thruster research has been going on intermittently for almost thirty years. The bulk of the research done has been of an experimental nature. No attempt is made herein to survey all of the experimental work which has appeared. Instead, a number of experiments which are relevant to the question of anode voltage drops are discussed. With regard to theoretical and numerical research, a summary of most of the existing models of anode starvation is presented. Since one of the main contributions of the thesis is an axisymmetric model of the plasma flow in the thruster, a comprehensive survey of one and two thruster models is also presented.

2.1 Experimental Research

There is a large body of experimental work which bears on the problem of anode voltage drops. The experimental work which this research is most closely related to is that of Heimerdinger, Kilfoyle, and Martinez-Sanchez[25, 26, 24, 30]. This work, which was performed in 1987, involved three different cathodes in a thruster 9 cm long with a mass flow of 4 g/s of Argon at currents ranging from 20 to 60 kA. Heimerdinger [25] directly measured the anode voltage drop for his Fully Flared Cathode (FFC) at a number of different current levels at a position 2 mm from the anode. The FFC was made up on a constant diameter anode surrounding a cathode which varied from 0.042 m outer radius at the inelt to 0.053 at the throat to 0.033 at the exit. The

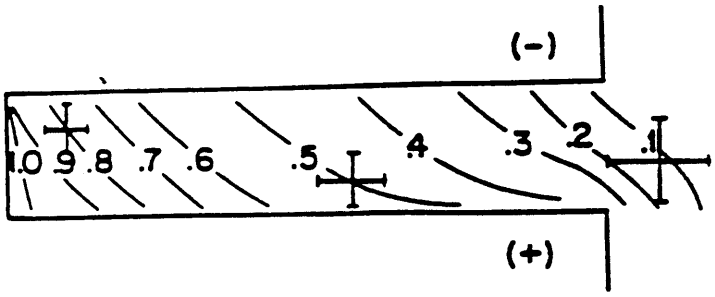

Figure 2-1: Current Lines from Heimerdinger et.al.

voltage drop measurements are shown in Figure 2-2. Heimerdinger also measured the anode voltage drop at 60 kA in the Constant Area Channel (CAC). All of these measurements indicated substantial voltage drops, except for those in the FFC at currents below approximately 25 kA. Contour plots of the constant potential lines are reproduced in Figure 2-3 for the CAC at 60 kA. These reveal that the anode voltage drops are not present near the inlet of the thruster, where the contour lines are spaced relatively evenly in the transverse direction near the thruster inlet. Within a short distance however, the contour lines, and the potential drop, become concentrated near the anode. Plots of the current lines, as shown in Figure 2-1 for the CAC at 60 kA, show that they are inclined slightly in the bulk of the thruster, but near the anode turn sharply until they are almost parallel to the electrode. The geometry of the FFC and CAC, as well as some of the experimental results, are discussed in more detail in Chapter 6.

Perhaps the earliest work to call attention to near anode voltage drops comes from the Soviet Union. Kislov, Morozov, and Tilinin [33] and Kovrov, Morozov, Tokarev,

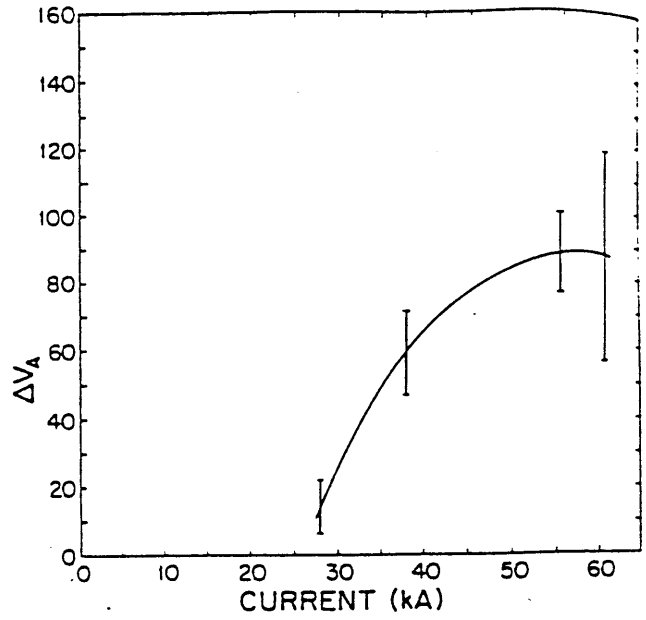

Figure 2-2: Experimental Anode Voltage Drop from Heimerdinger et.al.

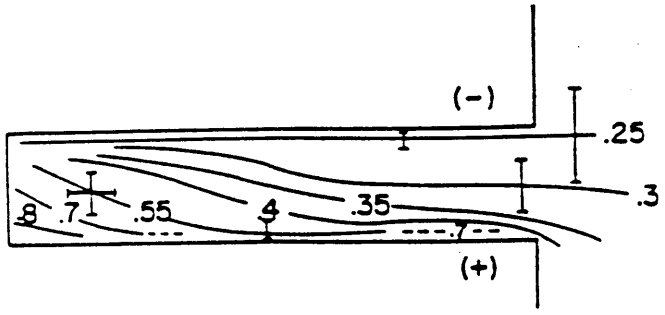

Figure 2-3: Constant Potential Lines from Heimerdinger et.al.

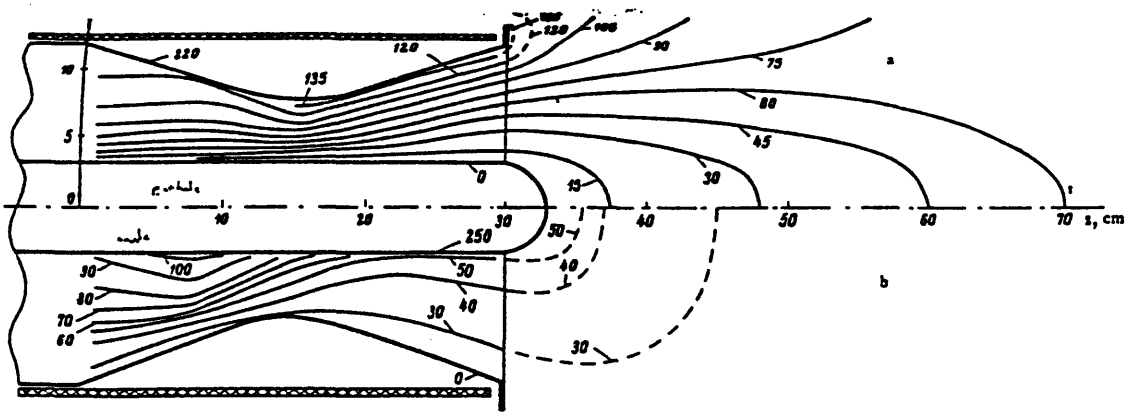

Distribution of the equipotentials $\varphi^* = \text{const}$. a) $V_d = -220$ V, $I_d = 39$ kA, $m = 3$ g/sec; b) $V_d = +250$ V, $I_d = 39$ kA, $m = 3$ g/sec. Values of φ^* are given in volts.

Figure 2-4: Constant Potential Lines from Kislov et.al.

and Shchepkin [35] experimented with a quasi stationary device with electrodes approximately 30 cm in length with the interelectrode gap ranging from about 9 cm at the inlet and exit to abouf 4.5 cm at the throat. Mass flow in the device ranged from 2 to 10 g/sec of nitrogen with current varying from 20 to 50 kA. The device could be run with either the central or the outer electrode as the cathode. Kislov et. al. present a plot of the equipotential lines for both cases while Kovrov et. al. present plots of the current lines. The data show near anode drops of 200 out of 250 total volts with the anode as the central electrode and 100 out of 220 volts with the anode as the outer electrode, as shown in Figure 2-4. Current plots, reproduced in Figure 2-5 show that for both polarities the current is skewed as it approaches part of the anode. Kovrov et. al. report that the constant non-azimuthal components of the magnetic field were zero, which they attribute to the azimuthal symmetry of the time average of the discharge.

Kislov, Kovrov, Morozov, Tilinin, Tokarev, Schepkin, Vinogadova, and Donzov [32] also report on discharges of both hydrogen and nitrogen between coaxial electrodes for current levels between 20 and 60 kA at 3 and 7.5 g/sec. This was also a pulsed experiment, with 2 msec pulses. Kislov plots both current lines and constant potential contours, as shown in Figure 2-6. Again, the current lines turn almost parallel to the electrode surface when they near the anode. The constant potential

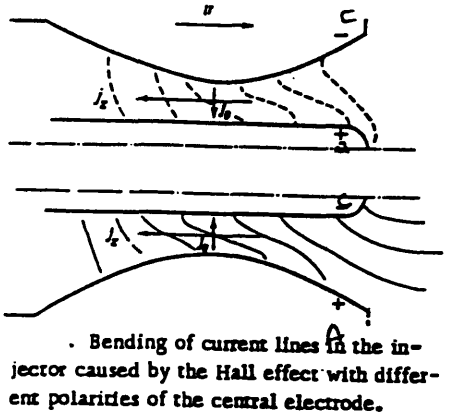

. Bending of current lines in the injector caused by the Hall effect with different polarities of the central electrode.

Figure 2-5: Current Lines from Kovrov et.al.

contours, like those shown by Heimerdinger, are somewhat evenly spaced near the gas inlet but quickly bunch up near the anode. Kislov varied the electrode polarity, using first the inner and then the outer electrode as the anode, but did not find significant variation in the anode "jump" due to this change. Kislov attributes these discharge properties to the Hall effect.

Other Soviet experimental work concerned with anode voltage drops was performed by Grishin[22] and Vainberg[71]. Grishin et. al. studied a lithium fueled steady state device, with mass flows ranging from 10 to 33 mg/sec and currents ranging from 500 to 2500 A. It was found that above some critical current, the voltage increased considerably with increasing current. Above some critical voltage, the electrodes melted and the voltage decreased considerably. The critical current increased with increasing mass flow. Different cathode and anode shapes were studied to determine their effect on both critical parameters. Vainberg et. al. instrumented a similar thruster to directly measure the anode voltage drop. The anode voltage drop, shown in Figure 2-7, was seen to increase considerably with increased current. The voltage drop is negative at low current values and increases to approximately 9 V at 800 A and 6 mg/s while the total voltage increases from 13 V at 550 A to 20 V at 800 A. This result is of particular interest because the experiment was performed under steady state rather than pulsed conditions.

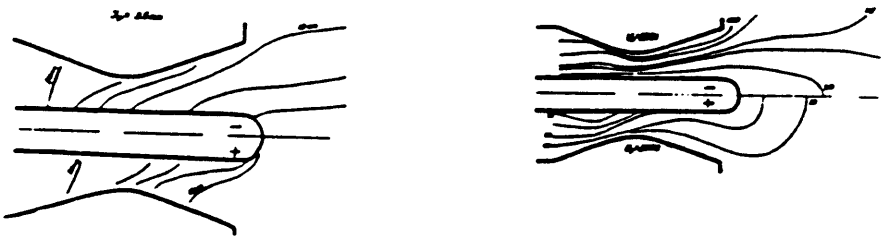

Figure 2-6: Current and Constant Potential Lines from Kislov et.al.

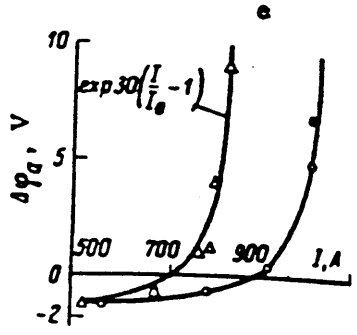

Figure 2-7: Experimental Anode Voltage Drop from Vainberg et.al.

Another interesting experiment is presented by Kuriki, Onishi, and Morimoto[37] for their KIII thruster. This was a quasi-steady thruster run both with and without an applied field of less than 0.15 T. Argon was used as the propellant. This experiment is particularly interesting because two rings of injectors were used, one near the cathode and the other near the anode. The percentage of the mass flow which went through each of the sets of rings was varied from 100% cathode injection to 30% cathode injection. Measurements of total voltage, anode fall voltage, and cathode fall voltage were taken for currents ranging from 4.5 kA up to 10 kA for both mass flow distributions. Mass flows from 0.7 g/s down to 0.12 g/s were used. For 100% cathode injection, anode fall voltages of up to 100 V are seen for total voltage up to 300 V. For 30% cathode injection, anode falls stay below 30 V for all but one of the cases in the test matrix.

The correlation between the electron Hall parameter and the anode potential drop is the subject of recent research by Gallimore[16, 19, 18, 17]. Gallimore measured both the anode fall and the Hall parameter in Princeton University's quasi-steady "full scale benchmark thruster". Current levels from 5 to 25 kA were used with mass flows from 4 to 16 g/s. Gallimore measured anode fall voltages as high as 50 V with total voltages as high as 300 V. Anode power fractions as high as 50% were measured. Electron Hall parameters up to 8 were measured at a distance 2 mm from the anode lip, and the anode fall was seen to scale with the Hall parameter. Measurements of heat flux into the anode using thermocouples showed that most of the power used in the anode fall was absorbed by the anode. Gallimore also discusses the possibility that anode falls may be due to anomalous transport. To this end, measurements of electric field, velocity, and one component of current are presented in order to calculate the conductivity of the plasma. The conductivity is found to differ considerably from the classical Spitzer-Harm value.

2.2 General MPD Models

The amount of theoretical and computational research related to self-field MPD thrusters has increased quite a bit in recent years. Most of this work has concentrated on what will be referred to as general MPD models, models which attempt to reproduce the overall characteristics of a thruster, rather than specialized models, which attempt to understand starvation or microturbulence or cathode erosion, etc. This work ranges from very simple one dimensional models to very complex axisymmetric ones, such as that described in this thesis.

Much of the early theoretical work which has been done consists of solutions to one dimensional models with analytic or ODE techniques. King[31] solved a one dimensional one fluid model. One fluid is used herein to describe models which assume that the plasma is always fully ionized and that the ions and electrons are at the same temperature. King does not include viscosity, heat conduction, or diffusion, and uses a constant electrical conductivity. His research involves two models. The first of these uses the ideal gas law. Because of the assumptions, all of the energy which physically would go into ionizing the working fluid goes, in the model, into heating the fluid, resulting in artificially high temperatures. To redress this problem, a second model is used. This model attempts to include ionization effects by setting the pressure to its equilibrium value for the corresponding density. King also estimates the importance of the Hall effect, but basically concludes that a one dimensional model with a scalar conductivity is adequate. He further demonstrates this by showing good agreement between calculated thrust and radial electric field values and experimental data.

Kuriki, Kunii, and Shimizu[38] also solve a one fluid model. Unlike King, they include area variation but neglect pressure forces and energy conservation. This leads to an algebraic solution for a constant area channel and an eigenvalue problem for variable area channels. They identify boundary layers at the inlet and exit of the channel through which most of the current flows and find that the thickness of these regions is inversely proportional to the magnetic Reynolds number, defined as $R_m = \sigma B_0^2 L \frac{\bar{A}}{\dot{m}}$ where $\bar{A}$ is the average channel area.

Minakuchi and Kuriki[50] solve a one fluid model in a dual stage thruster, with a pair of electrodes followed by insulators followed by a second pair or electrodes. They also include heat conduction in a model of a single stage thruster and use the model to estimate the importance of the Hall effect and anode starvation. However, their use of a one temperature model results in extremely large electron temperatures, on the order of 60,000 K, and unrealistic temperature profiles. This leads to inaccurate profiles of the Hall parameter, and calls into question their analysis of starvation.

Martinez-Sanchez [45] also solves a one fluid one dimensional model in both constant and variable area channels. Martinez-Sanchez shows how the one dimensional flow varies with the magnetic Reynolds number. For low values of the magnetic Reynolds number, Martinez-Sanchez finds fully subsonic solutions. As the magnetic Reynolds number is increased, the flow becomes partly supersonic with an embedded shock, and then fully supersonic. Martinez-Sanchez also discusses the importance of pressure forces and the effects of convergent-divergent channels. Good comparison is shown to both thrust and voltage data from experiment, although a large electrode potential drop is assumed for the numerical voltage calculation.

Lawless and Subramaniam[41] describe a one fluid model similar to that solved by King. Their paper is mainly concerned with describing the choking condition at the sonic point, and its importance in their back-EMF theory of onset. The effect of variable ionization on the choking condition and back-EMF is also briefly considered. Variable ionization is discussed at greater length in a later paper[68], which also presents axial profiles of ionization fraction, current density, velocity and temperature. The ionization model used is that of Mansbach and Keck. Although ionizational non-equilibrium is included, thermal equilibrium is assumed. This paper also discusses the effect of heat conduction and viscous forces on the choking condition. More recently, Lefever-Button and Subramaniam [42] extended the model further by including variable area channels. They present plots of ionization fraction, temperature, current density, and magnetic field for different expansion ratios and mass flow values. They also compare computed thrust to experimentally obtained values, with good agreement.

Niewood[53, 55] solves a two fluid one dimensional model, again in both constant and variable area channels. Two fluid is used herein to indicate that the model differentiates between the electron and the heavy species temperatures. The ionization fraction is controlled by a rate equation using the Hinnov-Hershberg model for ionization and recombination rates. Elastic transfer between electrons and ions, axial electron heat conduction, variable conductivity, ion-neutral velocity slip, and ad hoc models of ambipolar diffusion and viscosity are all included. Finite difference techniques are used to solve a set of unsteady equations, rather than the Runge-Kutta type schemes used to solve the steady equations in all of the research described above. Good comparison to thrust data is shown, but voltage predictions do not mimic experimental data.

Another two temperature finite rate ionization model is described by Shoji and Kimura[60]. Their model is similar to that of Niewood but does not include ambipolar diffusion, viscosity, heat conduction, or collisional energy transfer between electrons and heavy particles. It does however examine both hydrogen and argon as propellants. The ionization model used is again that of Mansbach and Keck. Results for both propellants are shown at conditions representing electrothermal and electromagnetic regimes of operation.

In summary, quite a few one dimensional models have been developed. The advantages presented by these models are that they are relatively fast and computationally cheap ways to obtain approximations to MPD flows. They produce fairly accurate predictions of thrust and of some flow parameters. They are also helpful in understanding the importance of scaling parameters such as the magnetic Reynold's number and evaluating the effect of including or neglecting various aspects of thruster physics, such as velocity slip or ionizational non-equilibrium. The limitations of these models stem, of course, from their one dimensionality. The Hall effect can not be represented in any meaningful way. Radial heat conduction, viscosity, and velocity slip can be treated, at best, in an ad hoc fashion. Complex thruster geometries are also not faithfully reproduced. Perhaps for these reason, thruster efficiency is not correctly predicted. These limitations can only be addressed by multi dimensional

models.

Fortunately, two dimensional MPD models have also been solved, using numerical techniques such as finite differences and finite volumes. The earliest example of this avenue of research is probably that of Morozov et al.[52]. The model used assumes full ionization everywhere and constant temperature for both ions and electrons. The Hall effect is introduced via a constant exchange parameter $\Xi = \frac{m_i I}{e\dot{m}}$. For $\Xi = 0$, no Hall effect, the solution is stable. At some critical value of Ξ the flow, or the numerical method, becomes unstable. The flow loses its stability near the anode because of an "unlimited increase in the current density". For those cases with Hall effect in which stable solutions were found, the current lines are seen to be substantially skewed near the anode, pressing the plasma against the cathode.

This early Russian work is described more fully by Brushlinskii and Morozov[7]. This article reviews a number of one and two dimensional analytical and numerical solutions of MPD models, mostly from the late 1960's, mostly in Russian papers. The article starts off by describing a general two fluid MPD model and then describing assumptions which can be made to simplify the model. All of the solutions given are for one fluid models, except for one set of quasi one dimensional results which assume some thin ionization front on the upstream side of which ionization is negligible and with fully ionized plasma on the downstream side. Two dimensional models with infinite conductivity and no Hall effect, finite conductivity and no Hall effect, and finite conductivity with Hall effect are discussed and some solutions are presented. The finite conductivity models assume that the plasma is isothermal. As in earlier Russian papers, the existence of anode voltage drops and "current bridges" and the instability of the code in the presence of these effects are noted.

The Soviet work is the only two dimensional numerical work to appear before the mid-1980's. Then, a number of Western researchers began to use numerical methods to solve two dimensional fluid models. The first work to appear was that of Ao and Fujiwara[2]. Their model was axisymmetric and one fluid. Heat conduction was included. The electrical conductivity is set to a constant value as presumably is the Hall parameter, although the latter is unclear from their paper. Also unclear from

their paper are the boundary conditions, particularly for the magnetic field, at the electrodes.

The next work to be done was that of Park and Choi[56]. Their model was one fluid but two dimensional, rather than axisymmetric. The electrical conductivity is again assumed to be constant and all other transport effects are neglected. The Hall effect is included by assuming a constant Hall parameter which modifies the electrical conductivity. Results show concentration of the current at the anode tip and pinching of the plasma at the cathode.

Another numerical effort from around the same time was undertaken at M.I.T. by Chanty and Martinez-Sanchez[11, 12]. Their model, one fluid and axisymmetric, assumed constant temperature and electrical conductivity. Viscosity is neglected, as well as the electron pressure term in Ohm's Law. The parallel electric field is set to zero at the electrodes. Results are obtained for currents up to 10 kA at a mass flow of 6 g/s.

Perhaps the most extensive numerical effort outside the Soviet Union comes from the University of Stuttgart. A number of different models have been solved there by Sleziona, Auweter-Kurtz, Schrade, and Wegmann[3, 62, 63, 66, 64, 65]. Much of their work centers around extension of a packaged code, EUFLEX, to include additional equations and source terms and for cylindrical geometries. The latest incarnation of the Stuttgart model includes separate heavy and electron temperatures, equilibrium ionization, electron and heavy species heat conduction, and viscous transport. Results are shown for both the cylindrical and nozzle type thrusters experimented with at Stuttgart. These steady state devices run at relatively low power. Simulations for the nozzle type thruster are run at massflows of 0.8 g/s and up to 3 kA. The cylindrical thruster simulations are run at up to 12 kA and 2 g/s. No skewing of the current lines is seen even at the highest current levels. Electron temperatures of up to 5 eV are seen along with fourth ionized Argon.

Miller and Martinez-Sanchez[47, 48, 49] investigated the importance of transport, electron and heavy species heat conduction, viscosity, and ambipolar diffusion, in MPD thrusters. Their early work used an assumed magnetic field distribution, but

later work included a self consistent magnetic field equation which neglected the Hall effect and electron pressure terms in Ohm's law. Their results show the boundary layers to grow to fill the channel and the heavy species temperature to be substantially raised by viscous effects, in the relatively long and narrow channels which they examine. However, because the Hall effect is not included, skewing of the current is not seen and no anode voltage drops are seen.

Another recent two dimensional model is that developed by LaPointe[39, 40] at NASA's Lewis Research Center. In his early work Lapointe solves a single temperature, fully ionized axisymmetric model in complex geometries. Later work includes separate electron and heavy species energy equations. The equations are developed to include an applied magnetic field, but the papers describe only self field cases. Both viscosity and heat conduction are included in the model. Comparisons are made to a number of experimental geometries, including the University of Stuttgart ZT-1 thruster and the Princeton University half scale flared anode and extended thrusters. The Stuttgart thruster was modeled at 6 kA and 6 g/s of Argon with two different anode geometries. The Princeton extended anode thruster was modeled at a mass flow of 1 g/s for currents up to 4 kA. Instability of the numerical code is compared to onset with good agreement.

Caldo, Choueiri, Kelly, and Jahn [9, 10] have developed a numerical simulation which includes much of the physics found in earlier versions of this research as well as a model for anomalous transport due to plasma microinstabilities. Caldo uses a two fluid model incorporating nonequilibrium ionization, electron-heavy species thermal nonequilibrium, and electron and heavy species heat conduction. Additional ion heating and electron-ion collisions are included due to anomalous effects. Results are obtained for currents up to 18 kA at a mass flow of 6 g/s. Results are shown for cases with and without anomalous transport. Heavy species temperature is increased considerably by anomalous effects, from 10,000K up to 23,000K. Efficiency is decreased somewhat, but mostly because thrust is decreased. Plasma fall voltage increases only slightly due to anomalous effects.

Mikelides, Turchi, and Roderick [46] have begun work on adapting the MACH2

code for use with MPD thrusters. Current work assumes full ionization and a single temperature. The code is used to simulate an applied field thruster being tested at the NASA Lewis Research Center. Both self field and applied field cases have been simulated at a mass flow of 0.1 g/s and a current of 1 kA. So far steady state conditions have been reached only for very low applied field cases.

2.3 Anode Starvation Models

A number of theoretical efforts have been aimed at understanding and predicting anode starvation. Most of these efforts attempted to link anode starvation with "onset", the inititiation of large oscillations in the total thruster voltage.

The three earliest efforts in this direction all come from the Soviet Union. The standard model of starvation is probably that of Bakhst, Moizhes, and Rybakov[4]. Bakhst assumes that the radial current at the electrode equals the local random electron flux to the electrode. Using Ohm's law and the radial momentum balance Bakhst derives an analytic expression for the local number density near the anode. Bakhst's model will be discussed in more detail in Chapter 5.

Korsun [34] assumes that the plasma is injected at the base of the cathode. He then derives an expression for the radial expansion of the injected jet as it travels the length of the accelerator. Korsun finds that the growth of the jet decreases with increasing currents. As the current is increased, the jet is in contact with the anode over a smaller length of the anode, and the anode current density increases. Korsun defines the limiting current as the lowest current for which the jet does not grow to reach the anode by the end of the thruster.

Shubin [61] assumes that the plasma near the anode becomes unstable to microscopic instabilities when the drift velocity of the electrons becomes greater than some critical speed, about the ion sonic speed. To determine when this happens he analytically solves a system of equations made up of an axial momentum balance and the two scalar Ohm's law equations with the radial current neglected, along with a stream function for the mass flux. Shubin derives an equation for the number density

and the current, and uses these to determine when the drift speed will be greater than the critical speed. Shubin believes that the resulting microinstabilities are the cause of onset. Although not really a model of anode starvation, onset occurs in this theory either when the plasma density grows small, i.e. when the anode becomes starved, or when the axial current grows very large. Since the axial current in Shubin's theory is inversely proportional to the number density, this second cause of instability is also due to anode starvation.

Perhaps the first explicit connection between anode falls and starvation in Western literature was made by Hugel [29]. Hugel measured anode falls in a nozzle-type MPD thruster and found them to be small or negative at low currents and then to increase dramatically above some critical current. Hugel also presents data showing that the pressure near the anode is an order of magnitude lower than at the center of the flow and that the pressure at the anode wall decreases with increasing current. Hugel mentions a computational solution which also shows low pressure and number density near the anode. He then goes on to connect the anode voltage drop with the depletion of charge carriers near the anode. If the thermal electron current is too small to carry the local current density then a fall voltage must be created to carry more current.

An extended form of Bakhst's model is developed by Heimerdinger [23]. Heimerdinger's equations include ion-neutral slip, non-equilibrium ionization, heat conduction, and variable transport coefficients. He uses slender channel approximations to separate the governing equations into axial and transverse equations. The resulting set of ordinary differential equations are then solved by computer. Like Bakhst, he finds a critical current above which there are not enough electrons to carry current to the anode. Heimerdinger shows relatively high total potential, but does not show transverse plots of the potential drop.

Martinez-Sanchez[44] generalizes the theory of Bakhst to conditions below "onset", or the critical current at which the electron thermal current is less than the local current density. He does this by allowing a negative anode potential drop to develop and reduce the thermal electron flux to the anode. Martinez-Sanchez can then solve for the necessary anode drop at various total currents below the critical

current. He finds that this voltage drop is negative up to very near onset, and then quickly approaches zero or changes sign.

2.4 Other Voltage Drop Theories

Many of the starvation theories described above essentially explain anode voltage drops as a sheath effect. When the anode becomes starved, the local current density is greater than the random electron flux to the wall. In order to attract more electrons to the wall, a positive voltage drop must develop. Gallimore [17] goes somewhat further. He assumes a sheath thickness, local current density, and charged particle density outside the sheath. The resulting voltage drops are on the same order as those that he finds experimentally. Although reasonable sheath widths are assumed, the magnitude of the voltage drop is very sensitive to the width, so this model is somewhat incomplete.

Researchers at Princeton University, particularly Choueiri[13], Gallimore [17], and Caldo[9], have suggested that plasma microturbulence could lead to substantially lower electrical conductivity than the classical values. This would, in turn, cause greater Ohmic drops in the plasma. Caldo, Choueiri, Kelly, and Jahn [10] have shown that anomalous transport can lead to increased voltage and decreased efficiency, but they do not say whether this is due to increased anode voltage drops. Also, Caldo's numerical results still show efficiencies substantially higher than experimental results.

Chapter 3

Governing Equations

The ideal simulation of an MPD thruster would follow each of the 10^{21} particles per m^3 in its three dimensional motion about the three dimensional geometry of the thruster. However, solutions to such a model are not conceivable at the present time, nor in the foreseeable future. Therefore, simplifications are necessary. The governing equations used in this research incorporate a number of assumptions. The plasma is assumed to be quasi-neutral, and is described using fluid equations. The geometry is assumed to be cylindrical, with no variation in the azimuthal direction. The magnetic field is assumed to be confined to the azimuthal direction. The electric field, the current, and the velocity all have components in both in plane directions. The plasma is treated as being out of equilibrium, in that the electron and heavy species temperatures are treated separately and coupled only by elastic collisional energy transfer, the ionization fraction is not determined by Saha equilibrium, but by balancing ion flow with ionization and recombination collisions, and the ion and neutral velocities are coupled only by collisional drag.

Incorporating these assumptions yields a model consisting of nine partial differential equations. There are eight differential equations for the fluid variables and one for the magnetic field. Sections 3.1 - 3.4 describe the derivation of these equations. Section 3.5 describes the derivation of the transport properties. The ionization model is discussed in Section 3.6. Performance calculations are the subject of Section 3.7.

3.1 Continuity Equations

The model includes two continuity equations, a neutral and an ion density equation. Both equations are derived by starting from the mass density equations for the individual species making up the plasma. The general continuity equation for any species is given by[5]

$$\frac{\partial n_s}{\partial t} + \nabla \cdot (n_s \mathbf{V}_s) = \dot{n}_s, \tag{3.1}$$

where $\dot{n}_s$ represents the local creation or loss rate of the species. Expanding the divergence operator for cylindrical geometries yields the scalar form of this equation,

$$\frac{\partial n_s}{\partial t} + \frac{1}{r}\frac{\partial}{\partial r}(r n_s V_{sr}) + \frac{\partial}{\partial z}(n_s V_{sz}) = \dot{n}_s. \tag{3.2}$$

This equation is further rearranged for implementation in the numerical scheme as

$$\frac{\partial n_s}{\partial t} + \frac{\partial}{\partial r}(n_s V_{sr}) + \frac{\partial}{\partial z}(n_s V_{sz}) = \dot{n}_s - \frac{n_s V_{sr}}{r}. \tag{3.3}$$

The three species considered in this model are neutral Argon atoms, Argon ions, and electrons. Creation or loss of these species is assumed to take place due to either ionization or recombination collisions only. Therefore, the three species equations are

$$\frac{\partial n_e}{\partial t} + \frac{\partial (n_e V_{er})}{\partial r} + \frac{\partial (n_e V_{ez})}{\partial z} = -\dot{n}_{eR} + \dot{n}_{eI} - \frac{n_e V_{er}}{r}, \tag{3.4}$$

$$\frac{\partial n_e}{\partial t} + \frac{\partial (n_e V_{ir})}{\partial r} + \frac{\partial (n_e V_{iz})}{\partial z} = -\dot{n}_{eR} + \dot{n}_{eI} - \frac{n_e V_{ir}}{r}, \tag{3.5}$$

and

$$\frac{\partial n_n}{\partial t} + \frac{\partial (n_n V_{nr})}{\partial r} + \frac{\partial (n_n V_{nz})}{\partial z} = -\dot{n}_{eI} + \dot{n}_{eR} - \frac{n_n V_{nr}}{r}. \tag{3.6}$$

where $\dot{n}_{eR}$ represents the number of recombination events, each producing one neutral and one electron from two electrons and one ion, and $\dot{n}_{eI}$ represents the number of ionization events, each producing two electrons and one ion from a neutral and an electron. As mentioned above, the plasma is assumed to be quasi-neutral, so that n_e

is used in place of n_i. It is useful to define the global density,

$$\rho = m_e n_e + m_i n_e + m_n n_n \approx m_n(n_e + n_n).$$

It is convenient to define the global velocity, the current, and the slip velocity, where, respectively,

$$\mathbf{V} = \frac{m_e n_e \mathbf{V}_e + m_i n_e \mathbf{V}_i + m_n n_n \mathbf{V}_n}{\rho} \approx \alpha V_i + (1-\alpha) V_n$$

with $\alpha = \frac{n_e}{n_e + n_n}$,

$$\mathbf{J} = -e n_e (\mathbf{V}_e - \mathbf{V}_i)$$

$$\mathbf{U} = \mathbf{V}_i - \mathbf{V}_n.$$

The individual species velocities can then be written as

$$\mathbf{V}_e = \mathbf{V} - \frac{\mathbf{J}}{e n_e} + (1-\alpha)\mathbf{U}, \tag{3.7}$$

$$\mathbf{V}_i = \mathbf{V} + (1-\alpha)\mathbf{U}, \tag{3.8}$$

and

$$\mathbf{V}_n = \mathbf{V} - \alpha \mathbf{U}. \tag{3.9}$$

where terms of order $\frac{m_e}{m_i}$ have been neglected.

In order to obtain the global continuity equation, each of the three species equations is multiplied by the corresponding mass and the three equations are then summed. Since no mass is created or lost, the resulting equation is relatively simple,

$$\frac{\partial \rho}{\partial t} + \frac{\partial}{\partial r}(\rho V_r) + \frac{\partial}{\partial z}(\rho V_z) = -\frac{\rho V_r}{r}. \tag{3.10}$$

With the assumption of quasi-neutrality, any combination of two independent continuity equations, such as the ion and neutral species continuity equations, are enough to specify all of the densities.

3.2 Momentum Equations

The set of governing equations includes six momentum equations, one for the momentum of each species in each of the two directions, axial and transverse. Again, the derivation starts from the vector form of the individual species momentum equation[5]

$$n_s m_s \left[\frac{\partial \mathbf{V}_s}{\partial t} + (\mathbf{V}_s \cdot \nabla)\mathbf{V}_s \right] + \nabla \cdot \mathsf{P}_s = n_s q_s (\mathbf{E} + \mathbf{V}_s \times \mathbf{B}) + \mathbf{A}_s - m_s \dot{n}_s \mathbf{V}_s \quad (3.11)$$

where $\mathbf{A}_s$ represents the momentum gained or lost by the species in elastic and inelastic collisions. Adding the species continuity equation multiplied by $m_s \mathbf{V}_s$,

$$\frac{\partial}{\partial t}(n_s m_s \mathbf{V}_s) + \nabla \cdot (n_s m_s \mathbf{V}_s \mathbf{V}_s) + \nabla \cdot \mathsf{P}_s = n_s q_s (\mathbf{E} + \mathbf{V}_s \times \mathbf{B}) + \mathbf{A}_s \quad (3.12)$$

The pressure tensor is split into two parts

$$\mathsf{P}_s = P_s \mathsf{I} - \Pi_s$$

where Π is the viscous stress term, so that

$$\nabla \cdot \mathsf{P}_s = \nabla \cdot (P_s \mathsf{I}) - \nabla \cdot \Pi_s = P_s(\nabla \cdot \mathsf{I}) + (\nabla P_s) \cdot \mathsf{I} - \nabla \cdot \Pi_s = \nabla P_s - \nabla \cdot \Pi_s.$$

Expanding the vector operators yields two equations, the transverse momentum equation

$$\frac{\partial (n_s m_s V_{sr})}{\partial t} + \frac{\partial (n_s m_s V_{sr}^2 + P_s)}{\partial r} + \frac{\partial (n_s V_{sr} V_{sz})}{\partial z} = n_s q_s (E_r - V_{sz} B_\theta)$$

$$+ A_{sr} - \frac{n_s m_s V_{sr}^2}{r} + \frac{1}{r}\frac{\partial r \Pi_{srr}}{\partial r} + \frac{\partial \Pi_{srz}}{\partial z} - \frac{\Pi_{s\theta\theta}}{r} \quad (3.13)$$

and the axial momentum equation,

$$\frac{\partial (n_s m_s V_{sz})}{\partial t} + \frac{\partial (n_s m_s V_{sr} V_{sz})}{\partial r} + \frac{\partial (n_s V_{sz}^2 + P_s)}{\partial z} = n_s q_s (E_z + V_{sr} B_\theta)$$

$$+ A_{sz} - \frac{n_s m_s V_{sr} V_{sz}}{r} + \frac{1}{r}\frac{\partial r \Pi_{srz}}{\partial r} + \frac{\partial \Pi_{szz}}{\partial z}. \tag{3.14}$$

The state equation for each species is assumed to be given by

$$P_s = n_s k T_s. \tag{3.15}$$

From Burgers[8], the collision term for each species is given by

$$\mathbf{A}_s = \sum_t [K_{st}(\mathbf{V}_t - \mathbf{V}_s) - m_s \dot{n}_s^-(\mathbf{V}_s + \mathbf{c}_s^-) + m_s \dot{n}_s^+(\mathbf{V}_s + \mathbf{c}_s^+)]. \tag{3.16}$$

where

$$K_{st} = n_s m_{st} \nu_{st} = K_{ts}$$

$$m_{st}^{-1} = m_s^{-1} + m_t^{-1}$$

and

$$\nu_{st} = n_t \bar{C}_{st} Q_{st}.$$

The only reactions which are considered are ionization and recombination which will be described by

$$A + e^- \rightleftharpoons A^+ + e^- + e^-$$

From Burgers, the inelastic collision velocities $\mathbf{c}_s^{-,+}$ are given by

$$\mathbf{c}_s^{-,+} = \int F_s^{-,+} \mathbf{c}_s dc_s \tag{3.17}$$

where F_s^- is the distribution function in velocity space of particles of type s which are lost in inelastic collisions normalized by the number of particles of type s colliding and F_s^+ is the normalized distribution function of particles of type s created in these collisions. The velocity $\mathbf{c}_s$ is defined with respect to the mean velocity of the species. For simplicity, it is assumed that all particles are equally likely to partake in an inelastic collision. This is a reasonable assumption for both neutrals and ions, which do not have any threshold energy to participate in an inelastic collision. It is a

poor assumption for the electrons, which must be above the ionization energy to be involved in ionization. However, the electron inelastic collision velocity drops out of the final equations because of the small electron mass, so the assumption is good enough. With this assumption, the collision velocity for particles disappearing in an inelastic collision is just the average thermal velocity of that species, which is zero by definition. So,

$$\mathbf{c}_i^- = \mathbf{c}_e^- = \mathbf{c}_n^- = 0 \tag{3.18}$$

However, particles which are created in collisions are created at the mean velocity of the particle that they were created from. Therefore,

$$\mathbf{c}_{sh}^+ = \int F_t(c_t) c_{sh} d\mathbf{c}_s = \int F_t(c_t)(c_{th} + V_{th} - V_{sh}) d\mathbf{c}_t = V_{th} - V_{sh} \tag{3.19}$$

where the subscript t represent the type of particle which is lost in the equation which creates the particle of type s, and h is an index for the direction. So,

$$\mathbf{c}_i^+ = \mathbf{V}_n - \mathbf{V}_i = -\mathbf{U} \tag{3.20}$$

$$\mathbf{c}_e^+ = \mathbf{V}_n - \mathbf{V}_e \tag{3.21}$$

$$\mathbf{c}_n^+ = \mathbf{V}_i - \mathbf{V}_n = \mathbf{U} \tag{3.22}$$

Therefore, the neutral momentum equations are

$$\frac{\partial(n_n m_n V_{nr})}{\partial t} + \frac{\partial(n_n m_n V_{nr}^2 + P_n)}{\partial r} + \frac{\partial(n_n m_n V_{nr} V_{nz})}{\partial z} = S_{nnr} + S_{nir}$$

$$+ K_{ni}(V_{ir} - V_{nr}) + K_{ne}(V_{er} - V_{nr}) - \dot{n}_{eI} m_n V_{nr} + \dot{n}_{eR} m_n V_{ir} - \frac{n_n m_n V_{nr}^2}{r} \tag{3.23}$$

and

$$\frac{\partial(n_n m_n V_{nz})}{\partial t} + \frac{\partial(n_n m_n V_{nr} V_{nz})}{\partial r} + \frac{\partial(n_n m_n V_{nz}^2 + P_n)}{\partial z} = S_{nnz} + S_{niz}$$

$$+ K_{ni}(V_{iz} - V_{nz}) + K_{ne}(V_{ez} - V_{nz}) - \dot{n}_{eI} m_n V_{nz} + \dot{n}_{eR} m_n V_{iz} - \frac{n_n m_n V_{nr} V_{nz}}{r} \tag{3.24}$$

where S_{ntr} and S_{ntz} represent the viscous terms in the species momentum equation

given above. The ion momentum equations become

$$\frac{\partial(n_e m_i V_{ir})}{\partial t} + \frac{\partial(n_e m_i V_{ir}^2 + P_i)}{\partial r} + \frac{\partial(n_e m_i V_{ir} V_{iz})}{\partial z} = n_e e(E_r - V_{iz} B_\theta) + S_{iir} + S_{inr}$$

$$+ K_{in}(V_{nr} - V_{ir}) + K_{ie}(V_{er} - V_{ir}) + \dot{n}_{eI} m_i V_{nr} - \dot{n}_{eR} m_i V_{ir} - \frac{n_e m_i V_{ir}^2}{r} \qquad (3.25)$$

and

$$\frac{\partial(n_e m_i V_{iz})}{\partial t} + \frac{\partial(n_e m_i V_{ir} V_{iz})}{\partial r} + \frac{\partial(n_e m_i V_{iz}^2 + P_i)}{\partial z} = n_e e(E_z + V_{ir} B_\theta) + S_{iiz} + S_{inz}$$

$$+ K_{in}(V_{nz} - V_{iz}) + K_{ie}(V_{ez} - V_{iz}) + \dot{n}_{eI} m_i V_{nz} - \dot{n}_{eR} m_i V_{iz} - \frac{n_e m_i V_{ir} V_{iz}}{r}. \qquad (3.26)$$

In the electron momentum equations terms which are multiplied by the electron mass can be neglected. Terms multiplied by the square root of the electron mass, in particular the drag terms, are retained. Having done this,

$$\frac{\partial P_e}{\partial r} = -n_e e(E_r - V_{ez} B_\theta) + K_{ei}(V_{ir} - V_{er}) + K_{en}(V_{nr} - V_{er}) \qquad (3.27)$$

$$\frac{\partial P_e}{\partial z} = -n_e e(E_z + V_{er} B_\theta) + K_{ei}(V_{iz} - V_{ez}) + K_{en}(V_{nz} - V_{ez}) \qquad (3.28)$$

Substituting for the electron velocity, and using

$$\sigma = \frac{e^2 n_e}{m_e(\nu_{ei} + \nu_{en})}$$

yields

$$E_r = V_{iz} B_\theta - \frac{1}{e n_e}(J_z B_\theta + \frac{\partial P_e}{\partial r} - K_{en} U_r) + \frac{J_r}{\sigma} \qquad (3.29)$$

$$E_z = -V_{ir} B_\theta - \frac{1}{e n_e}(-J_r B_\theta + \frac{\partial P_e}{\partial z} - K_{en} U_z) + \frac{J_z}{\sigma} \qquad (3.30)$$

These equations are a form of Ohm's law generalized for velocity slip. They can be used to replace the electric field term in the ion momentum equation. Doing this

yields the ambipolar momentum equations

$$\frac{\partial(n_e m_i V_{ir})}{\partial t} + \frac{\partial(n_e m_i V_{ir}^2 + P_i + P_e)}{\partial r} + \frac{\partial(n_e m_i V_{ir} V_{iz})}{\partial z} = -J_z B_\theta + S_{iir} + S_{inr}$$

$$+ K_{in}(V_{nr} - V_{ir}) + K_{en}(V_{nr} - V_{er}) + \dot{n}_{eI} m_i V_{nr} - \dot{n}_{eR} m_i V_{ir} - \frac{n_e m_i V_{ir}^2}{r} \qquad (3.31)$$

and

$$\frac{\partial(n_e m_i V_{iz})}{\partial t} + \frac{\partial(n_e m_i V_{ir} V_{iz})}{\partial r} + \frac{\partial(n_e m_i V_{iz}^2 + P_i + P_e)}{\partial z} = J_r B_\theta + S_{iiz} + S_{inz}$$

$$+ K_{in}(V_{nz} - V_{iz}) + K_{en}(V_{nz} - V_{ez}) + \dot{n}_{eI} m_i V_{nz} - \dot{n}_{eR} m_i V_{iz} - \frac{n_e m_i V_{ir} V_{iz}}{r}. \qquad (3.32)$$

3.3 Energy Equations

The conservative form of the species internal energy equation is[5]

$$\frac{\partial}{\partial t}(\frac{3}{2} P_s) + \nabla \cdot (\frac{3}{2} P_s \mathbf{V}_s) + (\mathsf{P}_s \cdot \nabla) \cdot \mathbf{V}_s = \Delta_s + \Phi_s + \kappa_s \qquad (3.33)$$

where Δ_s represents the rate of energy density change due to collisions, and is given in more detail below, κ_s is the negative divergence of the heat flux of species s, described in Section 3.5, and Φ_s is the viscous dissipation function, also described in Section 3.5. Expanding the vector operators to their scalar form for axisymmetric geometries,

$$\frac{\partial}{\partial t}(\frac{3}{2} P_s) + \frac{1}{r}\frac{\partial}{\partial r}(\frac{3}{2} r P_s V_{sr}) + \frac{\partial}{\partial z}(\frac{3}{2} P_s V_{sz}) + P_s \left[\frac{1}{r}\frac{\partial}{\partial r}(r V_{sr}) + \frac{\partial}{\partial z} V_{sz}\right]$$

$$= \Delta_s + \Phi_s + \kappa_s. \qquad (3.34)$$

3.3.1 Collision Terms

From Burgers, the collision terms can be written as

$$\Delta_s = \sum_t K_{st}(\frac{3k}{m_0}(T_t - T_s)$$

$$+\frac{m_t}{m_0}((V_{tr}-V_{sr})^2+(V_{tz}-V_{sz})^2))-\dot{n}_s^-\frac{3}{2}kT_s^-+\dot{n}_s^+\frac{3}{2}kT_s^+, \tag{3.35}$$

where

$$m_0 = m_s + m_t.$$

In order to write the species specific equations, the inelastic collision temperatures T_s^+ and T_s^- must be determined. These temperatures are defined by

$$\frac{3}{2}kT_s^{-,+} = \int F_s^{-,+}\frac{1}{2}m_s c_s^2 dc_s \tag{3.36}$$

As described above, the distribution function for ion and neutral particles entering an inelastic collision is the same as the overall distribution function for that species. Therefore, the collision temperature T_s^- for the heavy particles is just the species temperature, so

$$T_i^- = T_i$$

$$T_n^- = T_n.$$

However, the heavy particles which are created in a collision are created with the temperature and velocity of the particle they are created from. Therefore

$$\int c_s^2 F_s^+ d\mathbf{c}_s = \int c_s^2 F_t d\mathbf{c}_s = \int (\mathbf{c}_t + (\mathbf{V}_t - \mathbf{V}_s)) \cdot (\mathbf{c}_t + (\mathbf{V}_t - \mathbf{V}_s)) F_t d\mathbf{c}_t$$

$$= (\mathbf{V}_t - \mathbf{V}_s) \cdot (\mathbf{V}_t - \mathbf{V}_s) + \frac{3k}{m_t}T_t \tag{3.37}$$

So, the collision temperatures are given by

$$T_i^+ = T_n + \frac{m_n}{3k}U^2 \tag{3.38}$$

and

$$T_n^+ = T_i + \frac{m_i}{3k}U^2 \tag{3.39}$$

For the electrons the inelastic collision temperatures are slightly more complicated. There are six characteristic electron energies, the average energy of the primary elec-

tron before it excites the neutral, the average energy of the primary electron after exciting the neutral, the average energy of the secondary electron after it is emitted by the neutral, the average energy of each of the electrons captured by an ion before recombination, and the average energy of the electron left after a recombination event. A number of simplifying assumptions are used to find these energies. First, the temperature of the electrons participating in recombination is assumed to be just the average electron temperature, since any electron can participate in recombination. Therefore,

$$T^-_{e,R,primary} = T^-_{e,R,secondary} = T_e.$$

The distinction between primary and secondary electrons going into a recombination collision is artificial.

The primary electrons are assumed to be that portion of the Maxwellian distribution with energy greater than the ionization energy, so that

$$F_e^- = \frac{(\frac{m_e}{2\pi kT_e})^{1.5} \exp \frac{-m_e c_e^2}{2kT_e} U(\frac{1}{2}m_e c_e^2 - E_i)}{\int_{\sqrt{\frac{2E_i}{m_e}}}^{\infty} 4\pi c_e^2 dc_e (\frac{m_e}{2\pi kT_e})^{1.5} \exp \frac{-m_e c_e^2}{2kT_e}}$$

where U represents the unit step function. Some messy integration and algebra and the assumption that $E_i \gg kT_e$ yields the "collision temperature", or average energy of the ionizing electron:

$$T^-_{e,I,primary} = T_e + \frac{2E_i}{3k}$$

By a similar argument it can be shown that that

$$T^+_{e,R,primary} = T_e + \frac{2E_i}{3k}$$

Finally, what are the mean energies of the primary and secondary electrons after ionization? For simplicity, it will be assumed that both have the average electron energy. Since $E_i \gg kT_e$ and since we are only interested in the overall balance of

energy during an inelastic collision, this assumption is good enough. So,

$$T^{+}_{e,I,primary} = T^{-}_{e,I,secondary} = T_e.$$

So, an ionization collision takes an electron with energy $T^{-}_{e,I,primary}$ and produces two electrons with energies $T^{+}_{e,I,primary}$ and $T^{+}_{e,I,secondary}$. The electrons as a whole therefore gain energy in an amount given by

$$\frac{3}{2}kT_e^{+} = \frac{3}{2}k(-T^{-}_{e,I,primary} + T^{+}_{e,I,primary} + T^{+}_{e,I,secondary}) = \frac{3}{2}kT_e - E_i$$

Similarly, the electron energy loss during a recombination collision is given by

$$\frac{3}{2}kT_e^{-} = \frac{3}{2}k(-T^{+}_{e,R,primary} + T^{-}_{e,R,primary} + T^{-}_{e,R,secondary}) = \frac{3}{2}kT_e - E_i$$

3.3.2 Heavy Species Equations

After inserting the collision temperatures and velocities the neutral energy equation can be written as

$$\frac{\partial(\frac{3}{2}P_n)}{\partial t} + \frac{\partial(\frac{3}{2}P_nV_{nr})}{\partial r} + \frac{\partial(\frac{3}{2}P_nV_{nz})}{\partial z} + P_n(\frac{\partial V_{nr}}{\partial r} + \frac{\partial V_{nz}}{\partial z})$$

$$= K_{ne}\frac{3k}{m_n}(T_e - T_n) + K_{ni}\left[\frac{3k}{2m_n}(T_i - T_n) + \frac{1}{2}\left((V_{ir} - V_{nr})^2 + (V_{iz} - V_{nz})^2\right)\right]$$

$$- \dot{n}_{eI}\frac{3}{2}kT_n + \dot{n}_{eR}(\frac{3}{2}kT_i + \frac{1}{2}m_iU^2) - \frac{5}{2}\frac{P_nV_{nr}}{r} + \Phi_n + \kappa_n \qquad (3.40)$$

The ion energy equation becomes

$$\frac{\partial(\frac{3}{2}P_i)}{\partial t} + \frac{\partial(\frac{3}{2}P_iV_{ir})}{\partial r} + \frac{\partial(\frac{3}{2}P_iV_{iz})}{\partial z} + P_i(\frac{\partial V_{ir}}{\partial r} + \frac{\partial V_{iz}}{\partial z})$$

$$= K_{in}(\frac{3k}{2m_n}(T_n - T_i) + \frac{1}{2}((V_{nr} - V_{ir})^2 + (V_{nz} - V_{iz})^2)) + K_{ie}\frac{3k}{m_n}(T_e - T_i)$$

$$- \dot{n}_{eR}\frac{3}{2}kT_i + \dot{n}_{eI}(\frac{3}{2}kT_n + \frac{1}{2}m_nU^2) - \frac{5}{2}\frac{P_iV_{ir}}{r} + \Phi_i + \kappa_i. \qquad (3.41)$$

If $T_i = T_n$ then the sum of these two equations is

$$\frac{\partial(\frac{3}{2}P_g)}{\partial t} + \frac{\partial(\frac{3}{2}P_g V_r)}{\partial r} + \frac{\partial(\frac{3}{2}P_g V_z)}{\partial z} + P_g(\frac{\partial V_r}{\partial r} + \frac{\partial V_z}{\partial z}) = \frac{3k}{m_n}(K_{ie} + K_{ne})(T_e - T_g)$$

$$+ \frac{1}{2}\left[K_{ni} + K_{in} + m_i(\dot{n}_{e,I} + \dot{n}_{e,R})\right](U_r^2 + U_z^2) - \frac{5}{2}\frac{P_g V_r}{r} + \Phi + \kappa_i + \kappa_n. \qquad (3.42)$$

where $T_g \equiv T_i = T_n$ and $P_g \equiv \frac{k}{m_i}\rho T_g$.

3.3.3 Electron Energy Equation

The electron energy equation is

$$\frac{\partial(\frac{3}{2}P_e)}{\partial t} + \frac{\partial(\frac{3}{2}P_e V_{er})}{\partial r} + \frac{\partial(\frac{3}{2}P_e V_{ez})}{\partial z} + P_e(\frac{\partial V_{er}}{\partial r} + \frac{\partial V_{ez}}{\partial z}) = K_{ei}\left[\frac{3k}{m_n}(T_i - T_e) + (V_{ir} - V_{er})^2\right.$$

$$\left. + (V_{iz} - V_{ez})^2\right] + K_{en}\left[\frac{3k}{m_n}(T_n - T_e) + (V_{nr} - V_{er})^2 + (V_{nz} - V_{ez})^2\right]$$

$$- \dot{n}_{e,R}(\frac{3}{2}kT_e - E_i) + \dot{n}_{e,I}(\frac{3}{2}kT_e - E_i) - \frac{5}{2}\frac{P_e V_{er}}{r} + \kappa_e. \qquad (3.43)$$

Using the electron continuity equation the energy equation can be rewritten in non-conservative form as

$$\frac{3}{2}n_e k[\frac{\partial T_e}{\partial t} + V_{er}\frac{\partial T_e}{\partial r} + V_{ez}\frac{\partial T_e}{\partial z} + T_e(\frac{\partial V_{er}}{\partial r} + \frac{\partial V_{ez}}{\partial z})] = K_{ei}\left[\frac{3k}{m_n}(T_i - T_e) + (V_{ir} - V_{er})^2\right.$$

$$\left. + (V_{iz} - V_{ez})^2\right] + K_{en}\left[\frac{3k}{m_n}(T_n - T_e) + (V_{nr} - V_{er})^2 + (V_{nz} - V_{ez})^2\right]$$

$$- \dot{n}_e(E_i - \frac{3}{2}kT_e) - \frac{P_e V_{er}}{r} + \kappa_e. \qquad (3.44)$$

This form of the equation looks somewhat strange as it does not explicitly include the Ohmic dissipation. This term is buried in the collision source terms as

$$K_{ei}(V_i - V_e)^2 + (K_{en} + K_{en})(V_n - V_e)^2 = K_{ei}\frac{J^2}{(en_e)^2} + K_{en}(\frac{J}{en_e} - U)^2 = \frac{J^2}{\sigma} - \frac{2K_{en}}{en_e}\mathbf{J}\cdot\mathbf{U} + K_{en}U^2$$

using the definition of conducitivity and K_{st} from above.

Therefore, the energy equation can be written as

$$\frac{3}{2}n_e k[\frac{\partial T_e}{\partial t}+V_{er}\frac{\partial T_e}{\partial r}+V_{ez}\frac{\partial T_e}{\partial z}+T_e(\frac{\partial V_{er}}{\partial r}+\frac{\partial V_{ez}}{\partial z})]=(K_{ei}+K_{en})\left[\frac{3k}{m_n}(T_g-T_e)\right]$$

$$+\frac{J^2}{\sigma}+K_{en}(U^2-2\frac{\mathbf{J}\cdot\mathbf{U}}{en_e})-\dot{n}_e(E_i-\frac{3}{2}kT_e)-\frac{P_eV_{er}}{r}+\kappa_e. \qquad (3.45)$$

3.3.4 Total Energy Equation

The total species energy equation can be derived from the internal energy equation by combining it with the conservative and non-conservative forms of the momentum equation. From the momentum equations it can be shown that

$$P_s\frac{\partial V_{sr}}{\partial r}=\frac{\partial P_sV_{sr}}{\partial r}-n_sq_sV_{sr}(E_r-V_{sz}B_\theta)-A_{sr}V_{sr}+V_{sr}^2\frac{\dot{n}_sm_i}{2}$$

$$+\frac{\partial\frac{1}{2}\rho_sV_{sr}^3}{\partial r}+\frac{\partial\frac{1}{2}\rho_sV_{sr}^2V_{sz}}{\partial z}-\frac{1}{2}\rho_sV_{sr}^3-(S_{sir}+S_{snr})V_{sr}+\frac{1}{2}\frac{\partial\rho_sV_{sr}^2}{\partial t} \qquad (3.46)$$

and

$$P_s\frac{\partial V_{sz}}{\partial z}=\frac{\partial P_sV_{sz}}{\partial z}-n_sq_sV_{sz}(E_z+V_{sr}B_\theta)-A_{sz}V_{sz}+V_{sz}^2\frac{\dot{n}_sm_i}{2}$$

$$+\frac{\partial\frac{1}{2}\rho_sV_{sz}^3}{\partial z}+\frac{\partial\frac{1}{2}\rho_sV_{sr}V_{sz}^2}{\partial r}-\frac{1}{2r}\rho_sV_{sr}V_{sz}^2-(S_{siz}+S_{snz})V_{sz}+\frac{1}{2}\frac{\partial\rho_sV_{sz}^2}{\partial t} \qquad (3.47)$$

Inserting the above into the internal species energy equations yields the species total energy equation,

$$\frac{\partial}{\partial t}(\frac{3}{2}P_s+\frac{1}{2}\rho_s(V_{sr}^2+V_{sz}^2))+\frac{1}{r}\frac{\partial}{\partial r}\left[rV_{sr}\left(\frac{5}{2}P_s+\frac{1}{2}\rho_s(V_{sr}^2+V_{sz}^2)\right)\right]$$

$$+\frac{\partial}{\partial z}\left[V_{sz}\left(\frac{5}{2}P_s+\frac{1}{2}\rho_s(V_{sr}^2+V_{sz}^2)\right)\right]=n_sq_s(V_{sr}E_r+V_{sz}E_z)$$

$$+(S_{sir}+S_{snr})V_{sr}+(S_{siz}+S_{snz})V_{sz}+\Delta_s+\Phi_s+\kappa_s+\mathbf{A}_s\cdot\mathbf{V}_s-\frac{1}{2}\dot{n}_sm_iV_s^2 \qquad (3.48)$$

The global total energy equation is derived by summing over all species,

$$\frac{\partial}{\partial t}\left(\frac{3}{2}P+\frac{1}{2}\rho_i(V_{ir}^2+V_{iz}^2)+\frac{1}{2}\rho_n(V_{nr}^2+V_{nz}^2)\right)+\frac{1}{r}\frac{\partial}{\partial r}\left[r\left(\frac{5}{2}(P_gV_r+P_eV_{er})\right.\right.$$

$$+\frac{1}{2}\rho_i V_{ir}(V_{ir}^2+V_{iz}^2)+\frac{1}{2}\rho_n V_{nr}(V_{nr}^2+V_{nz}^2)\Big)\Big]+\frac{\partial}{\partial z}\left[\frac{5}{2}(P_g V_z+P_e V_{ez})+\frac{1}{2}\rho_i V_{iz}(V_{ir}^2+V_{iz}^2)\right.$$

$$\left.+\frac{1}{2}\rho_n V_{nz}(V_{nr}^2+V_{nz}^2)\right]=J_r E_r+J_z E_z+(S_{iir}+S_{inr})V_{ir}+(S_{nir}+S_{nnr})V_{nr}$$

$$+(S_{iiz}+S_{inz})V_{iz}+(S_{niz}+S_{nnz})V_{nz}+\Phi+\kappa_i+\kappa_e+\kappa_n+m_i\dot{n}_e E_i \qquad (3.49)$$

where the terms proportional to the electron mass have been neglected. In vector form

$$\frac{\partial}{\partial t}\left(\frac{3}{2}P+\frac{1}{2}(\rho_i\mathbf{V}_i\cdot\mathbf{V}_i+\rho_n\mathbf{V}_n\cdot\mathbf{V}_n)+n_e E_i\right)+\nabla\cdot\left[\frac{5}{2}(P_g\mathbf{V}+P_e\mathbf{V}_{er})+\frac{1}{2}\rho_i\mathbf{V}_i\mathbf{V}_i\cdot\mathbf{V}_i\right.$$

$$\left.+\frac{1}{2}\rho_n\mathbf{V}_n\mathbf{V}_n\cdot\mathbf{V}_n+E_i n_e\mathbf{V_i}\right]=\mathbf{J}\cdot\mathbf{E}+(\nabla\cdot\Pi_\mathbf{i})\cdot\mathbf{V_i}+(\nabla\cdot\Pi_\mathbf{n})\cdot\mathbf{V_n}+\nabla\cdot(\Pi_\mathbf{i}\cdot\mathbf{V_i}+\Pi_\mathbf{n}\cdot\mathbf{V_n})$$

$$-(\nabla\cdot\Pi_\mathbf{i})\cdot\mathbf{V_i}-(\nabla\cdot\Pi_\mathbf{n})\cdot\mathbf{V_n}+\nabla\cdot\mathbf{H_e}+\nabla\cdot\mathbf{H_i}+\nabla\cdot\mathbf{H_n} \qquad (3.50)$$

where H is defined in Section 3.5.2. Since $\mathbf{J}=\frac{1}{\mu_0}\nabla\times\mathbf{B}$,

$$\mathbf{J}\cdot\mathbf{E}=\frac{1}{\mu_0}(\nabla\times\mathbf{B})\cdot\mathbf{E}=\frac{1}{\mu_0}(\mathbf{B}\cdot\nabla\times\mathbf{E}-\nabla\cdot(\mathbf{E}\times\mathbf{B}))$$

From Maxwell's equations, $\nabla\times\mathbf{E}=-\frac{\partial B}{\partial t}$, so $\mathbf{J}\cdot\mathbf{E}=-\frac{1}{\mu_0}\nabla\cdot(\mathbf{E}\times\mathbf{B})-\frac{\partial}{\partial t}\frac{B^2}{2\mu_0}$. So, the global total energy equation is,

$$\frac{\partial}{\partial t}\left[\frac{3}{2}P+\rho_i V_i^2+\rho_n V_n^2+\frac{B^2}{2\mu_0}+n_e E_i\right]+\nabla\cdot\left[\frac{5}{2}(P_g\mathbf{V}+P_e\mathbf{V}_{er})+\frac{1}{2}\rho_i\mathbf{V_i}\mathbf{V_i}\cdot\mathbf{V_i}\right.$$

$$\left.+\frac{1}{2}\rho_n\mathbf{V_n}\mathbf{V_n}\cdot\mathbf{V_n}+\frac{1}{\mu_0}\mathbf{E}\times\mathbf{B}+n_e\mathbf{V}_i E_i-\Pi_\mathbf{i}\cdot\mathbf{V_i}-\Pi_\mathbf{n}\cdot\mathbf{V_n}+\mathbf{H}_e+\mathbf{H}_i+\mathbf{H}_n\right]=0 \qquad (3.51)$$

3.4 Electromagnetic Equations

The last governing equation for MPD channels comes from the electromagnetic properties of the thruster. The time rate of change of the magnetic field is given by

$$\frac{\partial\mathbf{B}}{\partial t}+\nabla\times\mathbf{E}=0 \qquad (3.52)$$

or in scalar form for a magnetic field in the azimuthal direction only,

$$\frac{\partial B_\theta}{\partial t} = -\frac{\partial E_r}{\partial z} + \frac{\partial E_z}{\partial r}. \tag{3.53}$$

Ampere's Law gives

$$\mathbf{J} = \frac{1}{\mu_0}(\nabla \times \mathbf{B}) \tag{3.54}$$

where the displacement current has been neglected. The scalar components of the current are given by

$$J_r = -\frac{1}{\mu_0}\frac{\partial B_\theta}{\partial z} \tag{3.55}$$

and

$$J_z = \frac{1}{\mu_0 r}\frac{\partial r B_\theta}{\partial r} = \frac{1}{\mu_0}\frac{\partial B_\theta}{\partial r} + \frac{B_\theta}{\mu_0 r} \tag{3.56}$$

The electric field is defined by Ohm's Law, of which the scalar form was given earlier. The vector form is

$$\mathbf{E} = \frac{\mathbf{J}}{\sigma} - (\mathbf{V} + \frac{n_n}{n_e + n_n}\mathbf{U}) \times \mathbf{B} + \frac{1}{en_e}(\mathbf{J} \times \mathbf{B} - \nabla \cdot \mathsf{P}_e) \tag{3.57}$$

3.5 Transport Properties

Modeling of the contributions to the equations from the viscosity and heat conduction terms is described in this section. Subsection 3.5.1 describes the two fluid model used for the off diagonal pressure terms and the viscosity coefficients. Subsection 3.5.2 describes the contribution of both heavy species and electron heat conduction to the governing equations, and the derivation of both heat conduction coefficients.

3.5.1 Viscosity

Viscosity appears in the governing equations due to the off diagonal and non-isotropic terms of the pressure tensor, P_s. Because of the substantial slip between neutrals and ions, these off diagonal terms are more complex than those in the one fluid Navier-Stokes equations. A derivation and expression for these terms was found in

a recent paper by Fernandez and Fernandez[14]. According to their derivation the non-isotropic part of the pressure tensor is given by

$$\Pi_s = 2v_{si}\nabla \circ \mathbf{V}_i + 2v_{sn}\nabla \circ \mathbf{V}_n. \tag{3.58}$$

where from Ferziger and Kaper[15] the operator $\nabla \circ \mathbf{V}$ is the symmetric traceless gradient of $\mathbf{V}$ given by

$$\nabla \circ \mathbf{V}_s \equiv \tilde{\nabla}\mathbf{V}_s - \frac{1}{3}(\nabla \cdot \mathbf{V}_s)\mathsf{I} \equiv \Upsilon_s \tag{3.59}$$

Expanding for an axisymmetric geometry,

$$\Upsilon_s = \begin{bmatrix} \frac{1}{3}(2\frac{\partial V_{sr}}{\partial r} - \frac{\partial V_{sz}}{\partial z} - \frac{V_{sr}}{r}) & 0 & \frac{1}{2}(\frac{\partial V_{sr}}{\partial z} + \frac{\partial V_{sz}}{\partial r}) \\ 0 & \frac{1}{3}(2\frac{V_{sr}}{r} - \frac{\partial V_{sr}}{\partial r} - \frac{\partial V_{sz}}{\partial z}) & 0 \\ \frac{1}{2}(\frac{\partial V_{sr}}{\partial z} + \frac{\partial V_{sz}}{\partial r}) & 0 & \frac{1}{3}(2\frac{\partial V_{sz}}{\partial z} - \frac{\partial V_{sr}}{\partial r} - \frac{V_r}{r}) \end{bmatrix}$$

where $\tilde{\nabla}\mathbf{V}_s$ is the average of $\nabla\mathbf{V}_s$ and $(\nabla\mathbf{V}_s)^T$ and is given by

$$\Upsilon_s = \begin{bmatrix} \frac{\partial V_{sr}}{\partial r} & 0 & \frac{1}{2}(\frac{\partial V_{sr}}{\partial z} + \frac{\partial V_{sz}}{\partial r}) \\ 0 & \frac{V_{sr}}{r} & 0 \\ \frac{1}{2}(\frac{\partial V_{sr}}{\partial z} + \frac{\partial V_{sz}}{\partial r}) & 0 & \frac{\partial V_{sz}}{\partial z} \end{bmatrix}$$

So,

$$\Pi_s = 2v_{si}\Upsilon_i + 2v_{sn}\Upsilon_n. \tag{3.60}$$

The divergence of the pressure tensor appears in the momentum equations. Expanding the divergence gives

$$\nabla \cdot \Pi_s = \left[\frac{1}{r}\frac{\partial r\Pi_{srr}}{\partial r} + \frac{\partial \Pi_{srz}}{\partial z} - \frac{\Pi_{s\theta\theta}}{r}\right]\hat{r} + \left[\frac{1}{r}\frac{\partial r\Pi_{srz}}{\partial r} + \frac{\partial \Pi_{szz}}{\partial z}\right]\hat{z}. \tag{3.61}$$

For compactness, this will be written as

$$\nabla \cdot \Pi_s = (S_{sir} + S_{snr})\hat{r} + (S_{siz} + S_{snz})\hat{z}. \tag{3.62}$$

where

$$S_{str} = 2\left(\frac{1}{r}\frac{\partial r v_{st}\Upsilon_{trr}}{\partial r} + \frac{\partial v_{st}\Upsilon_{trz}}{\partial z} - \frac{v_{st}\Upsilon_{t\theta\theta}}{r}\right)$$

and

$$S_{stz} = 2\left(\frac{1}{r}\frac{\partial r v_{st}\Upsilon_{trz}}{\partial r} + \frac{\partial v_{st}\Upsilon_{tzz}}{\partial z}\right)$$

From Anderson[1], expanding the various derivatives yields

$$S_{str} = v_{st}\left[\frac{4}{3}\frac{\partial^2 V_{tr}}{\partial r^2} + \frac{\partial^2 V_{tr}}{\partial z^2} + \frac{1}{3}\frac{\partial^2 V_{tz}}{\partial r \partial z}\right] + \frac{4}{3}\frac{\partial V_{tr}}{\partial r}\left(\frac{v_{st}}{r} + \frac{\partial v_{st}}{\partial r}\right) + \frac{\partial V_{tr}}{\partial z}\frac{\partial v_{st}}{\partial z}$$

$$+ \frac{\partial V_{tz}}{\partial r}\frac{\partial v_{st}}{\partial z} - \frac{2}{3}\frac{\partial V_{tz}}{\partial z}\frac{\partial v_{st}}{\partial r} - \frac{2}{3}\frac{V_{tr}}{r}\left(\frac{\partial v_{st}}{\partial r} + 2\frac{v_{st}}{r}\right) \tag{3.63}$$

and

$$S_{stz} = v_{st}\left[\frac{4}{3}\frac{\partial^2 V_{tz}}{\partial z^2} + \frac{\partial^2 V_{tz}}{\partial r^2} + \frac{1}{3}\frac{\partial^2 V_{tr}}{\partial r \partial z}\right] + \frac{\partial V_{tr}}{\partial z}\left(\frac{1}{3}\frac{v_{st}}{r} + \frac{\partial v_{st}}{\partial r}\right) - \frac{2}{3}\frac{\partial V_{tr}}{\partial r}\frac{\partial v_{st}}{\partial z}$$

$$- \frac{2}{3}\frac{V_{tr}}{r}\frac{\partial v_{st}}{\partial z} + \frac{\partial V_{tz}}{\partial r}\left(\frac{\partial v_{st}}{\partial r} + \frac{v_{st}}{r}\right) + \frac{4}{3}\frac{\partial v_{st}}{\partial z}\frac{\partial V_{tz}}{\partial z} \tag{3.64}$$

The pressure tensor also appears in the energy equations. In the form of the energy equation used in Section 3.3, the non-diagonal terms of the pressure tensor are buried in the viscous dissipaton term and are given by

$$\Phi_s = \nabla \cdot (\Pi_s \cdot \mathbf{V}_s) - (\nabla \cdot \Pi_s) \cdot \mathbf{V}_s = \Pi_s : \nabla \mathbf{V}_s \tag{3.65}$$

From Anderson again,

$$\Phi = \Phi_i + \Phi_n = \sum_s \left[(v_{si} + v_{sn})\left(\frac{4}{3}\left(\left(\frac{\partial V_{sr}}{\partial r}\right)^2 + \left(\frac{V_r}{r}\right)^2 + \left(\frac{\partial V_z}{\partial z}\right)^2 - \frac{V_{sr}}{r}\frac{\partial V_{sr}}{\partial r}\right.\right.\right.$$

$$-\frac{\partial V_{sr}}{\partial r}\frac{\partial V_{sz}}{\partial z}-\frac{V_{sr}}{r}\frac{\partial V_{sz}}{\partial z})+(\frac{\partial V_{sr}}{\partial z}+\frac{\partial V_{sz}}{\partial r})^2\Big)\Big] \tag{3.66}$$

The various viscosity coefficients as given by Fernandez are

$$v_{ii}=[\alpha^2(\frac{2}{3}+a_i)+\frac{\alpha(1-\alpha)v_\star}{v_n}]/q_i, \tag{3.67}$$

$$v_{nn}=[(1-\alpha)^2(\frac{2}{3}+a_i)+\frac{\alpha(1-\alpha)v_\star}{v_i}]/q_i, \tag{3.68}$$

and

$$v_{in}=v_{ni}=\alpha(1-\alpha)(\frac{2}{3}-a_i)/q_i \tag{3.69}$$

where

$$q_i=(\frac{2}{3}+a_i)[\frac{\alpha^2}{v_i}+\frac{(1-\alpha)^2}{v_n}]+\alpha(1-\alpha)[\frac{v_\star}{v_n v_i}+\frac{8a_i}{3v_\star}],$$

$$v_i=\frac{5kT_g}{8\Omega_i^{(2,2)}},$$

$$v_n=\frac{5kT_g}{8\Omega_n^{(2,2)}},$$

$$v_\star=\frac{kT_g}{4\Omega_{in}^{(1,1)}},$$

and

$$a_i=\frac{\Omega_{in}^{(2,2)}}{5\Omega_{in}^{(1,1)}}.$$

T_g is used because Fernandez and Fernandez assume a single temperature mixture.

The collision integrals Ω are defined by Ferziger and Kaper [15] as

$$\Omega_{ij}^{(l,r)}=(\frac{kT_g}{2\pi m_{ij}})^{\frac{1}{2}}\int_0^\infty e^{-g^2}g^{2r+3}Q_{ij}^{(l)}dg \tag{3.70}$$

where

$$Q_{ij}^{(l)}=2\pi\int[1-\cos^l\chi_{ij}(b,g)]bdb, \tag{3.71}$$

$$m_{ij}^{-1}=m_i^{-1}+m_j^{-1},$$

$$g=(\frac{m_{ij}}{2kT_g})^{\frac{1}{2}}g.$$

and χ is the scattering angle for a given impact parameter, b, and approach speed, g.

The neutral-neutral and ion-neutral collisions will be modeled as hard sphere collisions. The various collision cross sections are then given by [28]

$$Q_{st}^{(l)} = \left[1 - \frac{1}{2}\frac{1+(-1)^l}{1+l}\right]\pi\sigma^2 \tag{3.72}$$

Experimental measurements are available for the momentum transfer cross sections, $Q_{st}^{(1)}$ so that

$$Q_{st}^{(1)} = \pi\sigma^2 = Q_{st}^{\text{experimental}}. \tag{3.73}$$

From Equation 3.72

$$Q_{st}^{(2)} = \frac{2}{3}Q_{st}^{(1)} = \frac{2}{3}Q_{st}^{\text{experimental}}. \tag{3.74}$$

Using experimental values from Lieberman and Velikovich [43], the relevant cross sections are given by

$$Q_{nn}^{(2)} = \frac{2}{3}Q_{nn}^{experimental} = \frac{2}{3}(1.7 \times 10^{-18}T_n^{-\frac{1}{4}}) \tag{3.75}$$

and

$$Q_{in}^{(2)} = \frac{2}{3}Q_{in}^{experimental} = \frac{2}{3}(1.4 \times 10^{-18}). \tag{3.76}$$

All units in the thesis are MKS unless otherwise noted. Then, the corresponding collision integrals are

$$\Omega_{in}^{(2,2)} = (\frac{kT_g}{2\pi m_{in}})^{\frac{1}{2}}2Q_{in}^{experimental} \tag{3.77}$$

and

$$\Omega_{in}^{(1,1)} = (\frac{kT_g}{2\pi m_{in}})^{\frac{1}{2}}Q_{in}^{experimental}. \tag{3.78}$$

For the ion-ion collisions the integrals can be approximated using the Coulomb interaction potential cut off at the Debye length. From Ferziger and Kaper again,

$$\Omega_{ii}^{(2,2)} = \frac{1}{4}(\frac{2\pi kT_g}{m_{ii}})^{\frac{1}{2}}(\frac{e^2}{4\pi\epsilon_0 kT_g})^2 \ln\Gamma_g \tag{3.79}$$

where

$$\Gamma_s = 1.24 \times 10^7 \sqrt{\frac{T_s^3}{n_e}}. \tag{3.80}$$

3.5.2 Heat Conduction

The heat conduction terms appear only in the energy equations. They are given in the energy equations as κ_s where $\kappa_s = -\nabla \cdot \mathbf{H_s}$. The heat flux vector, $\mathbf{H}$ is given by

$$\mathbf{H_s} = -\Theta_s \nabla T_s. \tag{3.81}$$

where Θ represents the thermal conductivity. So, the contribution from the heat conduction terms is

$$\kappa_s = -\nabla \cdot (-\Theta_s \nabla T_s) = \Theta_s \nabla \cdot \nabla T_s + (\nabla T_s) \cdot \nabla \Theta_s \tag{3.82}$$

Expanding the vector operators for a cylindrical coordinate system,

$$\kappa_s = \Theta_s \left[\frac{1}{r} \frac{\partial}{\partial r} (r \frac{\partial T_s}{\partial r}) + \frac{\partial^2 T_s}{\partial z^2} \right] + (\frac{\partial T_s}{\partial r} \hat{r} + \frac{\partial T}{\partial z} \hat{z}) \cdot (\frac{\partial \Theta_s}{\partial r} \hat{r} + \frac{\partial \Theta_s}{\partial z} \hat{z}) \tag{3.83}$$

or

$$\kappa_s = \Theta_s \left[\frac{1}{r} \frac{\partial T_s}{\partial r} + \frac{\partial^2 T_s}{\partial r^2} + \frac{\partial^2 T_s}{\partial z^2} \right] + \frac{\partial T_s}{\partial r} \frac{\partial \Theta_s}{\partial r} + \frac{\partial T_s}{\partial z} \frac{\partial \Theta_s}{\partial z}. \tag{3.84}$$

From Mitchner and Kruger [51], the thermal conductivity for the electrons is given by

$$\Theta_e = \frac{2.4}{1 + \frac{\nu_{ei}}{\sqrt{2}\nu_{eg}}} \frac{k^2 n_e T_e}{m_e \nu_{eg}} \tag{3.85}$$

For each of the heavy species the thermal conductivity is given similarly by

$$\Theta_s = \frac{k^2 T_g}{m_i \bar{C}_g} \left[\frac{n_n}{n_n Q_{nn} + n_e Q_{in}} + \frac{n_e}{n_e Q_{ii} + n_n Q_{in}} \right] \tag{3.86}$$

where

$$Q_{ii} = \frac{e^4 \ln \Gamma_i}{32 \pi \epsilon_0^2 k^2 T_i^2}. \tag{3.87}$$

and

$$\bar{C}_s = \sqrt{\frac{8kT_s}{\pi m_s}}$$

3.6 Ionization Model

This research grew out of one dimensional modeling described in the author's masters thesis. That modeling used a recombination rate from Hinnov and Hirschberg [27]. However, work performed by Sheppard at M.I.T. showed that in the electron temperature range of interest, between 1 and 5 eV, the Hinnov-Hirschberg expression overpredicted the recombination rate by orders of magnitude. Sheppard developed a more accurate expression based on a fit to a multilevel model which compared well with experiment. His recombination coefficient, R, for Argon is given by [59]

$$\dot{R} = 8.25 \times 10^{-43} e^{1.6276(\log \frac{T_e}{1000} - 3.95)^2} \tag{3.88}$$

The recombination rate is then given by

$$\dot{n}_{eR} = R n_e^3.$$

By detailed balancing, the ionization rate is then given by

$$\dot{n}_{eI} = RS n_e n_n$$

where

$$S = 2.9 \times 10^{22} T_e^{\frac{3}{2}} \exp\left(\frac{-eE_i}{kT_e}\right)$$

3.7 Performance Calculations

The long term goal of most, if not all, MPD research is to produce better MPD thrusters. With this in mind, it is important to determine what the simulation developed for this research predicts for thrust, power input, efficiency, specific impulse,

and the importance of the various loss mechanisms.

3.7.1 Thrust and Specific Impulse

The thrust is assumed to be equal to the momentum loss across the exit plane of the thruster. For the thruster geometries described in this thesis, the thrust is given by

$$T = \int_{r_c}^{r_a} 2\pi r(\rho_i V_{iz}^2 + \rho_n V_{nz}^2 + P + \frac{B^2}{2\mu_0})dr \tag{3.89}$$

as the magnetic field is not zero at the exit plane of the thruster. Alternatively, the thrust can be defined at the end of the insulating sections,

$$T = \int_{r_c}^{r_a} 2\pi r(\rho_i V_{iz}^2 + \rho_n V_{nz}^2 + P)dr \tag{3.90}$$

but then there will be additional viscous loss due to the longer channel length.

The specific impulse is defined as

$$I_{sp} = \frac{T}{\dot{m}g} \tag{3.91}$$

Because the plume is not included in the simulation and an insulating section is added, the thrust predicted by this research is expected to be lower than the thrust of an actual experimental device with no insulating sections firing into a vacuum.

3.7.2 Power Input and Efficiency

The efficiency is given by the ratio of the exhaust jet power to the input power. The input power to the thruster is made up of the electrical power and the power carried by the fuel entering the thruster. So, the input power to the device is given by

$$\text{Input Power} = \int_{r_c}^{r_a} 2\pi r \left[\frac{1}{\mu_0} E_r B_\theta + \frac{5}{2} P V_z + \frac{1}{2}\rho V_z^3 + n_e V_z E_i\right] dr = IV + \dot{m} h_{t0} A_0$$

where the assumption that $V_{iz} = V_{nz}$ at the inlet has been employed and where the inlet total enthalpy is given by

$$h_{t0} = \frac{\gamma}{\gamma - 1}\frac{P}{\rho} + \frac{1}{2}V_z^2 + \alpha\frac{E_i}{m_i}$$

The exhaust jet power is given by

$$\text{Jet Power} = \int_{r_c}^{r_a} 2\pi r \left[\frac{1}{2}\rho V_{iz}^2 + \frac{1}{2}\rho V_{nz}^2\right] dr$$

The efficiency is then given by

$$\eta = \frac{\text{jet power}}{\text{input power}}.$$

3.7.3 Loss Mechanisms

All of the input energy which does not go into the jet must be lost somewhere else. Much of this energy is deposited in the electrodes. A substantial fraction of the input energy is also absorbed by frozen and thermal flow losses and fluid stresses. The various loss terms can be identified by examining the total energy equation. As described in Section 3.3.4, the steady state total energy equation can be written in the form $\nabla \cdot \mathbf{\Sigma} = 0$ By the divergence theorem for an axisymmetric coordinate system

$$2\pi \left[\int_{r_c}^{r_a} \mathbf{\Sigma}(r, z = 0) \cdot \hat{\mathbf{z}} r dr - \int_0^l \mathbf{\Sigma}(r = r_a, z) \cdot \hat{\mathbf{r}} r_a dz - \int_{r_a}^{r_c} \mathbf{\Sigma}(r, z = l) \cdot \hat{\mathbf{z}} r dr \right.$$

$$\left. + \int_l^0 \mathbf{\Sigma}(r = r_c, z) \cdot \hat{\mathbf{r}} r_c dz\right] = 0. \tag{3.92}$$

$\mathbf{\Sigma}$ is given by

$$\mathbf{\Sigma} = \frac{5}{2}(P_g \mathbf{V} + P_e \mathbf{V}_{er}) + \frac{1}{2}\rho_i \mathbf{V}_i \mathbf{V}_i \cdot \mathbf{V}_i + \frac{1}{2}\rho_n \mathbf{V}_n \mathbf{V}_n \cdot \mathbf{V}_n + n_e \mathbf{V}_i E_i$$

$$+ \frac{1}{\mu_0}\mathbf{E} \times \mathbf{B} - \Pi_i \cdot \mathbf{V_i} - \Pi_n \cdot \mathbf{V}_n + \mathbf{Q}_e + \mathbf{Q}_i + \mathbf{Q}_n \tag{3.93}$$

At the inlet, $V_{iz} = V_{nz}$ and $V_{nr} = V_{ir} = J_z = \mathbf{Q}_e = 0$. So, the power transfer through the backplate is given by

$$\text{Backplate Power Transfer} = 2\pi \int_{r_c}^{r_a} \mathbf{\Sigma}(r, z=0)\cdot\hat{\mathbf{z}} r dr = 2\pi \int_{r_c}^{r_a} \left[(\frac{5}{2}P + \frac{1}{2}\rho V_z^2)V_z - \frac{1}{\mu_0} E_r B_\theta \right.$$

$$\left. + \Pi_{zz} V_z - \theta_g \frac{\partial T_g}{\partial z} + n_e V_z E_i \right] r dr = \dot{m} h_{t0} + VI + 2\pi \int_{r_c}^{r_a} \left[\Pi_{zz} V_z - \Theta_g \frac{\partial T_g}{\partial z} \right] r dr$$

$$= \text{Power input} + \text{viscous stress on backplate - heat transfer to backplate} \quad (3.94)$$

At the exit, $B = J_z = 0$. So, the power carried through the exit is given by

$$\text{exit power} = 2\pi \int_{r_c}^{r_a} \left[\frac{5}{2}(P_g V_z + P_e V_{iz}) + \frac{1}{2}\rho_i V_{iz}^3 + \frac{1}{2}\rho_n V_{nz}^3 \right.$$

$$\left. - \Pi_{izr} V_{ir} - \Pi_{nzr} V_{nr} - \Pi_{izz} V_{iz} - \Pi_{nzz} V_{nz} - \Theta_g \frac{\partial T_g}{\partial z} \right] r dr \quad (3.95)$$

A large part of this exit power is the useful jet power. However, there are also losses at the exit due to the ionization energy of the electrons being carried downstream, viscous stresses, and the convected thermal energy flux.

At the electrodes, $V_r = V_{iz} = V_{nz} = E_z = 0$. So, the power transfer at the anode is given by

$$\text{anode power} = -2\pi r_a \int_0^l \left[\frac{5}{2} k T_e (n_e V_{ir} - \frac{J_r}{e}) + n_e V_{ir} E_i + \frac{1}{2}(\rho_i V_{ir}^3 + \rho_n V_{nr}^3) \right.$$

$$\left. - \Pi_{irr} V_{ir} - \Pi_{nrr} V_{nr} - \Theta_g \frac{\partial T_g}{\partial r} \right] dz.$$

So, power is being lost to the anode through loss of the ionization energy of ion-electron pairs, thermal energy of electrons, viscous stresses, heavy species heat conduction, and the different energy of ions impinging and neutrals returning from the electrode.

The power lost at the cathode is similar to the anode power transfer

$$\text{cathode power} = -2\pi r_c \int_0^l \left[\frac{5}{2} k T_e (n_e V_{ir} - \frac{J_r}{e}) + n_e V_{ir} E_i + \frac{1}{2}\rho_i V_{ir}^3 + \frac{1}{2}\rho_n V_{nr}^3 \right.$$

$$-\Pi_{irr}V_{ir} - \Pi_{nrr}V_{nr} - \Theta_g\frac{\partial T_g}{\partial r}\Bigg] dz.$$

Chapter 4

Solution Techniques

The formulation described in Chapter 3 comprises a system of partial differential equations which do not yield to analytical solutions. Therefore, finite difference schemes are used to solve the governing equations on a computer. The scheme used is a combination of a number of different methods and is outlined in Section 4.1. The boundary conditions are detailed in Section 4.2. The equations are solved in a transformed coordinate space to allow the use of variable grid spacing. The grids used and the transformation techniques are described in Section 4.3. Some of the numerical issues are discussed in more detail in Appendix D. The computer code, the inputs needed to run it, and the outputs it produces are described in some detail in Appendix E.

4.1 Numerical Method

Chapter 3 described the equations which must be solved. Since these equations are intractable analytically, numerical techniques are used to obtain solutions. The type of numerical schemes used in the research are known as finite difference methods, although some finite volume ideas are incorporated into the overall numerical scheme. No single method is used for all of the equations or even for all the parts of a single equation. The methods used include the Steger-Warming version of flux vector splitting[67], Rusanov's method[58], and MacCormack's method [1] as well as techniques developed specifically for this research. All of these methods are described in

more detail below.

4.1.1 Time Scales

A number of different time scales are present in the different equations. These time scales are important for determining the maximum time step which can be used in the simulation and the number of time steps which must be taken to reach a converged solution. The time step for any equation must be such that information does not physically propagate further during a time step than the length or height of a cell in the computational grid. The longest time scale is typically the flow time of the plasma in the thruster. Therefore, the least stringent time step limitation is usually the CFL condition,

$$\Delta t \leq min(\frac{\Delta z}{|V_z| + a}, \frac{\Delta r}{|V_r| + a}).$$

where V_z and V_r are the values in the cell and $a = \sqrt{\gamma \frac{k}{m_i} T}$. For Navier-Stokes equations there is also a diffusive time scale due to momentum and heat diffusion. These time scales are given by

$$\tau_{viscous} = \frac{\rho L^2}{v}$$

and

$$\tau_{heatconduction} = \frac{\rho k L^2}{m\Theta}$$

where Θ and ρ are again representative of the flowfield as a whole. These translate to a time step limitation of

$$\Delta t \leq min(\frac{3}{2}\frac{k}{m_i}\frac{\rho(\Delta r)^2}{\Theta_g}, \frac{\rho_i \rho_n (\Delta r)^2}{\rho_n(v_{ii} + v_{in}) + \rho_i(v_{nn} + v_{in})})$$

as, typically, $\Delta r << \Delta z$. Normally, the diffusive limit is smaller than the CFL limit by a factor of about 10.

Each of the collisional source terms in the fluid equations also introduces its own time scale. The presence of chemical reactions imply some time needed for those reactions to bring the system to equilibrium. Momentum coupling between ions and

neutrals implies a time needed for the two species to be brought to the same velocity. These time scales are hard to quantify as the relevant cross sections and rates vary rapidly and by orders of magnitude spatially. In general, for the cases examined in this research, both ion and neutral velocities and heavy and electron temperatures are tightly coupled. However, they are not so tightly coupled as to be in equilibrium with each other and have very small (compared to the flow time) time scales. The time scale to reach ionizational equilibrium does seem to be relatively short, although the ionization fraction does not reach its equilibrium value before the thruster exit. Without the diffusive time scale described above, the time step would still be limited to CFL numbers of between 0.1 and 0.2 by collisional source terms in the regimes of interest for this research.

All three of the time scales described above are roughly of the same order and do not vary considerably in the course of finding a solution. However, the electron energy and magnetic field equations introduce time step limitations which can be considerably smaller than those due to the other equations. Both equations contain diffusive and convective terms. For the electrons, the diffusive terms usually determine the maximum time step except when anode starvation is severe and electron velocities in the starved region become quite large,

$$\Delta t \leq min(\frac{\Delta z \Delta r}{\Delta r V_{ze} + \Delta z V_{re}}, \frac{3}{2}\frac{k}{m_i}\frac{\rho_i(\Delta r)^2}{\Theta_e})$$

This time step varies considerably from case to case but can be from 10-100 times smaller than the diffusive fluid time scale.

Finally, there are time scales associated with the magnetic field equation. The magnetic field equation of Chapter 3 can be written in a form with the current and electric field terms replaced by products and derivatives of the fundamental variables. The resulting equation is

$$\frac{\partial B_\theta}{\partial t} + \frac{\partial V_{ir} B_\theta}{\partial r} + \frac{\partial V_{iz} B_\theta}{\partial z} + \frac{\partial}{\partial r}(\frac{1}{en_e})\frac{\partial P^*}{\partial z} - \frac{\partial}{\partial z}(\frac{1}{en_e})\frac{\partial P^*}{\partial r} - \frac{\partial}{\partial r}(\frac{1}{\mu_0 \sigma})(\frac{\partial B_\theta}{\partial r} + \frac{B_\theta}{r})$$

$$-\frac{\partial}{\partial z}(\frac{1}{\mu_0\sigma})\frac{\partial B_\theta}{\partial z}-\frac{1}{\mu_0\sigma}(\frac{\partial^2 B_\theta}{\partial r^2}+\frac{\partial^2 B_\theta}{\partial z^2}+\frac{1}{r}\frac{\partial B_\theta}{\partial r}-\frac{B_\theta}{r^2})+\frac{1}{r}\frac{\partial}{\partial z}(\frac{B_\theta^2}{\mu_0 e n_e})=0 \quad (4.1)$$

where $P^* = \frac{B_\theta^2}{2\mu_0} + P_e$. Writing the equation in this form helps to show what the associated time scales are. The most important of these are the diffusive time scale due to the radial magnetic diffusion and the convective time due to multiplying the axial magnetic field gradient by the radial gradient of the electron number density. The resulting maximum time step is

$$\Delta t \leq \frac{\mu_0}{\frac{1}{\sigma(\Delta r)^2}+\frac{|\frac{\partial}{\partial r}(\frac{1}{n_e})|}{4e\Delta z}}$$

This is typically the smallest time step in the simulation, about 100-200 times smaller than the diffusive fluid time step.

4.1.2 Overall Method

In order not to have to run the complete simulation at either the maximum magnetic field or electron temperature time step, these equations are split from the rest of the simulation and solved a given number of times for each time step of the fluid equations. The overall flow of the computer program is shown in Figures 4-1 - 4-4. The electron temperature equation is updated immediately before the integration variables. The magnetic field equation is solved after the source terms are computed for the next fluid integration step.

All of the fluid equations except the electron temperature equation are updated in the same manner, using the standard finite difference formulation

$$U^{n+1}(i,j) = U^n(i,j) - \Delta t\left[g(i,j+\frac{1}{2}) - g(i,j-\frac{1}{2}) + f(i+\frac{1}{2},j) - f(i-\frac{1}{2},j) + c(i,j)\right] \quad (4.2)$$

where g represents the fluxes in the axial direction, f represents the fluxes in the radial direction, and c represents the source terms. The index i represents the radial direction while j represents the axial direction. For the fluid equations, g is evaluated using either flux vector splitting or straight upwinding, as described below. The f

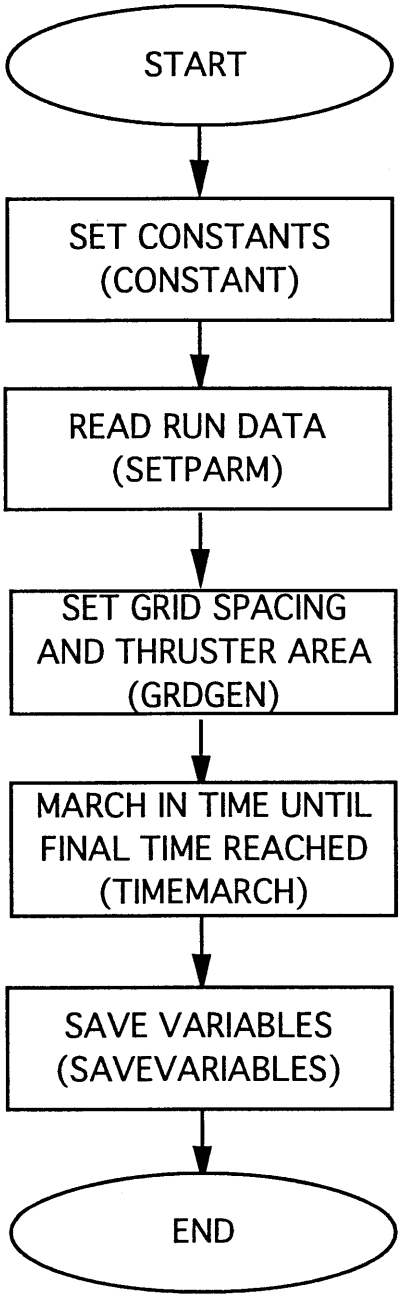

Figure 4-1: MPDAXI Flowchart, I

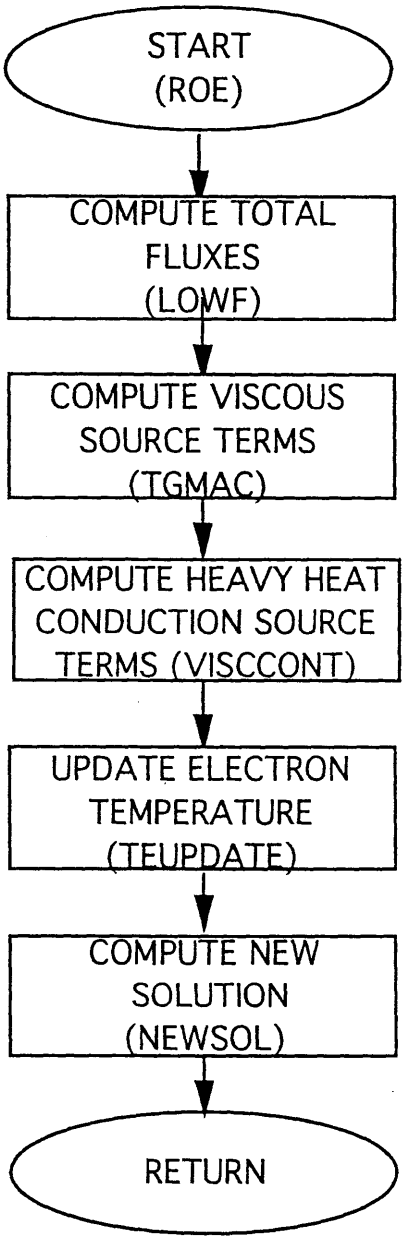

Figure 4-2: MPDAXI Flowchart, II

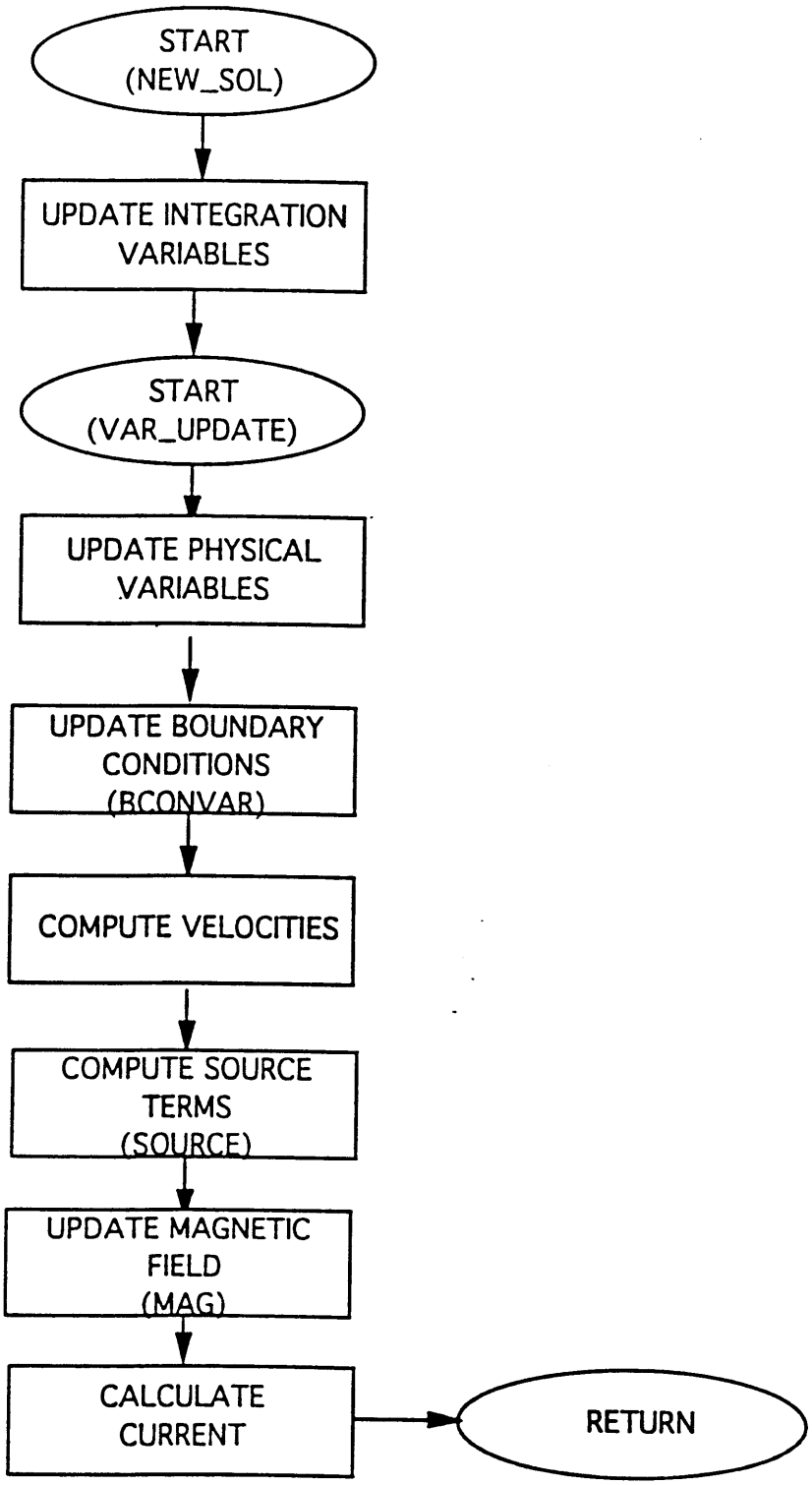

Figure 4-3: MPDAXI Flowchart, III

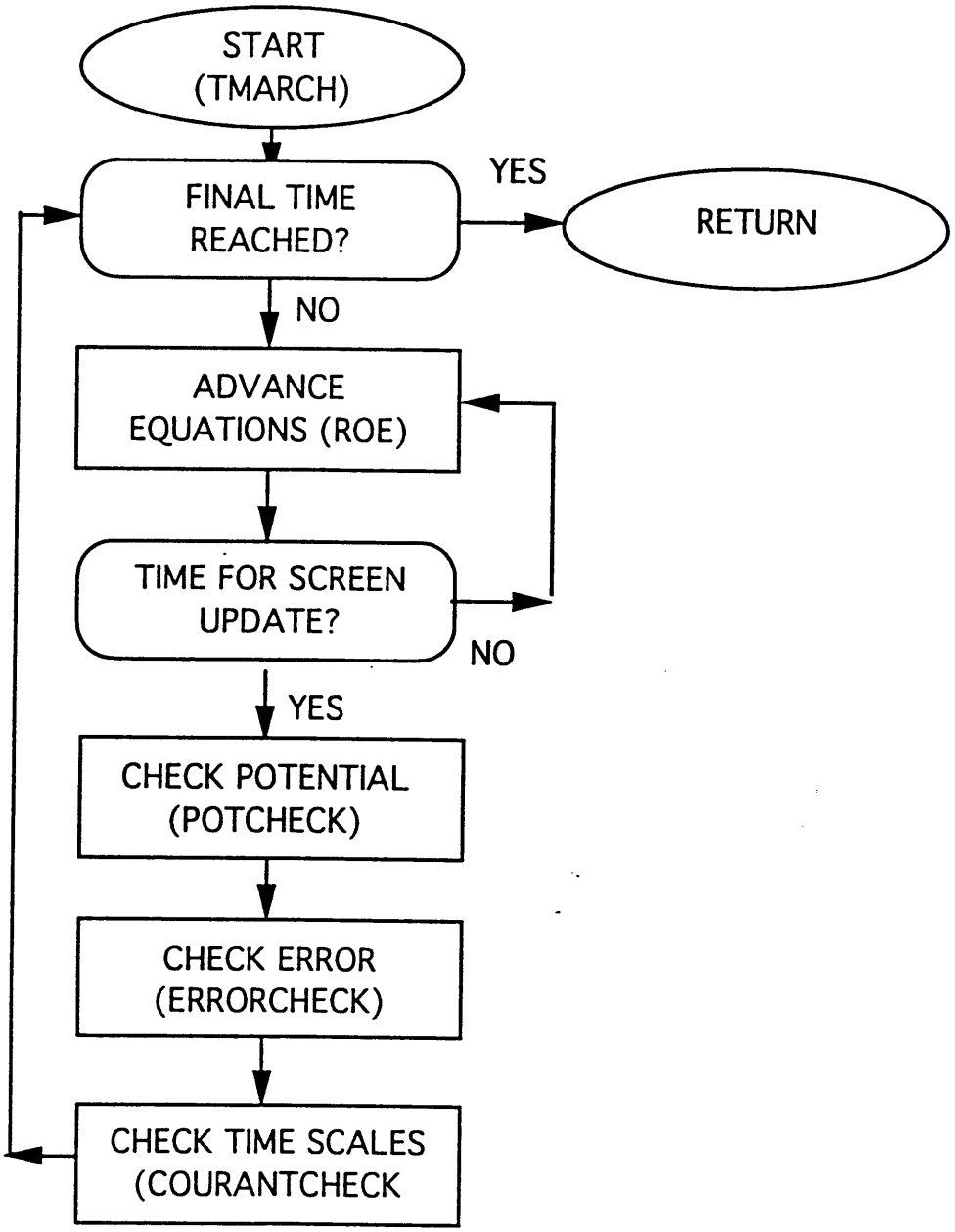

Figure 4-4: MPDAXI Flowchart, IV

terms are evaluated using a modified version of Rusanov's first order scheme. The electron temperature equation is updated using an ADI version of MacCormack's scheme, described below. The magnetic field equation is updated with a scheme developed for this research, also described below.

4.1.3 Axial Fluid Fluxes

The axial derivatives of the ion and neutral momentum and heavy species energy equations are evaluated using the Flux Vector Splitting (FVS) scheme of Steger and Warming [67]. FVS attempts to mimic the physical character of the fluid. When the flow is supersonic, the method reduces to upwinding, so that information only propagates in one direction. When the flow is subsonic, the eigenvectors of the derivative matrix are used to determine what information flows in what direction. The axial derivatives of the ion and neutral continuity equations are evaluated with simple upwinding. These schemes were chosen because of their simplicity, the inherent damping at the thruster inlet where the flow is subsonic, and the lack of damping in the bulk of the thruster where the flow is supersonic. For a variable vector given by

$$\mathbf{U}(i,j) = \left\{ \begin{array}{c} \rho_n \\ \rho_n V_{nz} \\ \rho_n V_{nr} \\ \frac{3}{2}\rho\frac{k}{m_i}T_g \\ \rho_i \\ \rho_i V_{iz} \\ \rho_i V_{ir} \end{array} \right\}_{(i,j)}$$

the axial fluxes are given by

$$\mathbf{g}(i,j+\tfrac{1}{2}) = \left\{ \begin{array}{c} \rho_n V_{nz} \\ \rho_n \left[V_{nz}^2 + \frac{k}{m_i} T_g \right] \\ \rho_n V_{nz} V_{nr} \\ \frac{3}{2} \rho \frac{k}{m_i} T_g V_z \\ \rho_i V_{iz} \\ \rho_i \left[V_{iz}^2 + \frac{k}{m_i} (T_e + T_g) \right] \\ \rho_i V_{iz} V_{ir} \end{array} \right\}_{(i,j)}$$

if $V_z > a_i$ where $a_i = \sqrt{\frac{k}{m_i} \gamma (T_g + T_e)}$ and

$$\mathbf{g}_{i,j+\frac{1}{2}} = \left\{ \begin{array}{c} \rho_n V_{nz} \\ \frac{\rho_n}{\gamma} \left[(\gamma - 1) V_{nz}^2 + \frac{1}{2} (V_{nz} + a_n)^2 \right] \\ \frac{\rho_n}{\gamma} \left[(\gamma - 1) V_{nr} V_{nz} + \frac{1}{2} V_{nr} (V_{nz} + a_n) \right] \\ \frac{3}{2} \frac{k}{m_i} \frac{\rho T_g}{\gamma} \left[(\gamma - 1) V_z + \frac{1}{2} (V_z + a) \right] \\ \rho_i V_{iz} \\ \frac{\rho_i}{\gamma} \left[(\gamma - 1) V_{iz}^2 + \frac{1}{2} (V_{iz} + a_i)^2 \right] \\ \frac{\rho_i}{\gamma} \left[(\gamma - 1) V_{ir} V_{iz} + \frac{1}{2} V_{ir} (V_{iz} + a_i) \right] \end{array} \right\}_{(i,j)} + \left\{ \begin{array}{c} 0 \\ \frac{1}{2} \frac{\rho_n}{\gamma} [V_{nz} - a_n]^2 \\ \frac{1}{2} \frac{\rho_n}{\gamma} V_{nr} [V_{nr} - a_n] \\ \frac{3}{2} \frac{k}{m_i} \frac{\rho T_g}{\gamma} [V_z - a] \\ 0 \\ \frac{1}{2} \frac{\rho_i}{\gamma} [V_{iz} - a_i]^2 \\ \frac{\rho_i}{\gamma} V_{ir} [V_{ir} - a_i] \end{array} \right\}_{(i,j+2)}$$

if $V_z \leq a_i$, where $a_n = \sqrt{\frac{\gamma k T_g}{m_i}}$.

One of the main problems with the numerical simulation was obtaining converged solutions. The methods used to track convergence and the behavior of unconverged solutions are both detailed in Appendix D. There was some evidence that non-convergence was tied to an oscillation of the location of the current bend and sonic transition discussed in Chapter 6. Therefore, for some of the cases shown in Chapter 6, particularly the higher current cases, pure upwinding (rather than FVS) was used in the portion of the simulation region 3 mm or less from the anode radially and between 1 cm downstream of the inlet and 1 cm downstream of the end of the electrodes. This kept the solution from changing drastically as the location of the sonic transtion varied, and so enhanced the convergence of the simulation.

4.1.4 Transverse Fluid Fluxes

The transverse derivatives of the continuity, momentum, and heavy species energy equations are all evaluated using a slightly modified version of Rusanov's first order scheme [58]. The fluxes are given by

$$\mathbf{f}_{i+\frac{1}{2},j} =$$

$$\left\{ \begin{array}{c} \frac{1}{2}\rho_n V_{nz} \\ \frac{1}{2}\rho_n \left[V_{nz}^2 + \frac{k}{m_i} T_g\right] \\ \frac{1}{2}\rho_n V_{nz} V_{nr} \\ \frac{3}{4}\rho \frac{k}{m_i} T_g V_z \\ \frac{1}{2}\rho_i V_{iz} \\ \frac{1}{2}\rho_i \left[V_{iz}^2 + \frac{k}{m_i}(T_e + T_g)\right] \\ \frac{1}{2}\rho_i V_{iz} V_{ir} \end{array} \right\}_{(i,j)} + \left\{ \begin{array}{c} \frac{1}{2}\rho_n V_{nz} \\ \frac{1}{2}\rho_n \left[V_{nz}^2 + \frac{k}{m_i} T_g\right] \\ \frac{1}{2}\rho_n V_{nz} V_{nr} \\ \frac{3}{4}\rho \frac{k}{m_i} T_g V_z \\ \frac{1}{2}\rho_i V_{iz} \\ \frac{1}{2}\rho_i \left[V_{iz}^2 + \frac{k}{m_i}(T_e + T_g)\right] \\ \frac{1}{2}\rho_i V_{iz} V_{ir} \end{array} \right\}_{(i+1,j)} - \mathbf{q}'(i+\tfrac{1}{2},j)$$

where the vector $\mathbf{q}'$ is a second order damping term.

4.1.5 Explicit Damping Terms

Explicit dissipation terms are used to damp numerical instabilities for all of the equations in the transverse direction, and for the ion equations in the axial direction. The damping terms are proportional to the second derivative of the integration variables and are based on those used in the standard first order Rusanov scheme,

$$\text{Damping} = \frac{\partial}{\partial r}(W\frac{\partial \mathbf{U}}{\partial r}) = \mathbf{q}'(i+\frac{1}{2},j) - \mathbf{q}'(i-\frac{1}{2},j)$$

where $\mathbf{U}$ is the variable vector as above and W is a measure of the wave speed

$$W(i+\frac{1}{2},j) = \frac{1}{2}C_1(a(i,j) + V_r(i,j) + a(i+1,j) + V_r(i+1,j)).$$

So the damping terms are given by

$$\mathbf{q}'(i+\frac{1}{2},j) = C_1 \frac{|V_r(i,j)+V_r(i+1,j)+a(i,j)+a(i+1,j)|}{4}(\mathbf{U}(i+1,j)-\mathbf{U}(i,j)) \tag{4.3}$$

where the vector **U** is as given above (with a similar expression for the axial damping). The actual damping terms used are heavily modified versions of the above general formula. The individual damping terms for each equation are given in Appendix C. The effect of these damping terms on the solution is discussed in Appendix D.

4.1.6 Electron Temperature Equation

The electron temperature equation is solved using an ADI version of MacCormack's method. The equation is taken in the non-conservative form given in Equation 3.45. The axial and radial first order derivatives in T_e are evaluated with a first order difference in the positive direction in the predictor step and in the negative direction in the corrector step. The second order derivatives are evaluated with a centered difference in space. The radial direction is treated implicitly in the predictor step and the axial direction is treated explicitly. The resulting tridiagonal system is solved using Thomas's algorithm [1]. In the corrector step the reverse procedure is followed.

4.1.7 Magnetic Field Equation

The magnetic field equation is solved using the electric field values at the cell boundaries rather than using an equation based on explicit derivatives of the magnetic field. This is done to maintain a constant potential drop across the electrodes in the steady state solution. The magnetic field updates are given by

$$B_\theta^{n+1}(i,j) = B_\theta^n(i,j) + \Delta t \left[\frac{E_z(i+\frac{1}{2},j)-E_z(i-\frac{1}{2},j)}{\Delta r} - \frac{E_r(i,j+\frac{1}{2})-E_r(i,j-\frac{1}{2})}{\Delta z} \right] \tag{4.4}$$

The components of the electric field are based on the Ohm's law given in equations 3.29 and 3.30. The component of current in the same direction as the field is given by the magnetic field gradient from adjacent gridpoint to gridpoint, as given in equations

4.7 and 4.8. The rest of the terms in the electric field are given by the average of the electric field at adjacent grid points.

$$E_r(i,j+\frac{1}{2}) = \frac{J_r(i,j+\frac{1}{2})}{\sigma} + \frac{1}{2}\left(V_{iz}(i,j)B_\theta(i,j) - \frac{1}{en_e(i,j)}\frac{\partial P^*}{\partial r}(i,j) - \frac{1}{\mu_0 r(i,j)}B_\theta^2(i,j)\right)$$

$$+\frac{1}{2}\left(V_{iz}(i,j+1)B_\theta(i,j+1) - \frac{1}{en_e(i,j+1)}\frac{\partial P^*}{\partial r}(i,j+1) - \frac{1}{\mu_0 r(i,j+1)}B_\theta^2(i,j+1)\right) \tag{4.5}$$

and

$$E_z(i+\frac{1}{2},j) = \frac{J_z(i+\frac{1}{2},j)}{\sigma} - \frac{1}{2}\left(\frac{1}{en_e(i,j)}\frac{\partial P^*}{\partial z}(i,j) + V_{ir}(i,j)B_\theta(i,j)\right)$$

$$-\frac{1}{2}\left(\frac{1}{en_e(i+1,j)}\frac{\partial P^*}{\partial z}(i+1,j) + V_{ir}(i+1,j)B_\theta(i+1,j)\right) \tag{4.6}$$

where $P^* = P_e + \frac{B_\theta^2}{2\mu_0}$.

The current in the electric field definitions is given by

$$J_r(i,j+\frac{1}{2}) = -\frac{1}{\mu_0}\frac{B_\theta(i,j+1) - B_\theta(i,j)}{\Delta z(i,j)} \tag{4.7}$$

and

$$J_z(i+\frac{1}{2},j) = \frac{1}{\mu_0}\left(\frac{B_\theta(i+1,j) - B_\theta(i,j)}{\Delta r(i,j)} + \frac{B_\theta(i,j)}{r(i,j)}\right) \tag{4.8}$$

4.1.8 Limiters

A number of limiters are applied to the solution to keep it stable. Some of the limiters were only important in keeping the transient solutions from becoming unstable, but some of the limiters were still active when the simulation converged on a steady state solution. The limiters that were needed only during transients were

- The ion axial velocity was limited to a minimum of 25 m/sec.
- The ion radial velocity was limited to a minimum of -5000 m/sec and a maximum of 5000 m/sec.

These limiters have no effect on the steady state solution. The other limiters are active in the converged simulation at some power levels. They are

- The ionization fraction was forced to be greater than 1% and smaller than 99.5% in the interior of the simulation.
- The heavy species temperature was cut off at a maximum of 50,000 K and a minimum of 200 K.
- The electron temperature was cut off at 40,000 K.

The effect that these limiters might have in obscuring important physics is discussed in Appendix D.

4.1.9 Source Terms

Gradients in the source terms, including gradients of velocity, heavy species temperature, viscosity coefficient, and heat conduction coefficients in the transport terms, are evaluated using centered differences.

4.2 Boundary Conditions

Boundary conditions are perhaps one of the most important and most overlooked aspects of numerical computations. At each of the boundaries of the thruster many or all of the flow quantities must be specified. The nature of the equations at the boundary determines how many of the boundary parameters are determined by physical conditions external to the flow and how many from internal conditions necessitated by numerical considerations. In Euler flow in a channel for example, if the exit of the flow is supersonic, there are no physical boundary conditions at the exit. If the flow is subsonic at the exit, one physical boundary condition must be applied, usually the pressure external to the flow. For the inviscid flow of a single fluid with no electric or magnetic effects, the number of each type of boundary condition can be found using characteristic analysis. Thompson[69] describes a unified formalism for developing

boundary conditions for any system of first order hyperbolic equations based on characteristic ideas. However, the equations in the MPD model are not all first order or hyperbolic. The magnetic field equation, the momentum equations, and the energy equations all contain second order terms and the magnetic field and energy equations contain terms in which the derivative of one quantity is multiplied by the derivative of another. No formalism exists for the boundary conditions for such a complex system of equations. Therefore, the boundary conditions used are a mix of physical considerations, characteristic analysis of simplified models, and trial and error. The following subsections describe the boundary conditions used at each of the thruster boundaries. At each boundary there are nine unknowns, the ion and neutral densities, the ion radial and axial momentum, the neutral radial and axial momentum, the electron and heavy species temperatures, and the magnetic field strength.

4.2.1 Inlet Boundary Conditions

At the inlet there are four boundary conditions which are known. These are the total mass flow, the bulk radial velocity, the applied current, and the total enthalpy of the inlet gas. This leaves five conditions which must be specified by some other means. Four of these conditions are specified by simplifying assumptions. These are that

1. There is no axial slip at the inlet. In reality, Sheppard [59] has shown that there is a very narrow diffusive layer where ions move backwards towards the insulator plate, while the neutrals move forwards. However, the grid used for this research is too coarse to capture the neccessary level of detail.

2. There is no radial slip at the inlet.

3. The ionization fraction is small but finite (0.1%). Again, the actual value could only be determined by modeling the diffusive layer at the inlet.

4. The axial electron temperature gradient is zero. This assumption is based on the electron repelling potential of the backplate.

This leaves one condition to be determined. Because the inlet flow is assumed to be subsonic, this last boundary condition should come from the interior of the simulation region. The boundary condition used in the simulation is that the inlet pressure should be such that the axial momentum equation is balanced between the inlet and the first interior point. Once the pressure is set, all of the other variables follow from the previously described conditions. The density can be determined from the inlet total enthalpy given the mass flow per unit area,

$$h_{t0} = \frac{\gamma}{\gamma - 1}\frac{P(r, z = 0)}{\rho(r, z = 0)} + \frac{1}{2}V^2(r, z = 0) \tag{4.9}$$

so

$$\rho^2 h_{t0} - \rho\frac{\gamma}{\gamma - 1}P - \frac{1}{2}(\frac{\dot{m}}{A_{inlet}})^2 = 0 \tag{4.10}$$

as it is assumed that the radial velocity is zero

$$V_r(r, z = 0) = 0$$

so that

$$V^2(r, z = 0) = V_z^2(r, z = 0)$$

The inlet mass flow is assumed to be distributed so that the mass flow per unit area is constant, so once the local density is found the velocity is set to give the proper mass flow,

$$V_z(r, z = 0) = \frac{\dot{m}}{\rho(r, z = 0)\pi(R_a^2 - R_c^2)} \tag{4.11}$$

The applied current determines the magnetic field at the inlet according to the relation

$$B_\theta(r, z = 0) = -\frac{\mu_0 I}{2\pi r} \tag{4.12}$$

4.2.2 Exit Boundary Conditions

Again at the exit there are nine variables to be determined. The first boundary condition is that the exit of the channel is set to be far enough from the end of the

electrodes so that the magnetic field at the exit is uniformly zero. Two assumptions are made, that the ionization fraction and electron temperature are constant axially at the exit.

$$\alpha(i, NZ) = \alpha(i, NZ - 1)$$

$$T_e(i, NZ) = T_e(i, NZ - 1)$$

For the other six fluid variables at a given radial location, boundary conditions are determined by whether the exit flow at that radial location is subsonic or supersonic. If the flow is supersonic, the axial gradient on all of the fluid variables is set to zero. This gives the other boundary conditions. If the flow is subsonic, the picture is more complicated. From characteristic theory for a single fluid, one boundary condition must come from outside of the simulation region. The outside pressure is chosen as the condition. Physically, the exit flow at the side walls sees the tank pressure as soon as it reaches the end of the walls. However, at the center of the exiting jet, far from the electrode, the fluid only sees the pressure of the fluid around it. So, if the exit flow at either electrode is subsonic (which it almost always is), the pressure is set to an assumed small tank pressure (typically 10 Pa). In order to allow this low pressure to propagate to the center of the exit flow, the pressure at any other subsonic radial location is set to half of the values at the simulation points right above and right below it.

$$P(i, NZ) = \frac{1}{2}(P_{exit}(i + 1) + P_{exit}(i - 1))$$

where $P_{exit}(i) = \begin{cases} 10Pa & \text{if } i = 0 \text{ or } i = NR \\ P(i, NZ) & \text{otherwise} \end{cases}$

Once the information from outside is determined, the other information comes from the interior. The boundary conditions for density, heavy species temperature, and the velocities then come from characteristic theory as described in Appendix B and are given by

$$V_r(i, NZ) = V_r(i, NZ - 1)$$

$$V_{ir}(i, NZ) = V_{ir}(i, NZ - 1)$$

$$B_\theta(i,NZ) = 0$$

$$\rho(i,NZ) = \sqrt{\frac{P(i,NZ)m_i\rho(i,NZ-1)}{k(T_g(i,NZ-1)+\alpha(i,NZ-1)T_e(i,NZ-1))}}$$

$$T_g(i,NZ) = (T_g(i,NZ-1)+\alpha(i,NZ-1)T_e(i,NZ-1))\frac{\rho(i,NZ)}{\rho(i,NZ-1)}$$

$$-\alpha(i,NZ-1)T_e(i,NZ-1)$$

$$V_z(i,NZ) = V_z(i,NZ-1)$$

$$-\frac{1}{2}\sqrt{\frac{\gamma k}{m_i}[T_g(i,NZ-1)+\alpha(i,NZ-1)T_e(i,NZ-1)]}\log\frac{\rho(i,NZ)}{\rho(i,NZ-1)}$$

$$V_{nz}(i,NZ) = V_{nz}(i,NZ-1)$$

$$-\frac{1}{2}\sqrt{\frac{\gamma k}{m_i}[T_g(i,NZ-1)+\alpha(i,NZ-1)T_e(i,NZ-1)]}\log\frac{\rho(i,NZ)}{\rho(i,NZ-1)}$$

and

$$V_{iz}(i,NZ) = \frac{V_z(i,NZ)-(1-\alpha)V_{nz}(i,NZ)}{\alpha(i,NZ)}$$

4.2.3 Insulating Side Wall Boundary Conditions

In the geometries modeled short insulating sections are attached to the ends of the electrodes. As at the inlet and exit, nine boundary conditions must be specified. Again, the magnetic field comes from physical considerations. Because no current attaches to the thruster downstream of these sections, the magnetic field at these insulating side walls must be zero. Also, physically there is no flow through the wall, so the bulk radial velocity at the wall is zero. The seven remaining boundary conditions on the fluid variables come from a combination of assumptions and characterisitic theory. The axial velocity of both ions and neutrals is assumed to be zero. The ion radial neutral velocity is assumed to be equal to the Bohm velocity, V_b directed into the wall, where

$$V_b = \sqrt{\frac{k}{m_i}(T_e+\frac{5}{3}T_g)}. \tag{4.13}$$

The electron number density is found from characteristic theory assuming that the ions can be treated separately from the neutral particles. As given in Appendix B

the resulting boundary condition for the electron number density is

$$\rho_i^{n+1}(NR,j) = \rho_i^n(NR,j) - \Delta t \left[\frac{2V_{ir}(NR,j)(\rho_i^n(NR,j) - \rho_i(NR-1,j))}{\Delta r(NR,j)} \right.$$

$$\left. + \frac{\rho_i^n(NR,j)(V_{ir}(NR,j) - V_{ir}(NR-1,j))}{\Delta r(NR,j)} - m_i \dot{n}_e(NR,j) \right] \qquad (4.14)$$

The heavy species temperature is set to 3000 K and the transverse gradient of the electron temperature is set to zero. At the upper side wall the neutral density gradient is set to zero and the total density is taken as the sum of the species densities. At the lower side wall the total density is set by balancing the total radial momentum equation. The neutral density is then set by differencing the total density and the ion density.

4.2.4 Cathode Boundary Conditions

At the cathode the same boundary conditions are applied as at the insulating sections, except that the magnetic field must be such that the parallel electric field at the cathode is zero. In discretized form this condition becomes

$$B_\theta(0,j) = \frac{1}{1 + V_{ir}(0,j)\mu_0\sigma(0,j)\Delta r(0,j)} \left[\frac{r(1,j)}{r(0,j)} B_\theta(1,j) \right.$$

$$\left. - \frac{\sigma(0,j)\mu_0 \Delta r(0,j)}{2e\Delta z(0,j)} (P^*(0,j+1) - P^*(0,j-1)) \right]. \qquad (4.15)$$

Solving this equation for the magnetic field at j using the previous values of the magnetic field at j-1 and j+1 often becomes unstable. This is because of a CFL type restriction on the transverse cell size for a given axial grid spacing. Therefore, a relaxation technique is used where the magnetic field at point j is set equal to a weighted average of the value given by Equation 4.15 and the previous value.

4.2.5 Anode Boundary Conditions

The boundary conditions for the ion and neutral velocities, the electron and heavy species temperatures, and the neutral density are the same as at the insulating sections or the cathode. The magnetic field and electron number density at the anode come from the near anode model described in Chapter 5.

4.3 Coordinate Transformations

In certain regions of the thruster, particularly near the anode, the inlet, and the end of the electrodes, the fluid undergoes large changes over small length scales. In these regions, in order to preserve the accuracy of the calculations, the grid spacing must be quite fine. In other regions, such as in the center of the channel and between the insulating sections of the side walls, the fluid properties are relatively constant. Here the grid spacing can be much coarser without leading to accuracy problems. Therefore, variable grid spacing is used to reduce the number of grid points needed. A grid with variable spacing is obtained using techniques described below. Then, the governing equations are transformed to a new coordinate space (η,ξ) in which the grid points are uniformly spaced. The transformation of the governing equations is also described below. The transformed equations are then solved using the numerical method described in Section 4.1

4.3.1 Coordinate Transformation

The transformation from one space to another is made using the relationships

$$\frac{\partial}{\partial r} = \frac{\partial \eta}{\partial r}\frac{\partial}{\partial \eta} + \frac{\partial \xi}{\partial r}\frac{\partial}{\partial \xi} = \eta_r \frac{\partial}{\partial \eta} + \xi_r \frac{\partial}{\partial \xi} \tag{4.16}$$

and

$$\frac{\partial}{\partial z} = \frac{\partial \eta}{\partial z}\frac{\partial}{\partial \eta} + \frac{\partial \xi}{\partial z}\frac{\partial}{\partial \xi} = \eta_z \frac{\partial}{\partial \eta} + \xi_z \frac{\partial}{\partial \xi}. \tag{4.17}$$

From Anderson[1], the metrics are given by

$$\eta_r = \frac{z_\xi}{G},$$

$$\eta_z = -\frac{r_\xi}{G},$$

$$\xi_r = -\frac{z_\eta}{G},$$

and

$$\xi_z = \frac{r_\eta}{G}$$

where the Jacobian, G, is given by

$$G = r_\eta z_\xi - r_\xi z_\eta$$

Inserting the metrics into equations 4.16 and 4.17 gives

$$\frac{\partial}{\partial r} = \frac{1}{G}(z_\xi \frac{\partial}{\partial \eta} - z_\eta \frac{\partial}{\partial \xi}) \tag{4.18}$$

and

$$\frac{\partial}{\partial z} = \frac{1}{G}(r_\eta \frac{\partial}{\partial \xi} - r_\xi \frac{\partial}{\partial \eta}). \tag{4.19}$$

The second derivative in transformed space is found by taking the first derivative of the first derivative,

$$\frac{\partial^2}{\partial r^2} = \frac{\partial}{\partial r}(\frac{\partial}{\partial r}) = \frac{1}{G^2}\left[z_\xi^2 \frac{\partial^2}{\partial \eta^2} - 2 z_\xi z_\eta \frac{\partial^2}{\partial \xi \partial \eta} + z_\eta^2 \frac{\partial^2}{\partial \xi^2}\right] + \eta_{rr}\frac{\partial}{\partial \eta} + \xi_{rr}\frac{\partial}{\partial \xi} \tag{4.20}$$

and

$$\frac{\partial^2}{\partial z^2} = \frac{\partial}{\partial z}(\frac{\partial}{\partial z}) = \frac{1}{G^2}\left[r_\eta^2 \frac{\partial^2}{\partial \xi^2} - 2 r_\xi r_\eta \frac{\partial^2}{\partial \xi \partial \eta} + r_\xi^2 \frac{\partial^2}{\partial \eta^2}\right] + \eta_{zz}\frac{\partial}{\partial \eta} + \xi_{zz}\frac{\partial}{\partial \xi} \tag{4.21}$$

where

$$\eta_{rr} = \frac{z_\xi}{G}(\frac{z_{\xi\eta}}{G} - \frac{z_\xi}{G^2}G_\eta) - \frac{z_\eta}{G}(\frac{z_{\xi\xi}}{G} - \frac{z_\xi}{G^2}G_\xi), \tag{4.22}$$

$$\eta_{zz} = \frac{r_\eta}{G}(-\frac{r_{\xi\xi}}{G} + \frac{r_\xi}{G^2}G_\xi) - \frac{r_\xi}{G}(-\frac{r_{\xi\eta}}{G} - \frac{r_\xi}{G^2}G_\eta), \tag{4.23}$$

$$\xi_{rr} = \frac{z_\xi}{G}(-\frac{z_{\eta\eta}}{G} + \frac{z_\eta}{G^2}G_\eta) - \frac{z_\eta}{G}(-\frac{z_{\xi\eta}}{G} + \frac{z_\eta}{G^2}G_\xi), \tag{4.24}$$

and

$$\xi_{zz} = \frac{r_\eta}{G}(\frac{r_{\eta\xi}}{G} - \frac{r_\eta}{G^2}G_\xi) - \frac{r_\xi}{G}(-\frac{r_{\eta\eta}}{G} - \frac{r_\eta}{G^2}G_\eta). \tag{4.25}$$

By similar manipulations, the mixed second derivative can be found,

$$\frac{\partial^2}{\partial r \partial z} = \frac{1}{G^2}\left[G\frac{\partial^2}{\partial r \partial z} - r_\xi z_\xi \frac{\partial^2}{\partial \eta^2} - z_\eta r_\eta \frac{\partial}{\partial \xi^2}\right] + V1\frac{\partial}{\partial \xi} + V2\frac{\partial}{\partial \eta} \tag{4.26}$$

where

$$V1 = \frac{1}{G^2}\left[z_\xi r_{\eta\eta} - z_\eta r_{\eta\xi} - \frac{1}{G}(z_\xi r_\eta G_\eta - z_\eta r_\eta G_\xi)\right] \tag{4.27}$$

and

$$V2 = \frac{1}{G^2}\left[z_\eta r_{\xi\xi} - z_\xi r_{\eta\xi} - \frac{1}{G}(z_\eta r_\xi G_\xi - z_\xi r_\xi G_\eta)\right]. \tag{4.28}$$

These transformations are used to replace the derivatives in the equations which make up any of the given models used in the research. For example, the global continuity equation as given by 3.10 is transformed to

$$\frac{\partial \rho}{\partial t} + \frac{\partial}{\partial \eta}(\rho \hat{V}_r) + \frac{\partial}{\partial \xi}(\rho \hat{V}_z) = -\frac{\rho V_r}{r} \tag{4.29}$$

where the contravariant velocities are given by

$$\hat{V}_r = \frac{1}{G}(V_r z_\xi - V_z r_\xi)$$

and

$$\hat{V}_z = \frac{1}{G}(V_z x_\eta - V_r x_\eta).$$

All of the equations are given in their transformed form in Appendix A.

4.3.2 Grid Generation and Grids Used

In order to take advantage of the transformation of the equations, it is necessary to generate a grid with points clustered in the regions of the thruster where steep gradients occur. The grids in this research are generated using differential equation methods, as described by Anderson [1] and modified somewhat by Giles [21]. Two partial differential equations

$$\frac{\partial}{\partial r}(\varpi\frac{\partial \xi}{\partial r}) + \frac{\partial}{\partial z}(\varpi\frac{\partial \xi}{\partial z}) = 0 \tag{4.30}$$

and

$$\frac{\partial}{\partial r}(\varpi\frac{\partial \eta}{\partial r}) + \frac{\partial}{\partial z}(\varpi\frac{\partial \eta}{\partial z}) = 0 \tag{4.31}$$

are transformed to the computational space. In these equations, ϖ represents a variable conductivity which controls the grid spacing. In computational space, the equations become Poisson type equations of the form,

$$(z_\eta^2 + r_\eta^2)z_{\xi\xi} - 2(z_\xi r_\eta + r_\xi r_\eta)z_{\xi\eta} + (z_\xi^2 + r_\xi^2)z_{\eta\eta} = \frac{G}{\varpi}(\varpi_\xi r_\eta - \varpi_\eta r_\xi) \tag{4.32}$$

and

$$(z_\eta^2 + r_\eta^2)r_{\xi\xi} - 2(z_\xi r_\eta + r_\xi r_\eta)r_{\xi\eta} + (z_\xi^2 + r_\xi^2)r_{\eta\eta} = -\frac{G}{\varpi}(\varpi_\xi z_\eta - \varpi_\eta z_\xi) \tag{4.33}$$

The last two equations are solved using a Gauss-Seidel successive over relaxation procedure, which gives the r and z values for each point in the η, ξ space. These values are then used to find the metrics used above in the coordinate transformations by centered differencing at each of the interior points, and by one sided differencing where necessary at the boundary points.

The actual grid used contains 51 points (NR = NZ = 50). The electrodes end at the 41 point (j = 40). The grid is heavily concentrated near the anode and somewhat concentrated near the cathode. The grid is shown in Figure 4-5

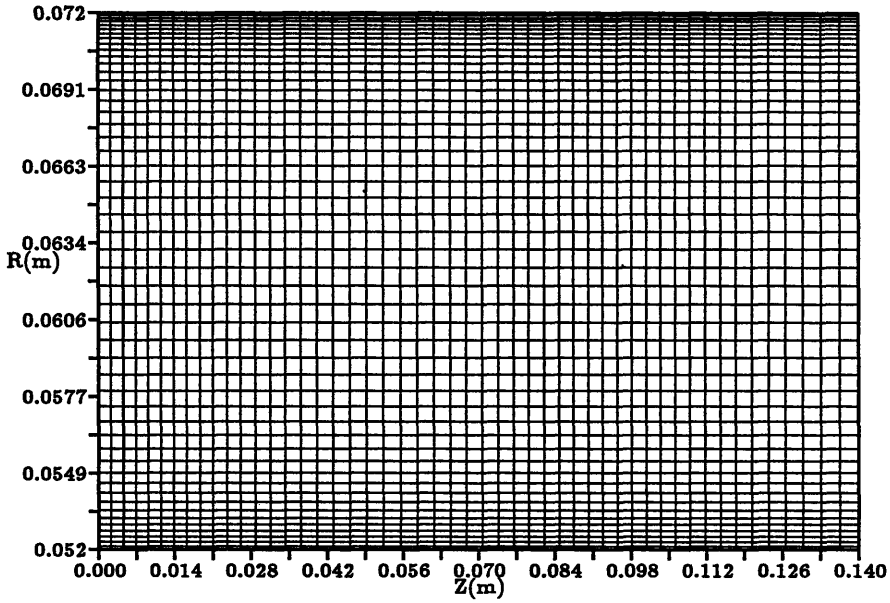

Figure 4-5: Grid

Chapter 5

Near Anode Model

If there were such a thing as an ideal thruster without the Hall effect, there would be no axial current and the current would run straight from electrode to electrode. However, due to the Hall effect there is axial current, the magnitude of which is approximately given by

$$J_z \approx -\frac{\sigma B_\theta}{e n_e} J_r = \beta J_r \tag{5.1}$$

where β is the Hall parameter, $\beta = \frac{\sigma |B_\theta|}{e n_e}$ and the magnetic field is into the plane of the thruster and so has a negative sign. So, as the electron number density decreases, the Hall parameter and the axial current increase. This axial current leads to high radial Lorentz force, which must be approximately balanced by a radial pressure gradient:

$$\frac{\partial n_e k (T_e + T_g)}{\partial r} = -J_z B_\theta. \tag{5.2}$$

Since J_z and B_θ are both negative and T_e and T_g are expected to be relatively constant, the radial gradient of n_e must be negative. Therefore, n_e must decrease dramatically in the radial direction if J_z is large, as

$$\frac{\partial n_e}{\partial r} \approx -\frac{J_z B_\theta}{k(T_e + T_g)}.$$

So, low electron number density and high axial current can build on each other and lead to anode starvation.

Once the anode becomes starved, large radial electric fields will develop, as seen from Ohm's Law. The Hall component of the radial field, which is dominant, is given by

$$E_r \approx -\frac{1}{en_e} J_z B_\theta \tag{5.3}$$

Since n_e is small and J_z is large, the radial electric field can be quite large. That starvation can occur is relatively well accepted in the somewhat fractious MPD community. However, the width of the starved region, and therefore the extent of the voltage drop across it, has not been experimentally determined. If this field is large enough and occurs over a wide enough region, the voltage drop across the starved region can be significant.

Probably the first model of anode starvation is that of Bakhst. Bakhst's [4] focus was on determining when starvation occurs, but his model also predicts the resulting voltage drop. Bakhst assumes that the axial electric field is zero

$$E_z = \frac{J_z}{\sigma} + \frac{J_r B_\theta}{en_e} = 0 \tag{5.4}$$

with the axial electron pressure gradient and ion velocity neglected. The axial current is therefore given by

$$J_z = -\frac{\sigma B_\theta}{en_e} J_r \tag{5.5}$$

From the radial momentum equation, neglecting the radial momentum and all of the source terms except for the Lorentz force,

$$\frac{\partial}{\partial r}(P_e + P_i) = -J_z B_\theta \tag{5.6}$$

Assuming that the ion and electron temperatures are constant radially yields

$$\frac{\partial n_e}{\partial r} = \frac{\sigma B_\theta^2 J_r}{en_e k(T_e + T_g)}. \tag{5.7}$$

If B_θ and J_r are constant radially then

$$n_e(r) = \sqrt{\frac{2\sigma B_\theta^2 J_r (r - r_a)}{ek(T_e + T_g)} + n_{e0}^2}. \tag{5.8}$$

The contribution to the radial electric field from the Hall and electron pressure terms is then

$$E_{r,Hall} = -\frac{1}{en_e}(J_z B_\theta + \frac{\partial P_e}{\partial r}) = \frac{\sigma B_\theta^2 J_r}{(en_e)^2} \frac{T_g}{T_e + T_g} \tag{5.9}$$

The potential drop across the near anode layer is then given by

$$\Delta V(anode) = \int_{r_{outer}}^{r_a} E_r dr = \frac{kT_g}{2e} \ln \frac{k(T_e + T_g)en_{e0}^2}{(r_{outer} - r_a)2\sigma B_\theta^2 J_r + k(T_e + T_g)en_{e0}^2}. \tag{5.10}$$

Bakhst assumes that the anode current density will be due to the random electron thermal flux to the wall, so that

$$n_{e0} = -\frac{4J_r}{e\bar{C}}$$

For the baseline case of Chapter 6, at the last inner point before the anode midway down the electrode, $T_e = 23,000K, T_g = 3200K, B_\theta = 0.0726T, \sigma = 3580\frac{Si}{m}$, and $J_r = -2.08 \times 10^{-5}\frac{A}{m^2}$. So, $\bar{C} = 591,000m/s$ and, to get the right thermal flux, $n_{e0} = 8.8 \times 10^{18}$. The last interior point is at $r = 0.071906m$ while $r_a = 0.072m$. The resulting potential drop over the last cell would be -1.09 Volts. The distribution of the electron number density, the radial electric field, and the potential drop are shown in Figures 5-1 - 5-3.

However, this Bakhst formulation neglects a number of effects, particularly in the transverse momentum equation. In order to get a more accurate determination of the electron number density and magnetic field at the wall, a somewhat more complete model has been developed. This model also assumes that the axial electric field is zero throughout the near anode region,

$$\frac{1}{\mu_0 \sigma r}\frac{\partial r B_\theta}{\partial r} = V_{ir} B_\theta + \frac{1}{en_e}\frac{\partial}{\partial z}\frac{B_\theta^2}{2\mu_0} + \frac{1}{en_e}\frac{\partial}{\partial z} n_e k T_e \tag{5.11}$$

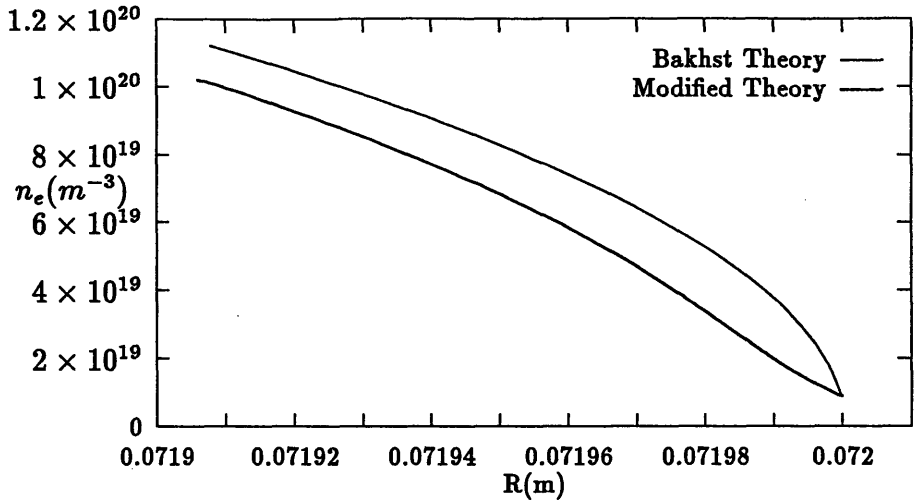

Figure 5-1: Electron Number Density, Analytical Models

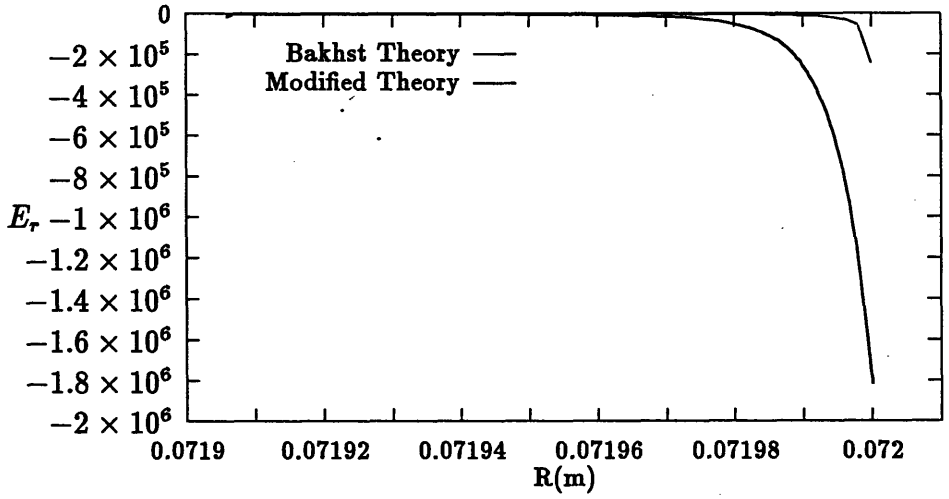

Figure 5-2: Radial Electric Field, Analytical Models

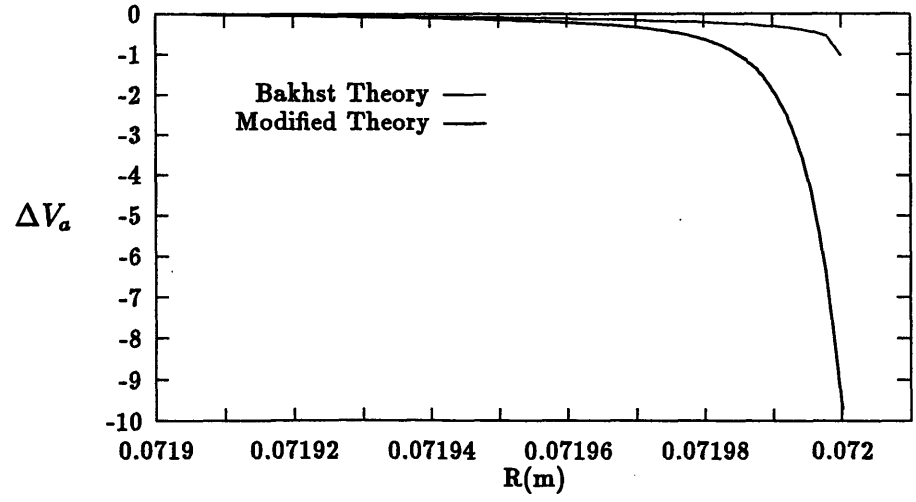

Figure 5-3: Anode Potential Drop, Analytical Models

where electron-neutral collisions have been neglected. Neglecting ion momentum, ion-neutral drag and viscosity, and radial temperature gradients, the transverse momentum equation for the charged species is given by

$$\frac{\partial n_e}{\partial r} = \frac{1}{k(T_g + T_e)} \left[-\frac{B_\theta}{\mu_0 r} \frac{\partial r B_\theta}{\partial r} + S_{ir} \right]. \tag{5.12}$$

The contribution from ion-neutral drag, at maximum, would be about 1% of the magnetic pressure drop across the cell. Ion momentum is included in the actual boundary condition used in the numerical simulation. The electron radial temperature gradient is assumed to be zero. Heavy species temperature and neutral velocity gradients are small and can probably be neglected. Even though the ion-neutral viscosity is 2-5 times larger than the ion-ion viscosity, due to the low ionization fraction, the radial gradients of the ion velocity are 100-1000 times larger than those of the neutral velocity. Therefore, the viscosity source term will be assumed to be given by

$$S_{ir} \approx \frac{4}{3} v_{ii} \frac{\partial^2 V_{ir}}{\partial r^2}.$$

Over the small transverse region being modeled, the change in the axial flow must be relatively small. Therefore,

$$\frac{\partial}{\partial r} \rho_i V_{ir} \approx 0 \tag{5.13}$$

Ionization over the short length being modeled could only change the overall ion flux by about 1%. Taking the appropriate derivatives,

$$\frac{\partial^2 V_{ir}}{\partial r^2} = -\frac{V_{ir}}{\rho_i} \frac{\partial^2 \rho_i}{\partial r^2} + \frac{2 V_{ir}}{\rho_i^2} \left(\frac{\partial \rho_i}{\partial r} \right)^2$$

The radial momentum equation can then be written as

$$\frac{\partial n_e}{\partial r} = \frac{-\sigma B_\theta f}{k(T_g + T_e)} + \frac{4}{3} \frac{v_{ii} V_{ir}}{n_e k (T_g + T_e)} \left[-\frac{\partial^2 n_e}{\partial r^2} + \frac{2}{n_e} \left(\frac{\partial n_e}{\partial r} \right)^2 \right] \tag{5.14}$$

where

$$f = V_{ir} B_\theta + \frac{B_\theta}{e n_e \mu_0} \frac{\partial B_\theta}{\partial z} + \frac{1}{e n_e} \frac{\partial}{\partial z} n_e k T_e = \frac{J_z}{\sigma}.$$

Rearranging,

$$\frac{\partial^2 n_e}{\partial r^2} = \frac{2}{n_e}(\frac{\partial n_e}{\partial r})^2 - \frac{3n_e}{4v_{ii}V_{ir}}\left[\sigma B_\theta f + k(T_g + T_e)\frac{\partial n_e}{\partial r}\right]. \tag{5.15}$$

The magnetic field is given by

$$\frac{\partial r B_\theta}{\partial r} = \mu_0 \sigma r f \tag{5.16}$$

and the Hall component of the radial electric field is given by

$$E_{r,Hall} = -\frac{1}{en_e}\left[\sigma B_\theta f + kT_e\frac{\partial n_e}{\partial r}\right] \tag{5.17}$$

For the one second order and one first order equation of the modified theory, three boundary conditions are needed. In order to match the Bakhst theory, the magnetic field and the electron number density at the anode were chosen as two of the boundary conditions. The third boundary condition was the radial derivative of n_e and was set equal to zero at the outer edge of the layer. For the same T_e, T_g and σ as used for the Bakhst model and with additional conditions that $v_{ii} = 7.3 \times 10^{-8}$ and $V_{ir}(d) = V_b$ at the wall and assuming $\frac{\partial P_e}{\partial z} = 0$, the solutions for this modified theory are given along with the Bakhst results in Figures 5-1 - 5-3.

The equations are solved by assuming a magnetic field and electron number density at the outer edge of the layer, $r = 0.071906$, and shooting to the electrode. If B_θ and n_e at the anode do not match the Bakhst values($B_\theta = 0.072$ and $n_e = 8.8 \times 10^{18}$) , the values at the outer edge are changed and the equations are again marched to the anode. The process is repeated until the desired anode conditions are obtained. The shooting is done with a variable step size Runge-Kutta algorithm. The total Hall potential drop across the near anode region predicted by this model is -9.68 Volts.

This modified theory is used to provide boundary conditions on the magnetic field and the electron number density at the anode. The flux into the anode layer from the plasma is set to the flux into the anode at the last iteration, where the flux is the product of the electron number density at the anode multiplied by the Bohm

velocity. The equations of the modified theory are marched to the anode along a grid of 50 equally spaced radial points, with the number of axial points determined by the number of points along the electrode. The radial current, or the axial magnetic field gradient, and the axial electron pressure gradient are taken from the previous (closer to the interior) axial line of the near anode grid. The change in the electron number density at each radial interval is limited to some percentage of the total value (typically 1 to 2%). The resulting radial potential drop across the grid at each axial location is then used to compute the electric field at the electrode and the interior side of the grid for use in the magnetic field calculation.

Chapter 6

Anode Starvation and Voltage Drops in the CAC Thruster

The most significant result of this research is the prediction of voltage drop less than 1 mm from the anode in the quasi-neutral region of the plasma. Section 6.1 describes the geometries of the experimental and numerical devices discussed in the remainder of the chapter. The experimental results of Heimerdinger and Kilfoyle are detailed in Section 6.2. Section 6.3 discusses the existence and cause of anode voltage drops in the baseline case. Finally, Section 6.4 describes the variation of the numerical results with different input currents.

6.1 The CAC Thruster

The experimental device on which this research concentrated was the Constant Area Channel (CAC) studied by Heimerdinger, Kilfoyle, and Martinez-Sanchez [25, 26, 24, 30]. This device was chosen because the experimental data was readily available at M.I.T. and because of its simple geometry. Also, the experimental results indicated that, in this type of thruster, anode starvation and onset were two separate phenomena, which would hopefully make the former easier to study. Onset, a large oscillation in the total voltage, is associated with large internal fluctuations of the plasma flow and increased thruster erosion. However, the bulk of the experimental work reported

by Heimeringer et. al. involved the Fully Flared Cathode (FFC), which differed from the CAC in the shape of the cathode, but was the same device in other respects. Results from the two thrusters will be treated somewhat interchangeably in the following discussion. Where necessary, a distinction will be drawn between the two devices.

The physical thruster was an axisymmetric device with the cathode as the inner electrode. Both the cathode and anode were 0.09 m long, with a constant outer radius for the cathode of the CAC of 0.053 m and a constant inner radius for the anode of 0.072 m. The FFC had a cathode which varied from 0.042 m outer radius at the inlet to 0.053 m at the throat to 0.033 m at the thruster exit. Current pulses of up to 3 $\times 10^{-4}$ sec were used, with currents ranging from 20 kA to 60 kA and a mass flow of $4 \times 10^{-3} \frac{kg}{s}$. Onset appeared to occur at approximately 60 kA.

The numerical thruster is depicted in Figure 6-1. It consists of two concentric cylinders, of which the first 0.109 m of each is conducting, followed by a short insulating section of 0.031 m. The dimensions of the numerical thruster are somewhat different than the physical thruster because of some confusion about the physical geometry when the first runs were done. The interelectrode gap is 0.02 m, with a cathode inner radius of 0.052 m. The plume is not included in the simulation. The mass flow of 4 $\times 10^{-3}$ kg/s is assumed to be injected through the whole backplate, with the mass flow per unit area constant at all radial locations. A number of different current levels, ranging from 23.4 kA up to 39.0 kA, were simulated. These currents are all well below the onset condition but span the region where large anode voltage drops develop. A baseline case of 31.2 kA will be discussed in this section. Variation between the different cases will be discussed in following sections.

6.2 Experimental Results

Heimerdinger[25] directly measured the anode voltage drop over a range of currents in the FFC and at 60kA in the CAC. The measured voltage drop is the difference

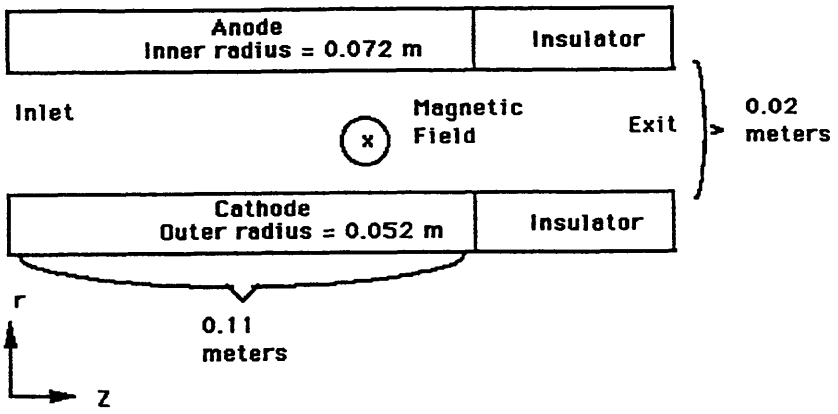

Figure 6-1: Numerical CAC Geometry

between the potential measured 2 mm from the anode at an axial location of 0.043 m from the inlet, and the potential at the anode. His data are shown in Figure 2-2. The data show that at low applied currents, anode voltage drops are negligible or non-existent. As the applied current is increased, the voltage drops appear and increase with increasing applied current. The anode drops seem to level out as the total current is increased past 50-55 kA, although the large error bars make this difficult to ascertain. The one data point available for the CAC seems to indicate that the anode voltage drop in this thruster is somewhat smaller than in the FFC. In general, the anode drops seem to account for 50 - 75 % of the total terminal voltage in those cases for which the anode seems to be starved, i.e. for currents above 25 kA or so.

Heimerdinger also presents other data which shed light on the voltage drops. He shows plots of enclosed current and floating potential for both the CAC and FFC at the 60 kA operating condition. The plots for the CAC are shown in Figures 2-3 and 2-1. The current plot indicates that the current is highly skewed near the anode, although it does not show the current within a mm of either electrode. The potential contours show that the anode voltage drops are significant along most of the thruster, but are substantially weaker within a cm of the inlet. Kilfoyle[30] shows a radial profile of the electron number density at the thruster exit plane. It shows that the electron density decreases from a maximum of 4 $\times 10^{21} m^{-3}$ at the cathode

to under 1.0 $\times 10^{20} m^{-3}$ 0.1 mm from the anode.

6.3 Cause of Starvation and Voltage Drops in the Baseline Case

As discussed in Chapter 1, simple theories and numerical models of MPD thrusters have always significantly underpredicted the total voltage of thrusters as observed in experiments. The data from Heimerdinger, as well as from other experiments discussed previously, indicate that the total voltage is distributed between a cathode fall voltage, a bulk plasma voltage, and an anode fall voltage. None of the existing theoretical or numerical results show the anode and cathode fall voltages, or adequately explain the cause of the anode falls. This is why the theoretical and numerical results predict so much lower voltages than those observed experimentally.

The model and simulation used in this research however does seem to reproduce the anode voltage drop behaviour seen by Heimerdinger. The anode voltage drops seen in the simulation occur in the quasi-neutral bulk plasma within a mm of the anode. The voltage drops appear even though the model uses fluid equations and does not include the non-neutral anode sheath. At low input total currents these voltage drops are not significant. As the input current is increased, the voltage drops appear and grow in magnitude, just as in Heimerdinger's data. These voltage drops occur because of the basic mechanism outlined in Chapter 5, as will be shown by the data presented herein.

Figure 6-2 shows the current lines for the baseline case, with the concentration of lines a measure of the current density. The plot is drawn so that the axial and radial dimensions are roughly in the correct proportions. The numbers on the plot indicate the approximate percentage of current enclosed by the nearest contour. As can be seen, the current is highly skewed near the anode, turning almost parallel to the electrode. This is because the axial component of the current is substantially larger than the radial component. The axial component is so large because the Hall parameter at the anode is quite large, reaching values as high as 100. Figure 6-3

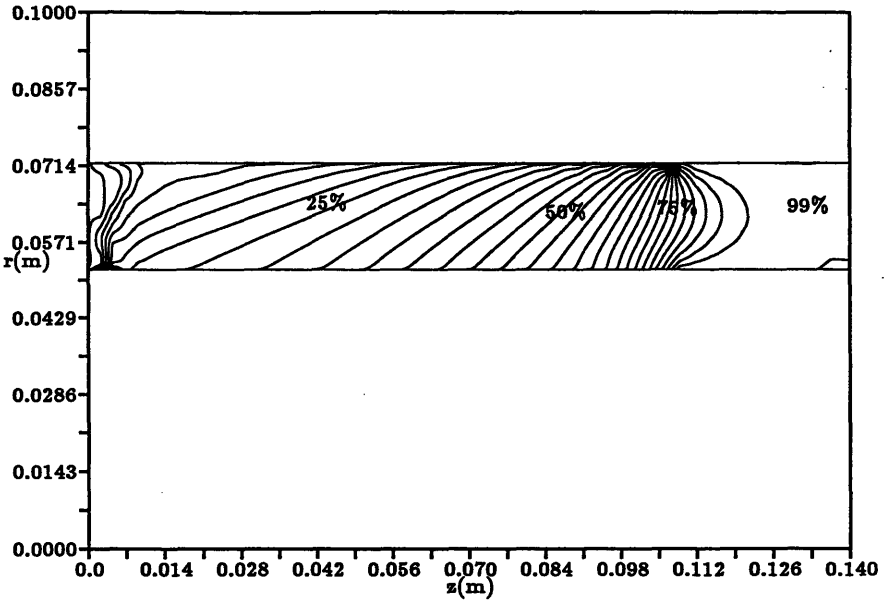

Figure 6-2: Current Lines in 31.2 kA CAC (Baseline)

shows contours of constant Hall parameter, with values shown at 5 locations. This region of high Hall parameter extends from within a cm of the thruster inlet until the end of the electrodes.

The Hall parameter is so high because of the low electron number density. The electron number density along five radial cuts is shown in Figure 6-4. The cuts are at the axial locations shown in the figure key. The electron number density decays from a maximum of $2 \times 10^{21} m^{-3}$ near the cathode to a minimum of $1 \times 10^{19} m^{-3}$ at the anode. The electron number density is dropping because both the ionization fraction and the total mass density are dropping near the anode. Radial cuts of these variables are shown in Figures 6-5 and 6-6 respectively. The ionization fraction is low near both the cathode and the anode due to recombination of the ions at the wall. The low ionization fraction near the cathode, and the slight (relatively) drop in electron density there leads to a small cathode voltage drop.

The electron number density near the anode is so low because the plasma has been turned away from the anode by the radial Lorentz force. This "turning away" takes place approximately 0.5 cm from the inlet. At the inlet, the plasma is not starved and there is a much smaller anode voltage drop, as shown in the constant potential contours of Figure 6-7. Within 1 cm from the base of the anode the potential drop has

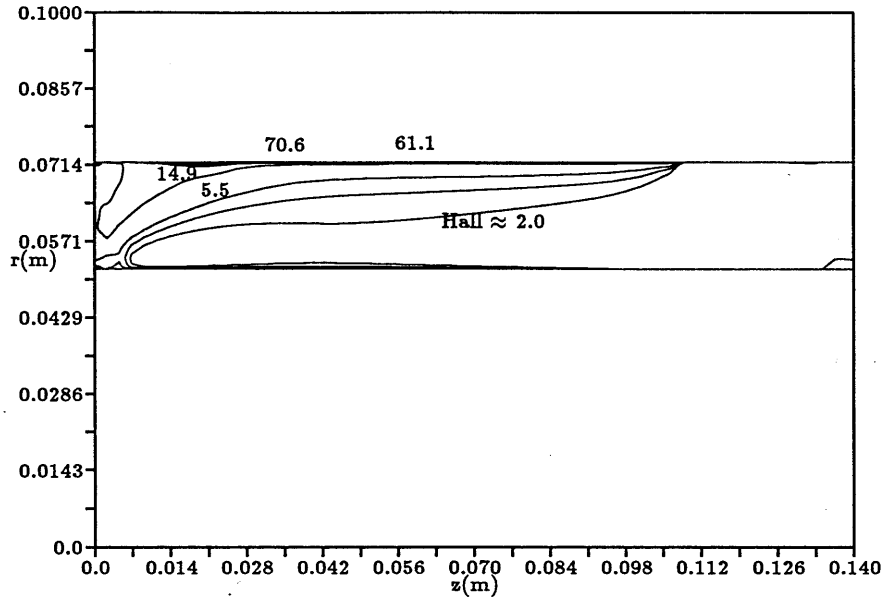

Figure 6-3: Constant Contours of Hall Parameter in 31.2 kA CAC (Baseline)

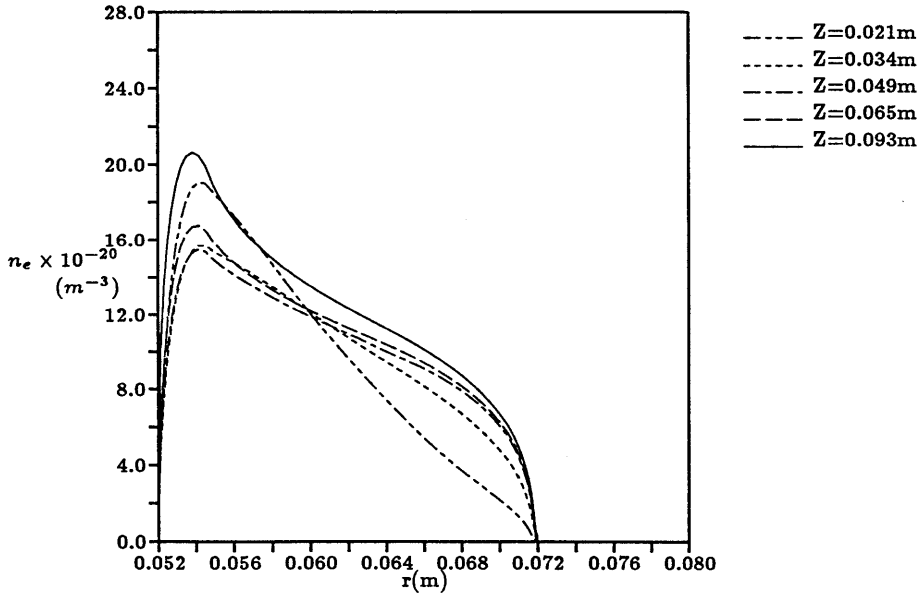

Figure 6-4: Radial Cuts of Electron Number Density in 31.2 kA CAC (Baseline)

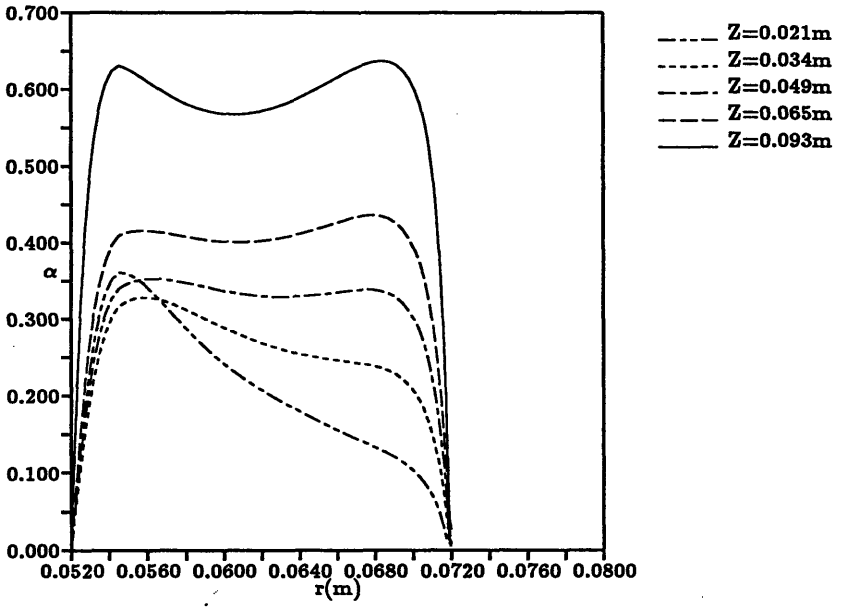

Figure 6-5: Radial Cuts of Ionization Fraction in 31.2 kA CAC (Baseline)

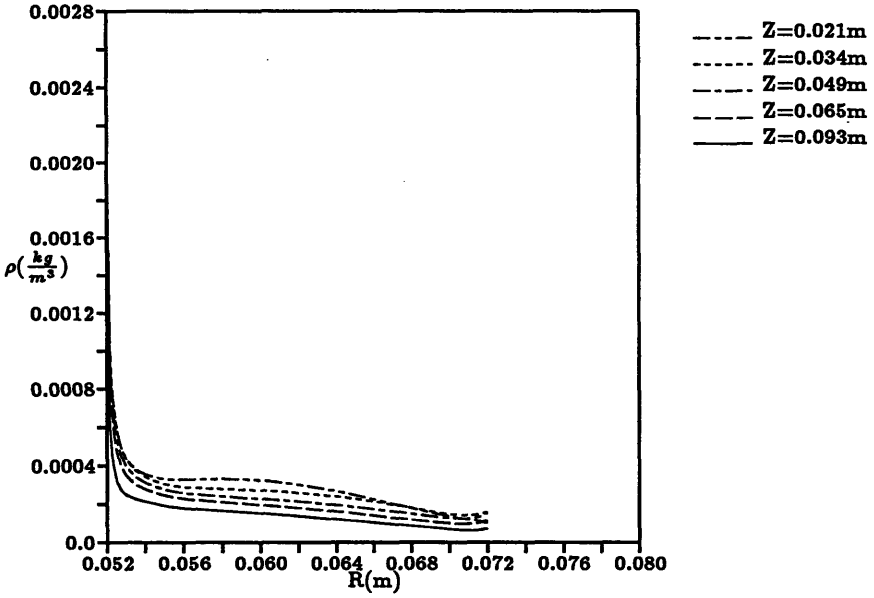

Figure 6-6: Radial Cuts of Total Mass Density in 31.2 kA CAC (Baseline)

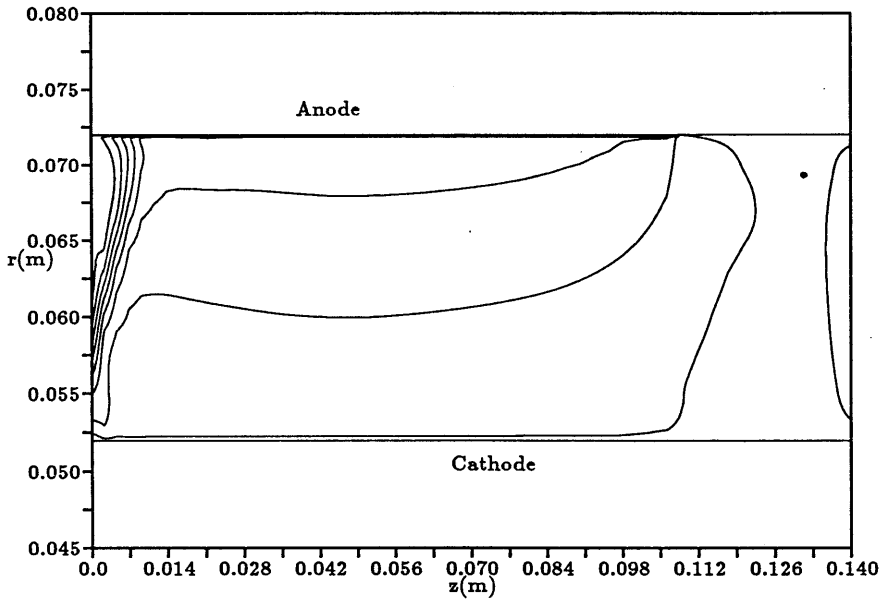

Figure 6-7: Constant Contours of Potential Drop in 31.2 kA CAC (Baseline)

spread itself down almost to the center line of the thruster. Mass density is relatively constant in the radial direction. Radial velocities are small as shown in Figure 6-8, constant contours of radial velocities. Numbers on the plot show values at the local minima (-582,-177,-61,-346 m/sec) and the maximum value (754 m/sec).

In this short unstarved portion of the near anode flow, the plasma is accelerated by the Lorentz forces to supersonic speeds. At the same time, the plasma is being turned away from the anode. This turn is shown in Figure 6-8 where there is a region of large negative radial velocity within 1 cm of the backplate. It is also illustrated by the streamlines, shown as the dotted lines in Figure 6-10. This turn is due to large radial Lorentz force near the center of backplate. This turn leads to depletion of the plasma near the anode, as shown by the isobars (solid lines) of Figure 6-10. The numbers on the plot indicate the pressure in Pascal at that location. As shown by the streamlines, the plasma then turns back so that it is flowing almost parallel to the anode. This turn is accompanied by a drop in Mach number, to subsonic speeds along some streamlines. The initial acceleration and subsequent drop in Mach number are shown in Figure 6-9, contours of constant Mach number. The label A is at a local maximum of 1.57. As shown by the labelled Mach 1 contour, along a number of axial lines the plasma is dropping from supersonic to subsonic speeds. This second

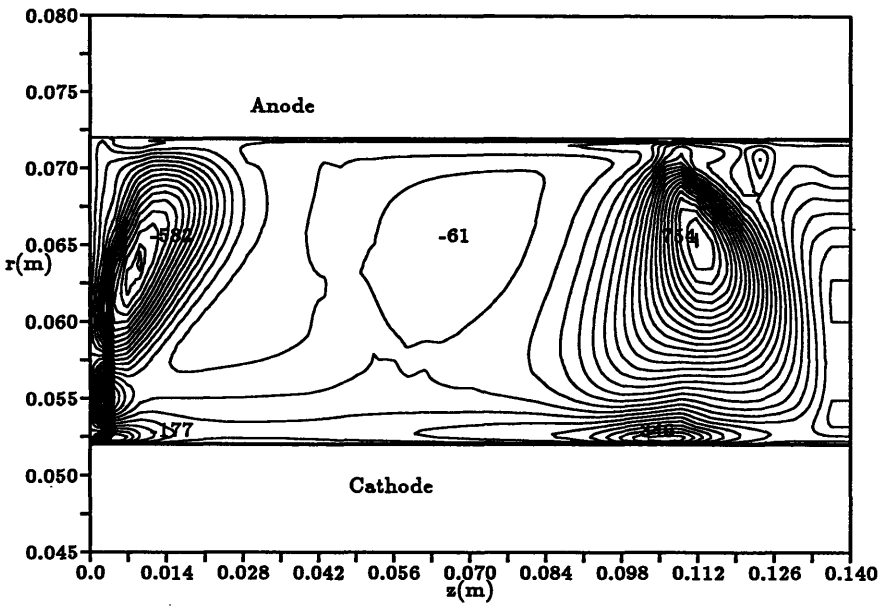

Figure 6-8: Radial Velocity Contours in 31.2 kA CAC (Baseline)

turn is perhaps due to an oblique shock. Some evidence of this shock is seen in the streamlines and isobars, which show that the turn and deceleration go together. Along streamlines within a cm from the anode the plasma first sees decreasing pressure as it accelerates, and then increasing pressure as the streamlines straighten out. This low pressure region is somewhat visible in the sharp dip and then slow rise in the electron number density 0.1 mm from the anode, shown in Figure 6-12. There is certainly not an increase in n_e as there is at the centerline due to ionization. The current lines (solid lines) and constant potential contours (dotted lines) shown in Figure 6-11, also show a sharp transition in this region. Very near the anode (within 0.1 mm) and along a ridge of high Hall parameter between z = 0.0015 and z = 0.0075, the current lines run almost parallel to the equipotentials, parallel to the anode within 0.1 mm of the anode, and parallel to the backplate along the ridge. Further along the channel, as the pressure increases and the Hall parameter decreases, the angle between the lines becomes larger.

When the plasma parameters at the last interior point are input to the near anode boundary equations, they predict significant voltage drops, as shown in Figure 6-13, transverse cuts of the potential drop.

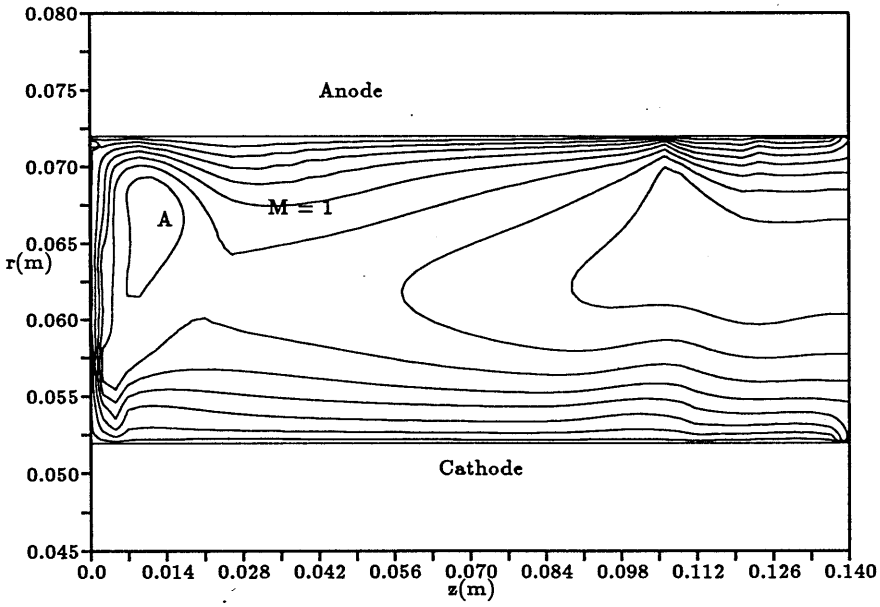

Figure 6-9: Mach Number Contours in 31.2 kA CAC (Baseline)

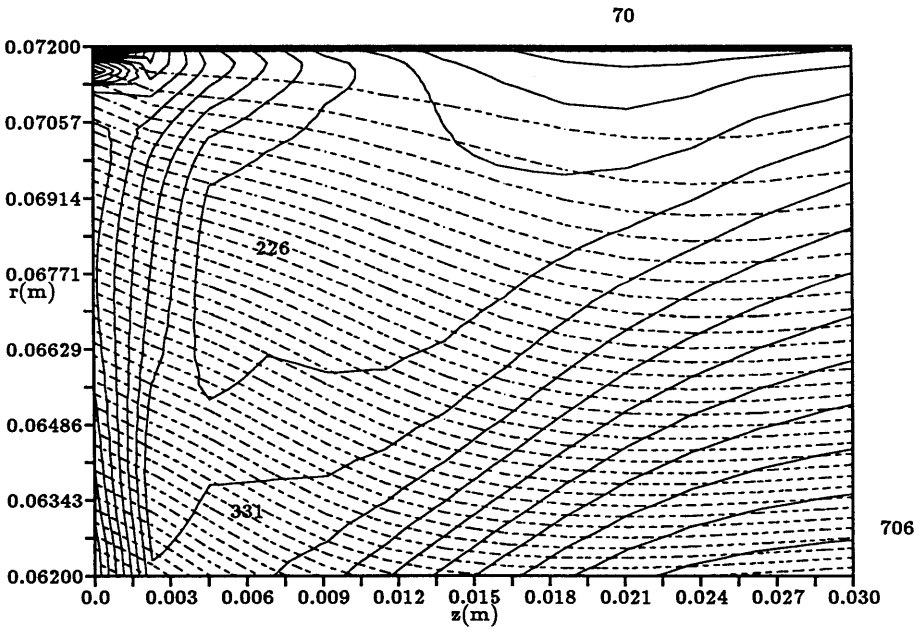

Figure 6-10: Stream Lines and Constant Pressure Contours (Baseline Case)

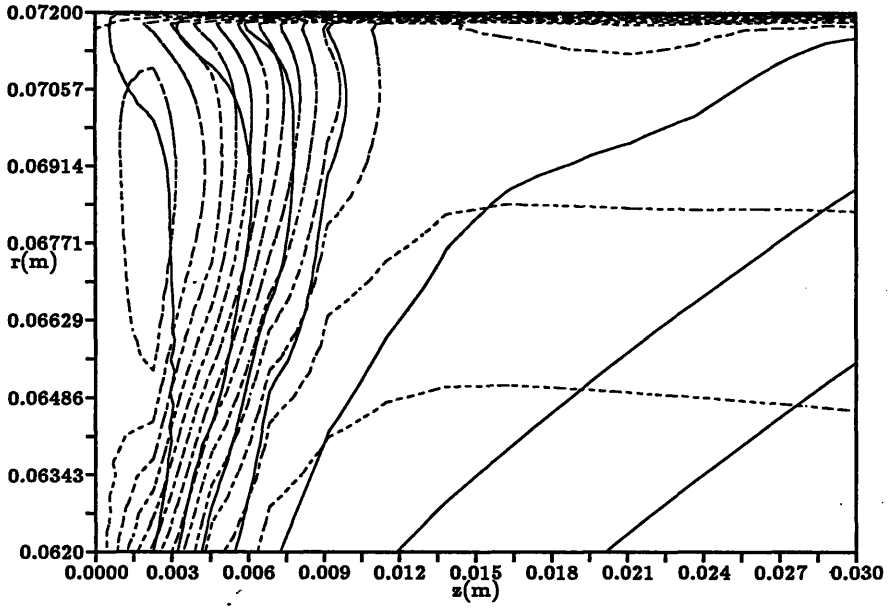

Figure 6-11: Current Lines and Constant Potential Contours (Baseline Case)

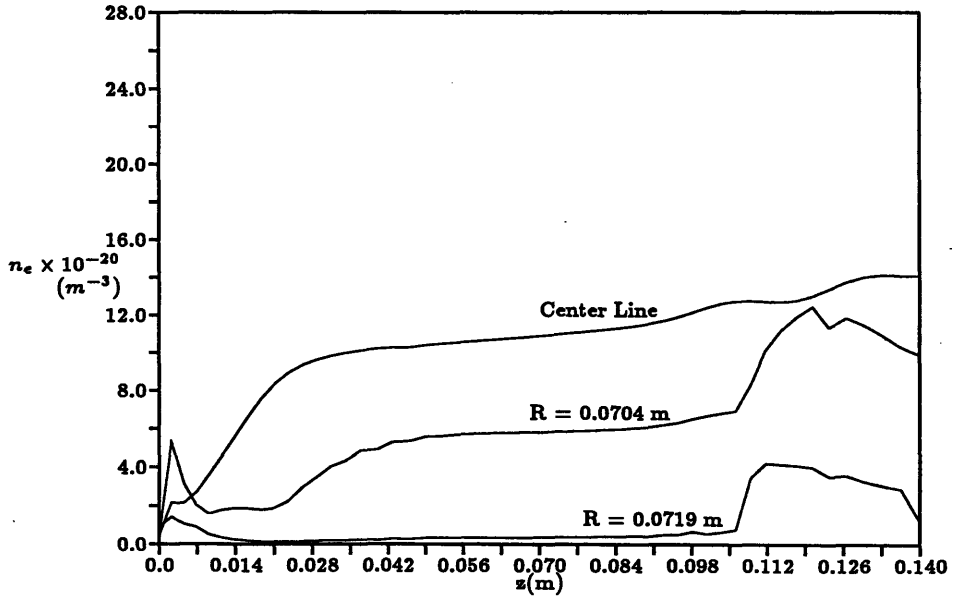

Figure 6-12: Axial Profiles of Electron Number Density in 31.2 kA CAC (Baseline)

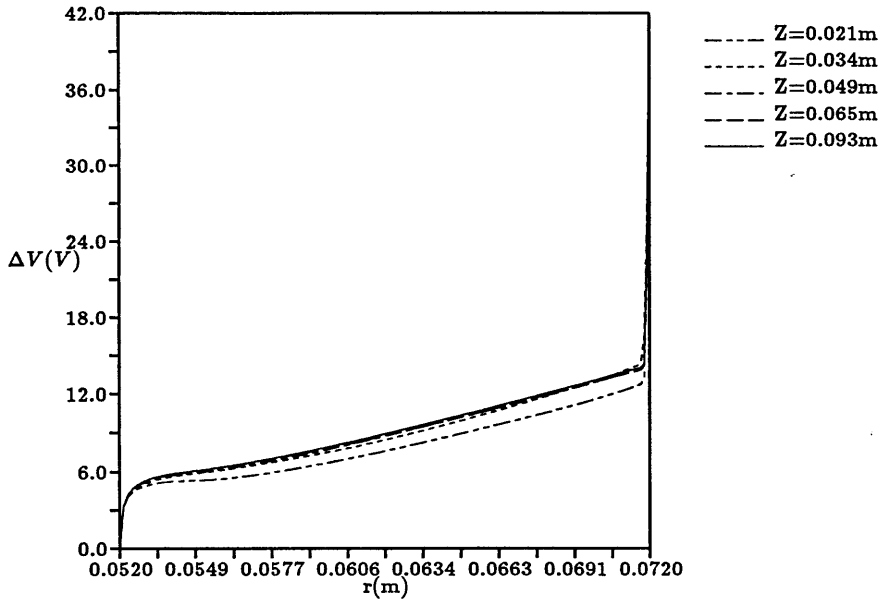

Figure 6-13: Radial Cuts of Potential Drop in 31.2 kA CAC (Baseline)

6.4 Current Variation

How do the anode voltage drops behave at different currents? Experimental evidence from Heimerdinger and others shows that below some critical current, the anode is not severely starved and voltage drops are not present. Above this current level, the voltage drops appear and grow with increasing current. Eventually, as the current increases, the voltage drops saturate and stay constant. Heimerdinger determined the voltage drop in the FFC at currents ranging from 20 kA up to 60 kA and in the CAC at 60 kA. Below 20 kA, the voltage drops appear to be small or non-existent and steady. From 20 kA to 50 kA, they grow dramatically with increasing current. Above 50 kA, they appear to be saturated.

The numerically predicted voltage drops behave in a similar manner. Simulations were performed for the CAC at currents of 23.4 kA, 27.3 kA, 31.2 kA, 35.9 kA, and 39.0 kA. The experimental and numerical voltage drops are all plotted in Figure 6-14. At 23.4 kA, the voltage drops are quite small. As current is increased, the numerically predicted anode voltage drops grow, like the experimental data. The total potential drops from the experimental data and the numerical simulation are shown in Figure 6-15. Agreement gets better as the current is increased, although

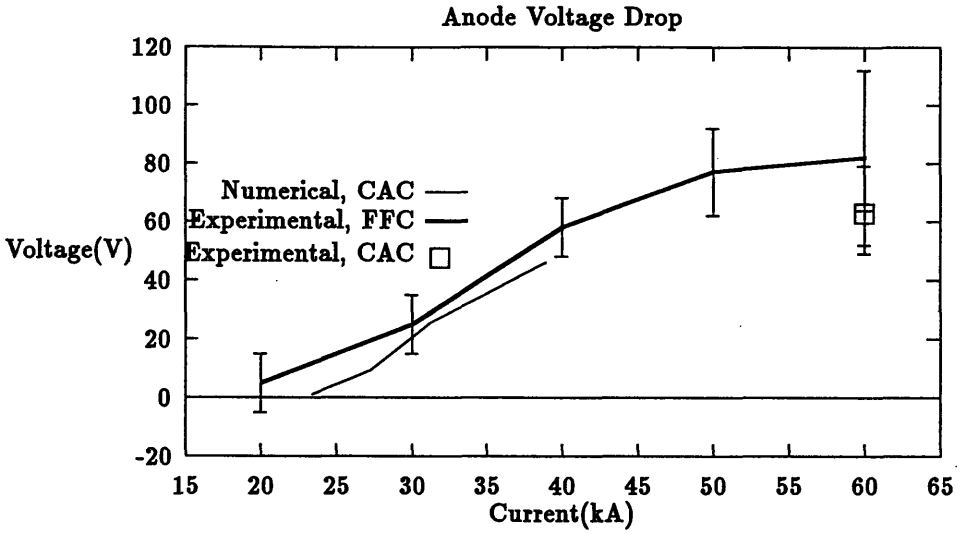

Figure 6-14: Experimental and Numerical Anode Voltage Drops

whether this trend will continue with current beyond 39 kA is unclear. The reason for the large discrepancy at low currents is also unclear. Possibly this is due to artificial ignition of the plasma in the low current numerical cases, due to the lower limit on ionization fraction. It might also be due to excessive damping in the numerical simulation at low Mach numbers.

Figure 6-16 shows the integrated potential difference between cathode and anode for each of the cases at a z location of 0.065 m. Figure 6-17 shows axial cuts of the electron number density in each of the five cases at r = 0.0704 m, 1.6 mm from the anode, while Figure 6-18 shows n_e at r = 0.0719 m, 0.1mm from the anode. The electron number density 1.6 mm from the anode does not vary strongly from case to case. The electron number density 0.1 mm from the anode does vary strongly, becoming increasingly smaller with increasing current. What causes this change in density variation from case to case over such a short distance? In part, at least, it is due to the variation in axial current. Figure 6-19 shows that the axial current 0.2mm from the anode increases as the total current increases. This does not however, explain why voltage drops are so much less significant in the lowest current case than the other four cases. One hint of an answer might come from looking at Mach number plots for the five cases. Figure 6-20 shows axial profiles of the Mach number along the centerline of the thruster. Note that all of the cases except the lowest current one go

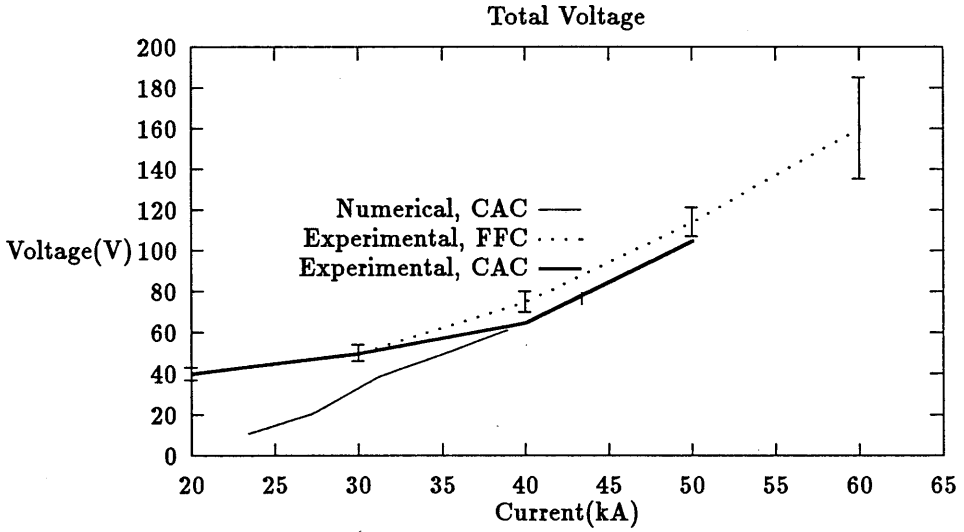

Figure 6-15: Experimental and Numerical Total Voltage Drops

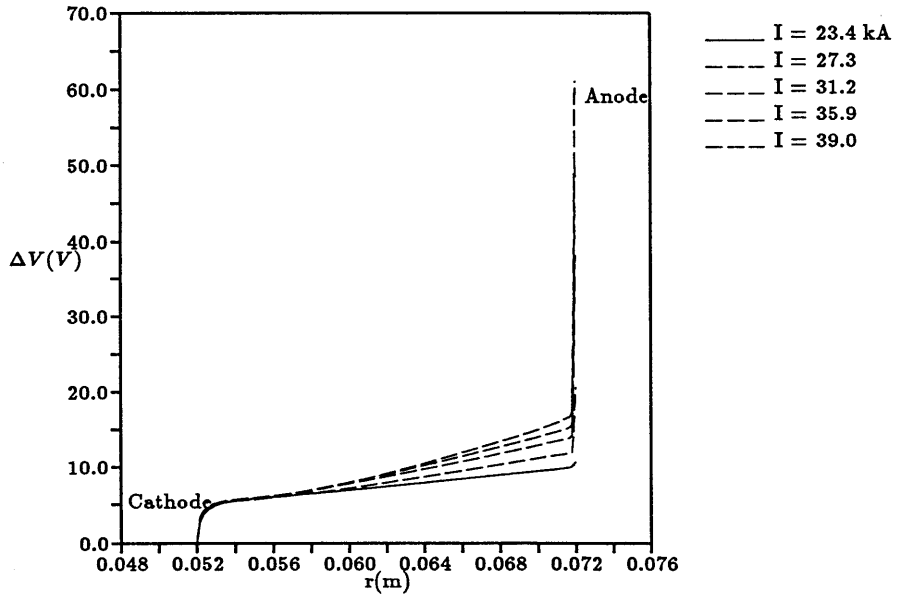

Figure 6-16: Integrated Potential Drop in Five Cases

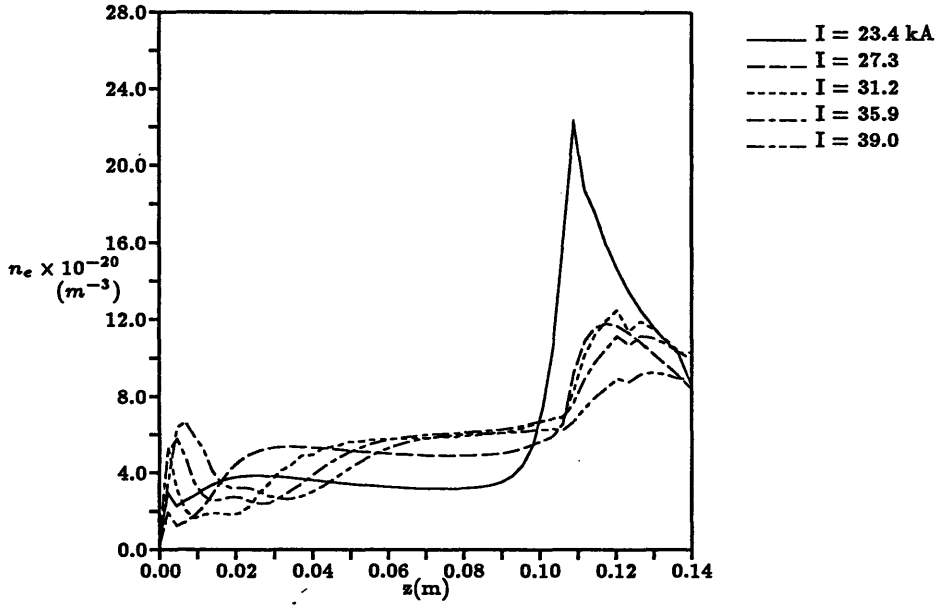

Figure 6-17: Electron Number Density at r = 0.0704 m in Five Cases

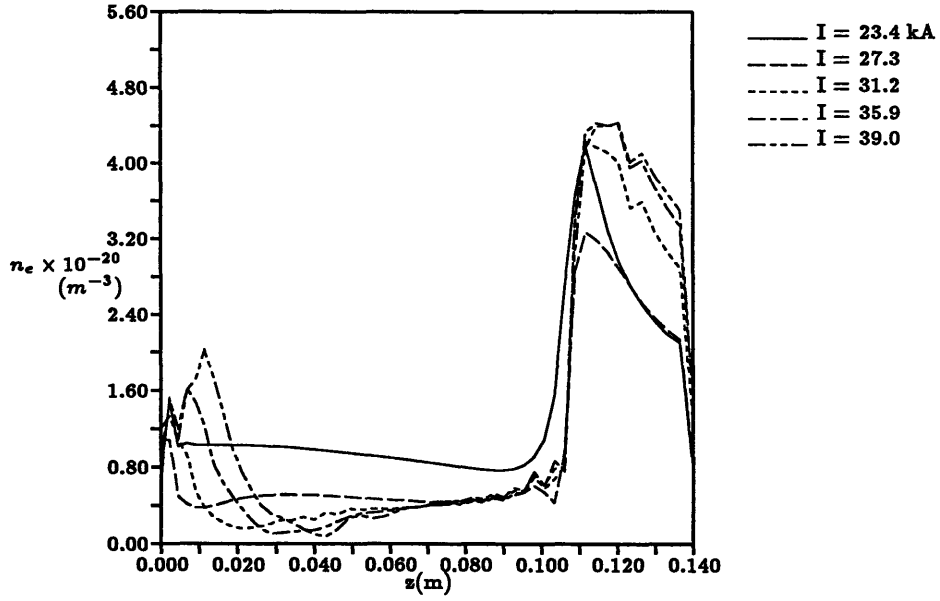

Figure 6-18: Electron Number Density at r = 0.0719 m in Five Cases

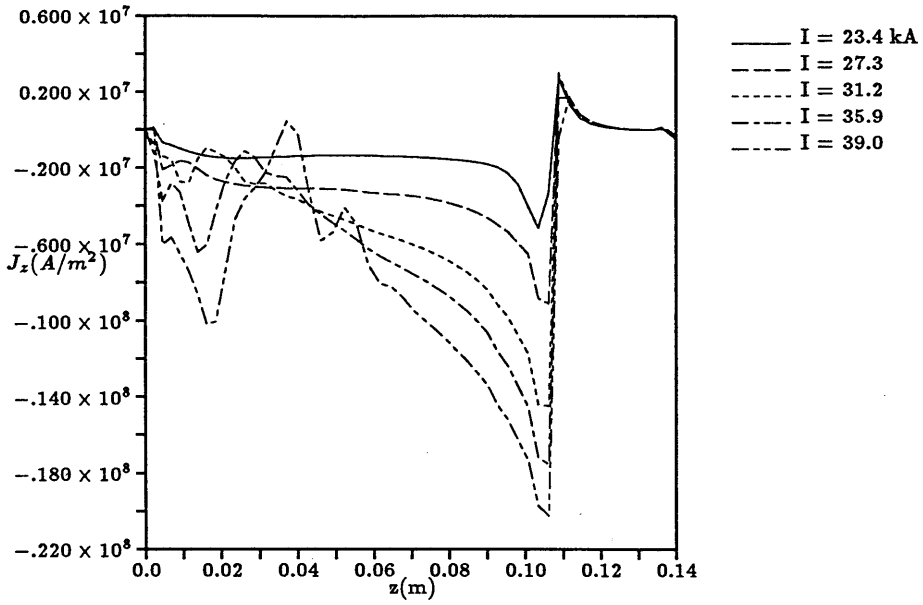

Figure 6-19: Axial Current Density at r = 0.0718 m in Five Cases

supersonic less than 3 cm from the inlet. The I = 23.4 kA case only goes supersonic at the exit current concentration. The same behaviour is noticed if one looks closer to the anode. Is it possible that the subsonic character of the 23.4 kA case allows the plasma, and perhaps the current, to distribute itself in a more even fashion? Or, is it the supersonic nature of the other cases that allows the plasma to turn away from the anode?

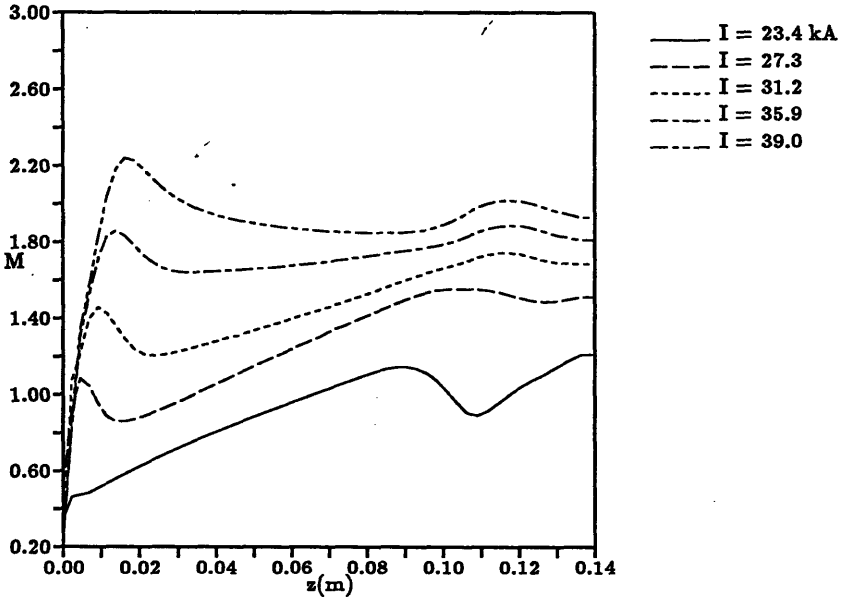

Figure 6-20: Centerline Mach Number Profiles for all Cases

Chapter 7

Other Phenomena

Although an explanation for near anode drops is the main result of this thesis, the numerical simulation predicts the state of the plasma everywhere in the thruster. These are not data which are readily available experimentally. A number of interesting things show up in these results, some of which are described briefly below.

7.1 Heavy Species Temperature

Experimental measurements have shown high heavy species temperature, with $\frac{T_g}{T_e} > 1$ and with $T_g > 80{,}000$ K [30, 36]. The mechanism by which the heavy species could be heated to such high temperatures is unclear. Choueiri [13] proposes that plasma microinstabilities are responsible. Niewood and Martinez-Sanchez [53, 55] and Miller and Martinez-Sanchez [47, 48] suggest that fluid viscosity could be responsible, particularly in long narrow channels such as that studied in this research and in the experiments of Heimerdinger. This research includes the fluid viscosity as a heating mechanism but also includes ion-neutral slip. Both are responsible for some of the ion and neutral heating seen in the results. Figure 7-1 and 7-2 show two axial profiles of the heavy species and electron temperatures in the 39.0kA case. The two profiles are at $r = 0.0525m$, 0.5mm from the cathode, and $r = 0.0704m$, 1.6mm from the anode. As can be seen, heavy species temperature can exceed electron temperature, although this happens only is some small regions. The heavy species temperature

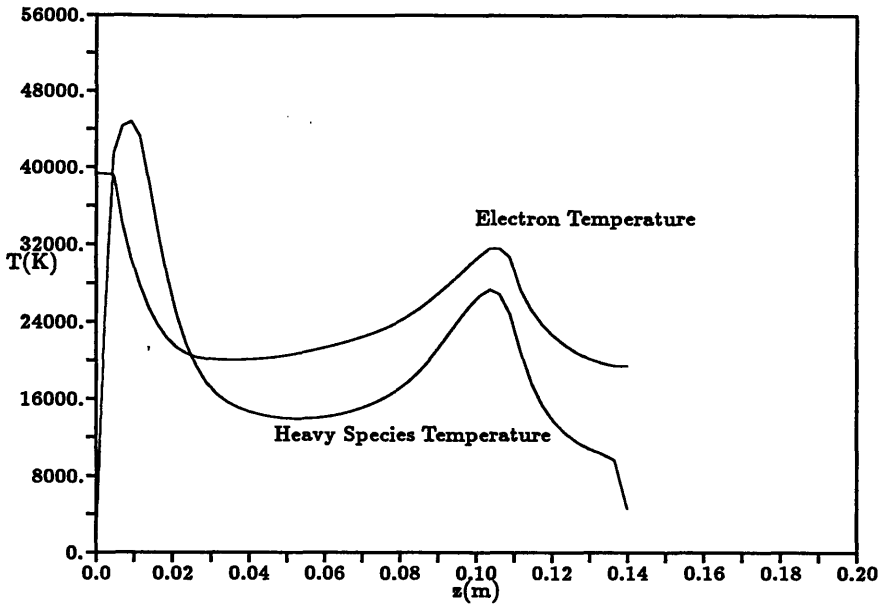

Figure 7-1: Species Temperatures 0.5 mm from the Cathode, 39.0 kA

seen at this current level reaches the upper limit of 50,000 K placed on it in a very small region near the cathode root.

The heavy species are heated primarily by the ion-neutral slip, as shown in Figures 7-3 and 7-4, plots of the magnitude of the dominant terms in the heavy species energy equation at $r = 0.0525m$, 0.5 mm from the cathode, and $r = 0.0704m$, 1.6 mm from the anode, respectively. The x-axis of both plots is the cell number (0=inlet, 50=exit). Positive values indicate that a term cools the heavy species. The inelastic slip term is heating or cooling due to inelastic collisions. Near the cathode, slip heating is dominant and balanced mostly by heavy species heat conduction. Near the anode, slip and viscous heating are more comparable and are balanced primarily by the pressure work term $P_g(\frac{\partial V_x}{\partial x} + \frac{\partial V_z}{\partial z})$. Coupling to the electrons is almost negligible near the cathode and still relatively small near the anode. The magnitude of the various terms was also examined along the centerline of the thruster. There, slip heating is primarily balanced by pressure work near the inlet, while heating by the electrons is balanced by the pressure work elsewhere. Heat conduction and viscous heating both play a small role in the equation balance ($< 10\%$ of the dominant terms).

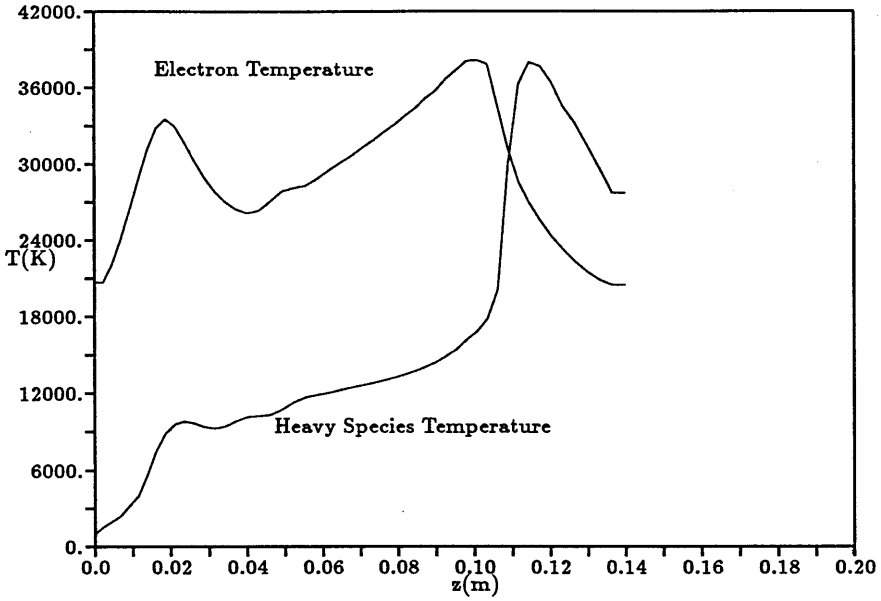

Figure 7-2: Species Temperatures 1.6 mm from the Anode, 39.0 kA

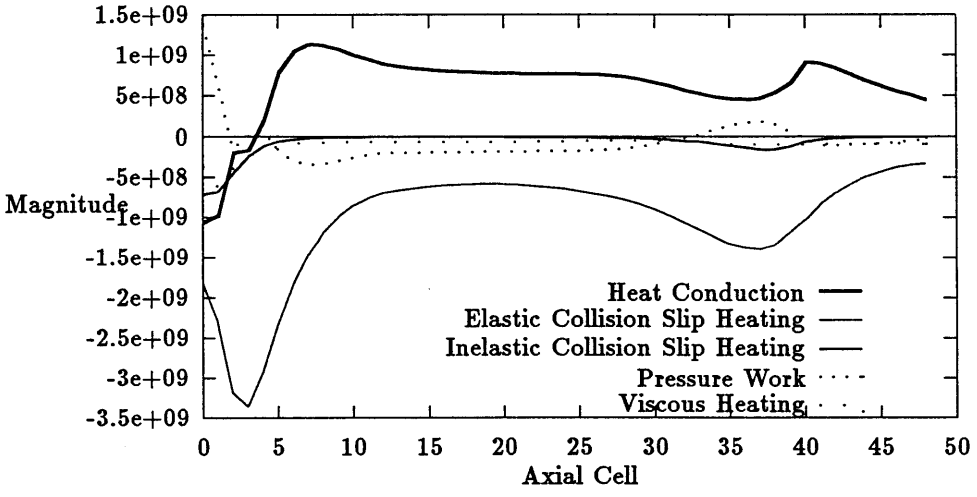

Figure 7-3: Magnitude of Terms in the Heavy Species Energy Equation 0.5 mm from the Cathode, 39.0 kA

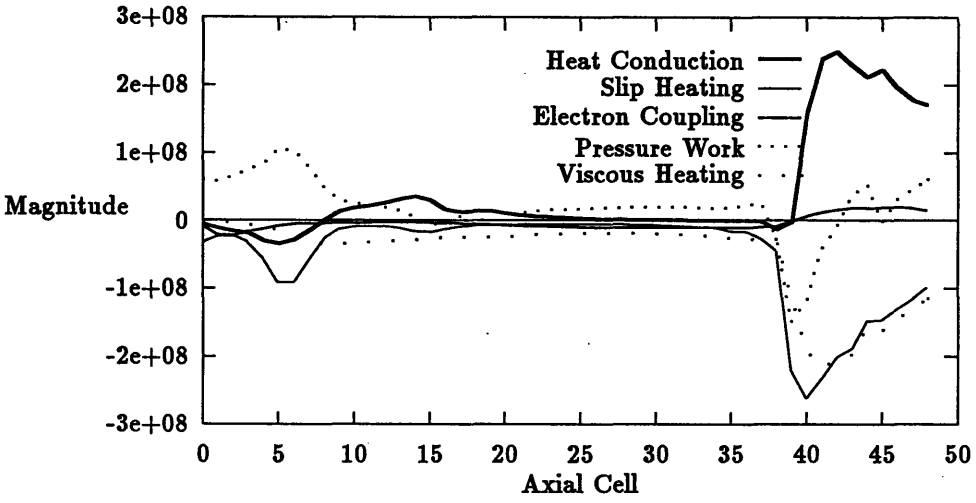

Figure 7-4: Magnitude of Terms in the Heavy Species Energy Equation 1.6 mm from the Anode, 39.0 kA

7.2 Cathode Ionization Fraction

Figure 7-5 shows constant contours of the ion (and electron) number densities in the 39.0 kA case. The letter A denotes the overall maximum of 37.4×10^{20} near the cathode root. There is also a local maximum of 24.9×10^{20} near the end of the cathode denoted by the letter B. The ionization fraction, shown in Figure 7-6 shows a similar behaviour, with a local maximum near the cathode root of 0.92 denoted by the letter A, and an overall maximum of 0.99 near the centerline just past the end of the electrodes, shown by the letter B. These distributions are reminiscent of data for the high power Princeton benchmark thruster described by Boyle [6]. He describes luminosity patterns indicating full ionization near the cathode root with much lower ionization near the anode. This high electron number density is driven by ionization, as shown in Figure 7-7. This figure plots the magnitude of the various terms in the electron continuity equation, including the numerical damping terms, along the axial line r = 0.0525 m (0.5 mm from the cathode). The lines are for ionization and recombination, "Prod", radial electron flux, "fflux", axial electron flux, "gflux—", radial damping, "rdamp", and axial damping "zdamp".

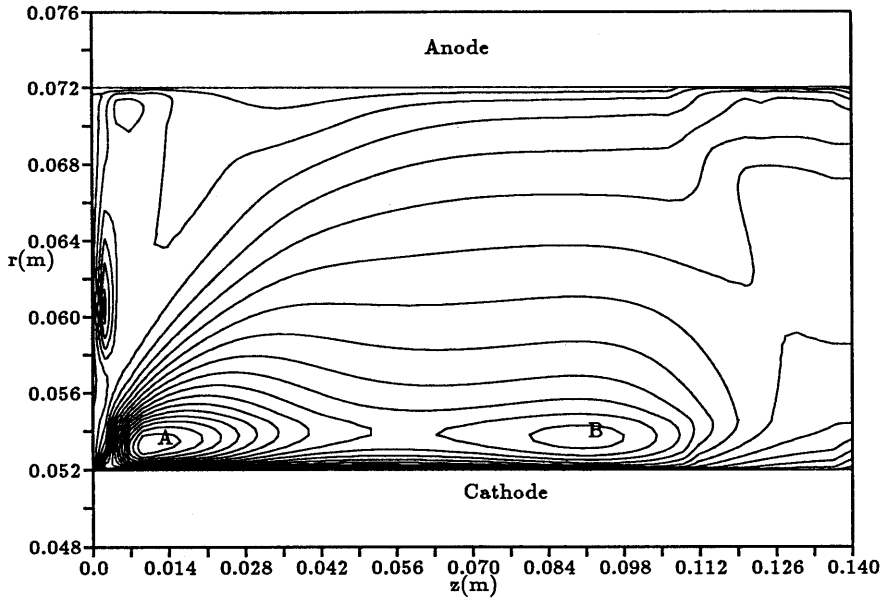

Figure 7-5: Electron Number Density Contours, 39.0 kA
A: $n_e = 3.7 \times 10^{21} m^{-3}$ B: $n_e = 2.5 \times 10^{21} m^{-3}$ Contour Spacing $= 1 \times 10^{-20} m^{-3}$

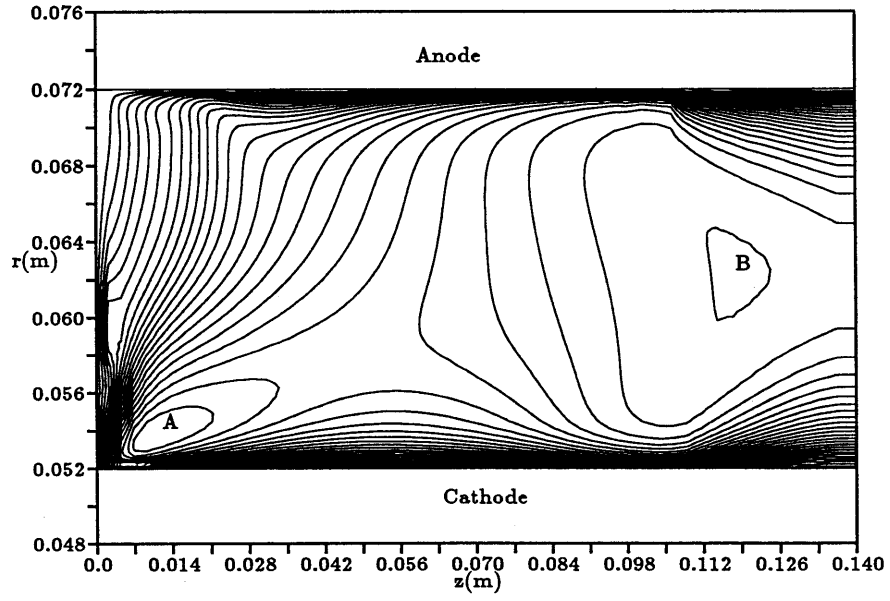

Figure 7-6: Ionization Fraction Contours, 39.0 kA
A: $\alpha = 0.92$ B: $\alpha = 0.99$ Contour spacing $= 0.04$

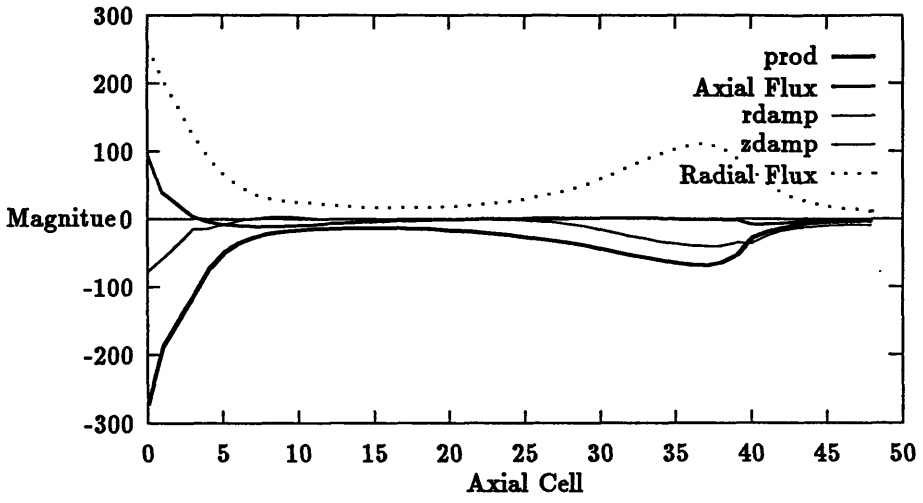

Figure 7-7: Magnitude of Terms in the Electron Continuity Equation, 0.5 mm from the Cathode

The ionization fraction right at the cathode, by contrast is quite low. This leads to a small but non-negligible cathode fall, as shown in Figure 7-8, showing the potential difference between the plasma 2.1 mm from the cathode and at the cathode. This difference of about 5.5 V is substantially smaller than that inferred by Heimerdinger in the FFC from an estimated plasma potential drop at a similar current but is within the error bars that he gives.

7.3 Boundary Layers

Work by Miller [49] showed that the viscous boundary layers in the CAC thruster grow to fill a substantial fraction of the channel. A plot of the axial velocity contours for the 39.0 kA case from this simulation, Figure 7-9, shows somewhat larger boundary layers. For this case the boundary layers seem to fill almost the whole channel. The strange pattern near the inlet is in part due to initial acceleration of the flow everywhere along a radial cut, followed by deceleration near the two electrodes. It is also due to the turning of the flow away from the anode. The asymmetry of the velocity about the centerline of the thruster is partly due to the cylindrical geometry, but is mostly due to the significantly higher density near the cathode. The maximum

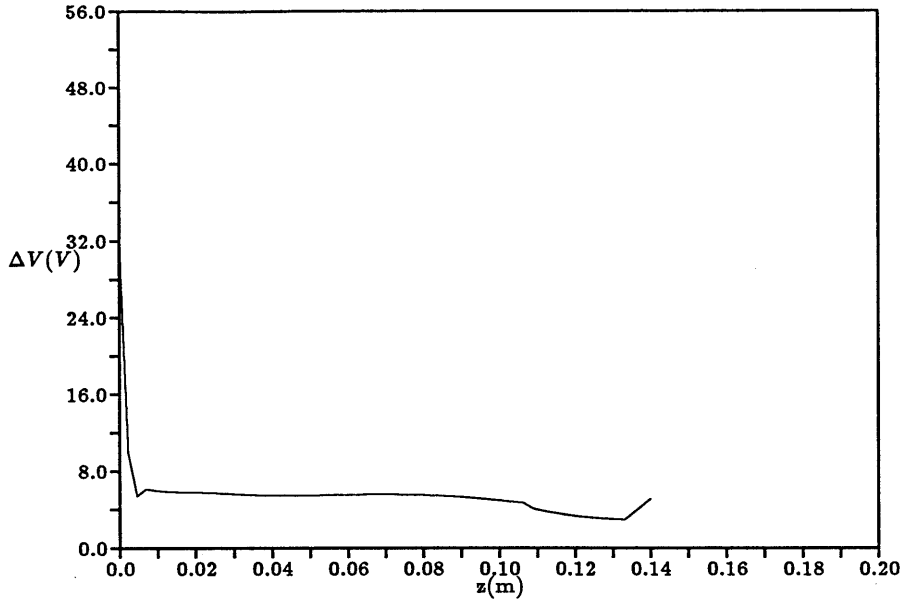

Figure 7-8: Plasma Potential 2.1 mm from the Cathode with respect to the Cathode 39.0 kA

axial velocity is reached near the end of the anode and is slightly under 9000 m/s.

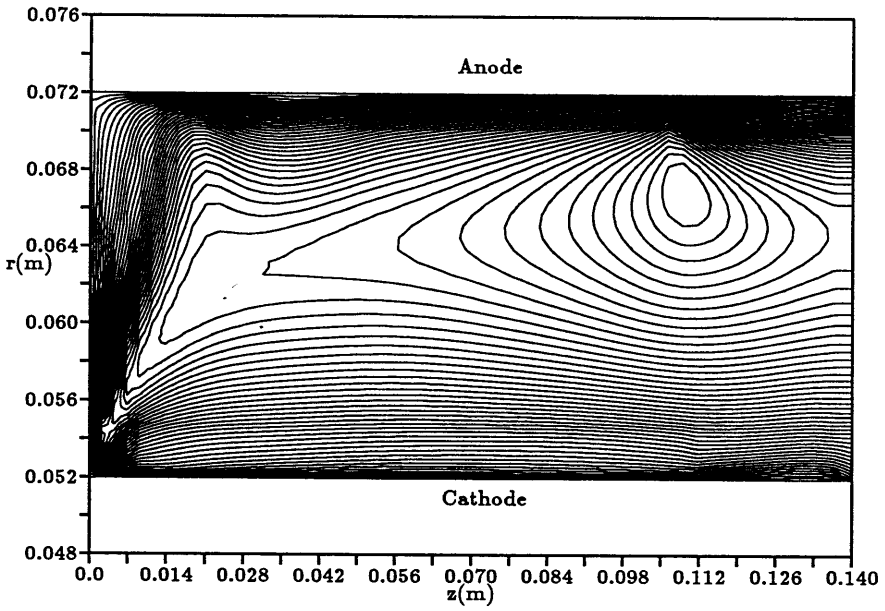

Figure 7-9: Axial Velocity Contours, 39.0 kA
Maximum = 9000 m/sec, Minimum = 0, Contour Spacing = 200 m/sec

Chapter 8

Conclusions

This chapter represents an attempt to summarize where this research stands right now. There are a number of questions which remain to be answered, many of which were touched on in previous chapters. These will be discussed in Section 8.2. There are also a number of lessons to be learned from this work, some of which are discussed in Section 8.3. Most importantly, the conclusions which can be drawn from this work are given in Section 8.1

8.1 Contributions of this Research

The contributions of this thesis to the state of the art in MPD thruster research are two-fold. This is the first two dimensional or axisymmetric simulation to model thrusters operating in the megawatt power range of interest to experimenters. Since MPD thrusters should be more efficient at higher power, these high power levels are neccessary for MPD to be a competitive choice for space propulsion. The highest current level results presented in this thesis represent a 2.4 MW power input. The highest power levels simulated in other research is 0.6 MW. Most simulations go unstable below 0.5 MW.

In addition, the governing equations used in this thesis include important physics that is not included in other models. No other models include ion-neutral slip. Few include nonequilibrium ionization and many do not include two temperatures. Be-

cause of the wealth of physics included and the high power levels simulated, the results reveal many details of the plasma flow inside the thruster that could not previously be examined either numerically, because of the limits of other models, or experimentally, because of the hostile environment inside the thruster. Information about ion-electron temperature ratios, electron density distributions, and profile of axial velocity should be invaluable to experimenters and theoriticians.

The most important contribution of this research, however, is the first theory of anode voltage drops in MPD thrusters to predict qualitatively, and perhaps quantitatively, the magnitude and behaviour of the voltage drops over a range of currents. The currents examined range from 23.4 kA where anode drops are negligible up to 39.0 kA where they dominate the overall thruster drop. The simulation correctly predicts the critical current at which the voltage drops begin to sharply increase in magnitude. It also qualitatively predicts the behaviour of the current and the potential throughout the starved region, so that it is not just macroscopic properties of the plasma flow which are being correctly modeled. Overall voltage also seems to be well predicted at the higher current values examined. The voltage drops which this research predicts are due to starvation of the near anode plasma. This starvation arises because of the Hall effect. Because anode voltage drops are the major cause of thruster inefficiency at high power levels, the results of this thesis will be useful in developing more efficient thrusters.

8.2 Questions to be Answered

This research has perhaps raised as many questions as it has answered. What causes the convergence problems seen to some extent in the CAC results and critical to results in other geometries? This is the real sticking point preventing more productive use of the simulation. Two ways to solve the problem, not just bypass it, can be envisioned. One way to deal with the convergence problem would be to write a new simulation using different methods and see if the problem still existed. This approach is discussed in the next section. The other way would be to use the simulation in its current form

and examine in great detail which variables are changing, and at which locations they change, during the oscillations. Some attempts have been made to do this but they have been inconclusive.

Given that anode voltage drops in the CAC channel seem to be due to anode starvation, how could these voltage drops be alleviated? One possibility which has been examined experimentally is to inject more of the inlet mass flow near the anode root. Kurikii et. al. [37] have had success with this technique in their KIII thruster, cutting anode drops by by 75% or more. Attempts were made to model variable injection in both the CAC and KIII geometries with the numerical code developed for this thesis. In the CAC geometry, the code did not reach a converged solution. The potential for the 31.2 kA case with most of the injection near the anode base varied from 24 to 31 V as the solution oscillated, compared to a steady state solution of 38.5 V for uniform injection. So some improvement in voltage drop was seen, but it is hard to quantify how much. For the KIII geometry, cases were run with uniform injection and injection concentrated at the cathode base. Neither injection pattern allowed for convergence. Neither solution seemed to show a substantial anode drop at any time, although there was some drop in the case with most of the injection near the cathode.

A number of other alleviation strategies can be envisioned, many of which could be modeled with a numerical code. One would be to inject mass through the anode. If a small amount of mass was injected downstream of the region where the current bends, it might be sufficient to raise the local number density and, if the flow ionizes, the local electron number density. Alternatively, shaping or displacing of the electrodes, particularly of the anode, might also reduce voltage drops by changing the current pattern.

Once alleviation strategies have been tested in the code, the next step is to try them out in experiments. That is the real goal of any voltage drop theory, to use the theory to improve thruster efficiency. Also, experiments could be done to test the theory by looking at distributions of potential, number density, and magnetic field in the near anode region.

Anode voltage drops have been observed in many other thruster designs. Does the mechanism described in this research control those drops? If so, can this code be used to predict the voltage drops in those geometries? The main barrier to answering the second of these questions is the recurring convergence problem. This problem will be dealt with in more detail later. One would expect the same mechanism to apply to voltage drops in other geometries. However, different geometries can display substantially different characteristics. More open geometries tend to have much lower density than the CAC and FFC. Transition from subsonic to supersonic flow may also take place within the last 20% of the channel length rather than near the inlet in the first 5% of the channel.

What determines the critical current at which voltage drops become significant? One suggestion for further inquiry, that it could be tied to the transition to supersonic flow, was made previously. However, if sonic transition is the dominant factor in initiating voltage drops, that would imply that accurate modeling of the shock and separation bubble near the anode root would be necessary. This is a very complex problem requiring more accurate and less dissipative numerical techniques than those used in this research. Perhaps examining other geometries would help to clarify what causes voltage drops to turn on.

What would be the effect of including plasma micro-instabilities? Plasma micro-instabilities have been the focus of much of the MPD work going on over the last few years at Princeton University. Incorporating the Princeton anomalous transport coefficients into the simulation would be relatively easy. The key questions would be how they affected stability and convergence properties.

8.3 Starting Over

The questions discussed in the previous section show that there is a great deal of future work which could be done. One way to do this work would be to continue using the simulation developed for this thesis. Another would be to create a new simulation using the lessons learned from this one.

What are those lessons? First the governing equations used in this research seem to be sufficient for describing thruster behavior and not too cumbersome. The only change that might be made is elimination of the axial slip, as the two axial velocities are pretty well coupled. This would simplify some of the analytical or semi-analytical approaches which might be taken. However, this is a minor point.

The near anode model used as a boundary condition for the electron number density and magnetic field at the anode could be improved. One way to improve it would be to assume that the radial variations of radial current and electron pressure gradient were small enough that these variables could be treated as constants. Then, the boundary conditions at each axial point would become independent of the other axial points, and a variable step size Runge-Kutta scheme could be used to solve the equations rather than the constant step size Euler scheme now used. This would probably allow removing the limiter currently used on electron number density gradient. Alternatively, the whole set of governing equations could be solved over a much finer grid than used in the interior of the simulation. This would allow inclusion of all of the axial gradients as well as better representation of the axial electric field.

One difficulty with the simulation in its current form is that the use of finite difference methods does not force conservation of total mass flow, momentum, energy, and potential. Switching to a finite volume scheme would make conserving these quantities simpler.

At the beginning of this research the electron temperature equation was solved with an explicit scheme. Switching to a semi-implicit ADI scheme allowed the electron temperature equation to be fully updated at each fluid time step. If an implicit or semi-implicit scheme could be devised for the magnetic field which would allow full updating in a reasonable time, that might improve the convergence properties of the simulation. An ADI scheme was tried with the magnetic field, but use of the anode model for the magnetic field boundary condition made the scheme unstable at time steps not much larger than the maximum explicit time step. Further work with the ADI scheme, or use of some other implicit or steady state technique, might solve this problem.

Some of the convergence problem seems to be tied to the sonic transition. In particular, convergence seems to be worse for operating parameters where the sonic transition moves from within the first the first 10% of the channel to a region between the center of the channel and the end of the electrodes. The flux vector splitting technique used in this research is known to create some problems at the sonic transition. Perhaps use of a different method for the axial fluxes would improve the convergence behavior of the simulation. Also, the Rusanov technique used for the transverse fluxes requires substantial tuning of the damping coefficients to keep the simulation stable in different operating regimes. On the other hand, the tunability of the damping coefficients sometimes allows for stable solutions where a more rigid scheme might not. However, a scheme which tuned itself might make it easier to go from geometry to geometry.

Appendix A

Equations in Transformed Coordinates

As described in Section 4.3, all of the equations are solved on a regular computational grid. The metrics described in that section are used herein to derive the transformed equations. A general equation of the form

$$\frac{\partial U}{\partial t} + \frac{\partial UV_r}{\partial r} + \frac{\partial UV_z}{\partial z} = S \tag{A.1}$$

becomes

$$\frac{\partial UG}{\partial t} + z_\xi \frac{\partial UV_r}{\partial \eta} - z_\eta \frac{\partial UV_r}{\partial \xi} + r_\eta \frac{\partial UV_z}{\partial \xi} - r_\xi \frac{\partial UV_z}{\partial \eta} = SG \tag{A.2}$$

which can be rewritten as

$$\frac{\partial UG}{\partial t} + \frac{\partial UV_r z_\xi}{\partial \eta} - UV_r z_{\xi\eta} - \frac{\partial UV_r z_\eta}{\partial \xi} + UV_r z_{\eta\xi} + \frac{\partial UV_z r_\eta}{\partial \xi} - UV_z r_{\eta\xi} - \frac{\partial UV_z r_\xi}{\partial \eta} + UV_z r_{\xi\eta} = SG \tag{A.3}$$

So,

$$\frac{\partial UG}{\partial t} + \frac{\partial U(V_r z_\xi - V_z r_\xi)}{\partial \eta} + \frac{\partial U(V_z r_\eta - V_r z_{eta})}{\partial \xi} = SG \tag{A.4}$$

or, using the contravariant velocities defined in Section 4.3,

$$\frac{\partial UG}{\partial t} + \frac{\partial U\hat{V}_r}{\partial \eta} + \frac{\partial U\hat{V}_z}{\partial \xi} = SG \tag{A.5}$$

So, the fluid equations can be written as

$$\frac{\partial n_n G}{\partial t} + \frac{\partial n_n \hat{V}_{nr}}{\partial \eta} + \frac{\partial n_n \hat{V}_{nz}}{\partial \xi} = (\dot{n}_R - \dot{n}_I - \frac{n_n V_{nr}}{r})G, \tag{A.6}$$

$$\frac{\partial n_e G}{\partial t} + \frac{\partial n_e \hat{V}_{ir}}{\partial \eta} + \frac{\partial n_e \hat{V}_{iz}}{\partial \xi} = (\dot{n}_I - \dot{n}_R - \frac{n_e V_{ir}}{r})G, \tag{A.7}$$

$$\frac{\partial \rho_n V_{nr} G}{\partial t} + \frac{\partial \rho_n V_{nr} \hat{V}_{nr} + P_n z_\xi}{\partial \eta} + \frac{\partial \rho_n V_{nr} \hat{V}_{nz} - P_n z_\eta}{\partial \xi} = (S_{nnr} + S_{nir}$$

$$+ K_{ni}(V_{ir} - V_{nr}) + K_{ne}(V_{er} - V_{nr}) - \dot{n}_{e,I} m_n V_{nr} + \dot{n}_{e,R} m_n V_{ir} - \frac{\rho_n V_{nr}^2}{r})G, \tag{A.8}$$

$$\frac{\partial \rho_n V_{nz} G}{\partial t} + \frac{\partial \rho_n V_{nz} \hat{V}_{nr} - P_n r_\xi}{\partial \eta} + \frac{\partial \rho_n V_{nz} \hat{V}_{nz} + P_n r_\eta}{\partial \xi} = (S_{nnz} + S_{niz}$$

$$+ K_{ni}(V_{iz} - V_{nz}) + K_{ne}(V_{ez} - V_{nz}) - \dot{n}_{e,I} m_n V_{nz} + \dot{n}_{e,R} m_n V_{iz} - \frac{\rho_n V_{nr} V_{nz}}{r})G, \tag{A.9}$$

$$\frac{\partial \rho_i V_{ir} G}{\partial t} + \frac{\partial \rho_i V_{ir} \hat{V}_{ir} + (P_e + P_i) z_\xi}{\partial \eta} + \frac{\partial \rho_i V_{ir} \hat{V}_{iz} - (P_e + P_i) z_\eta}{\partial \xi} = (-J_z B_{theta} + S_{inr} + S_{iir}$$

$$+ K_{in}(V_{nr} - V_{ir}) + K_{en}(V_{nr} - V_{er}) + \dot{n}_{e,I} m_i V_{nr} - \dot{n}_{e,R} m_n V_{ir} - \frac{\rho_i V_{ir}^2}{r})G, \tag{A.10}$$

$$\frac{\partial \rho_i V_{iz} G}{\partial t} + \frac{\partial \rho_i V_{iz} \hat{V}_{ir} - (P_e + P_i) r_\xi}{\partial \eta} + \frac{\partial \rho_i V_{iz} \hat{V}_{iz} + (P_e + P_i) r_\eta}{\partial \xi} = (J_r B_\theta + S_{inz} + S_{iiz}$$

$$+ K_{in}(V_{nz} - V_{iz}) + K_{en}(V_{nz} - V_{ez}) + \dot{n}_{e,I} m_n V_{nr} - \dot{n}_{e,R} m_n V_{ir} - \frac{\rho_i V_{ir} V_{iz}}{r})G, \tag{A.11}$$

and

$$\frac{\partial \frac{3}{2} P_g G}{\partial t} + \frac{\partial \frac{3}{2} P_g \hat{V}_r}{\partial \eta} + \frac{\partial \frac{3}{2} P_g \hat{V}_{iz}}{\partial \xi} + P_g(\frac{\partial \hat{V}_r}{\partial \eta} + \frac{\partial \hat{V}_z}{\partial \xi}) = \left[\frac{3k}{m_n}(K_{ie} + K_{ne})(T_e - T_g)\right.$$

$$\left. + \frac{1}{2}(K_{ni} + K_{in} + m_i(\dot{n}_{e,I} + \dot{n}_{e,R}))(U_r^2 + U_z^2) - \frac{5}{2}\frac{P_g V_r}{r} + \Phi + \kappa_i + \kappa_n\right] G. \tag{A.12}$$

The electron energy equation becomes

$$\frac{3}{2} n_e k \left[\frac{\partial T_e G}{\partial t} + \hat{V}_{er}\frac{\partial T_e}{\partial \eta} + \hat{V}_{ez}\frac{\partial T_e}{\partial \xi} + T_e(\frac{\partial \hat{V}_{er}}{\partial \eta} + \frac{\partial \hat{V}_{ez}}{\partial z})\right] = \left[(K_{ei} + K_{en})\left(\frac{3k}{m_n}(T_g - T_e)\right)\right.$$

$$+\frac{J^2}{\sigma}+K_{en}(U^2-2\frac{\mathbf{J}\cdot\mathbf{U}}{\mathbf{en_e}})-\dot{n}_e(E_i-\frac{3}{2}kT_e)-\frac{P_eV_{er}}{r}+\kappa_e\Bigg] \tag{A.13}$$

The magnetic field equation becomes

$$\frac{\partial B_\theta G}{\partial t}-\frac{\partial(E_zz_\xi-E_rr_\xi)}{\partial\eta}+\frac{\partial(E_rr_\eta-E_rz_\eta)}{\partial\xi}=0. \tag{A.14}$$

The viscous stress source terms are given in an axisymmetric geometry by

$$S_{stz}=v_{st}\left[\frac{4}{3}\frac{\partial^2V_{tz}}{\partial z^2}+\frac{\partial^2V_{tz}}{\partial r^2}+\frac{1}{3}\frac{\partial^2V_{tr}}{\partial r\partial z}\right]+\frac{\partial V_{tr}}{\partial z}(\frac{1}{3}\frac{v_{st}}{r}+\frac{\partial v_{st}}{\partial r})-\frac{2}{3}\frac{\partial V_{tr}}{\partial r}\frac{\partial v_{st}}{\partial z}$$

$$-\frac{2}{3}\frac{V_{tr}}{r}\frac{\partial v_{st}}{\partial z}+\frac{\partial V_{tz}}{\partial r}(\frac{\partial v_{st}}{\partial r}+\frac{v_{st}}{r})+\frac{4}{3}\frac{\partial v_{st}}{\partial z}\frac{\partial V_{tz}}{\partial z} \tag{A.15}$$

and

$$S_{str}=v_{si}\left[\frac{4}{3}\frac{\partial^2V_{tr}}{\partial r^2}+\frac{\partial^2V_{tr}}{\partial z^2}+\frac{1}{3}\frac{\partial^2V_{tz}}{\partial r\partial z}\right]+\frac{4}{3}\frac{\partial V_{tr}}{\partial r}(\frac{v_{st}}{r}+\frac{\partial v_{st}}{\partial r})+\frac{\partial V_{tr}}{\partial z}\frac{\partial v_{st}}{\partial z}$$

$$+\frac{\partial V_{tz}}{\partial r}\frac{\partial v_{st}}{\partial z}-\frac{2}{3}\frac{\partial V_{tz}}{\partial z}\frac{\partial v_{st}}{\partial r}-\frac{2}{3}\frac{V_{tr}}{r}(\frac{\partial v_{st}}{\partial r}+2\frac{v_{st}}{r}) \tag{A.16}$$

as shown in Section 3.5.1. In transformed coordinates these expressions are significantly more complicated. Dropping the fluid subscripts and using the expressions of Section 4.3

$$S_z=v\left[\frac{4}{3}\left(\frac{1}{G^2}\left[r_\eta^2\frac{\partial^2V_z}{\partial\xi^2}-2r_\xi r_\eta\frac{\partial^2V_z}{\partial\xi\partial\eta}+r_\xi^2\frac{\partial^2V_z}{\partial\eta^2}\right]+\eta_{zz}\frac{\partial V_z}{\partial\eta}+\xi_{zz}\frac{\partial V_z}{\partial\xi}\right)\right.$$

$$+\frac{1}{G^2}\left[z_\xi^2\frac{\partial^2V_z}{\partial\eta^2}-2z_\xi z_\eta\frac{\partial^2V_z}{\partial\xi\partial\eta}+z_\eta^2\frac{\partial^2V_z}{\partial\xi^2}\right]+\eta_{rr}\frac{\partial V_z}{\partial\eta}+\xi_{rr}\frac{\partial V_z}{\partial\xi}$$

$$\left.+\frac{1}{3}\left(\frac{1}{G^2}\left[G\frac{\partial^2V_r}{\partial\eta\partial\xi}-r_\xi z_\xi\frac{\partial^2V_r}{\partial\eta^2}-z_\eta r_\eta\frac{\partial^2V_r}{\partial\xi^2}\right]+V1\frac{\partial V_r}{\partial\xi}+V2\frac{\partial V_r}{\partial\eta}\right)\right]$$

$$+\frac{1}{G^2}\left[\left(r_\eta\frac{\partial V_r}{\partial\xi}-r_\xi\frac{\partial V_r}{\partial\eta}\right)\left(\frac{vG}{3r}+z_\xi\frac{\partial v}{\partial\eta}-z_\eta\frac{\partial v}{\partial\xi}\right)-\frac{2}{3}\left(z_\xi\frac{\partial V_r}{\partial\eta}-z_\eta\frac{\partial V_r}{\partial\xi}\right)\left(r_\eta\frac{\partial v}{\partial\xi}-r_\xi\frac{\partial v}{\partial\eta}\right)\right.$$

$$\left.-\frac{2GV_r}{3r}\left(r_\eta\frac{\partial v}{\partial\xi}-r_\xi\frac{\partial v}{\partial\eta}\right)+\left(z_\xi\frac{\partial V_z}{\partial\eta}-z_\eta\frac{\partial V_z}{\partial\xi}\right)\left(z_\xi\frac{\partial v}{\partial\eta}-z_\eta\frac{\partial v}{\partial\xi}+\frac{vG}{r}\right)\right.$$

$$+\frac{4}{3}\left(r_\eta\frac{\partial V_z}{\partial\xi}-r_\xi\frac{\partial V_z}{\partial\eta}\right)\left(r_\eta\frac{\partial v}{\partial\xi}-r_\xi\frac{\partial v}{\partial\eta}\right)\Bigg] \tag{A.17}$$

Grouping the various terms by the velocity derivatives,

$$S_z=\frac{1}{G^2}\Bigg[v\Bigg[\left(\frac{4}{3}r_\eta^2+z_\eta^2\right)\frac{\partial^2V_z}{\partial\xi^2}+\left(\frac{4}{3}r_\xi^2+z_\xi^2\right)\frac{\partial^2V_r}{\partial\eta^2}-2\left(\frac{4}{3}r_\eta r_\xi+z_\eta z_\xi\right)\frac{\partial^2V_z}{\partial\xi\partial\eta}$$

$$+\frac{G}{3}\frac{\partial^2V_r}{\partial\eta\partial\xi}-\frac{r_\xi z_\xi}{3}\frac{\partial^2V_r}{\partial\eta^2}-\frac{r_\eta z_\eta}{3}\frac{\partial^2V_r}{\partial\xi^2}\Bigg]-\frac{2V_rG}{3r}\left(r_\eta\frac{\partial v}{\partial\xi}-r_\xi\frac{\partial v}{\partial\eta}\right)$$

$$+\frac{\partial V_z}{\partial\eta}\left[Gv\left(\frac{4}{3}\eta_{zz}G+\eta_{rr}G+\frac{z_\xi}{r}\right)+\frac{\partial v}{\partial\eta}\left(\frac{4}{3}r_\xi^2+z_\xi^2\right)-\frac{\partial v}{\partial\xi}\left(\frac{4}{3}r_\eta r_\xi+z_\eta z_\xi\right)\right]$$

$$+\frac{\partial V_z}{\partial\xi}\left[Gv\left(\frac{4}{3}\xi_{zz}G+\xi_{rr}G-\frac{z_\eta}{r}\right)+\frac{\partial v}{\partial\xi}\left(\frac{4}{3}r_\eta^2+z_\eta^2\right)-\frac{\partial v}{\partial\eta}\left(\frac{4}{3}r_\eta r_\xi+z_\eta z_\xi\right)\right]$$

$$+\frac{\partial V_r}{\partial\xi}\left[vG\left(\frac{V1G}{3}+\frac{r_\eta}{3r}\right)+\frac{\partial v}{\partial\eta}\left(r_\eta z_\xi-\frac{2}{3}r_\xi z_\eta\right)+\frac{\partial v}{\partial\xi}\left(\frac{2}{3}z_\eta r_\eta-r_\eta z_\eta\right)\right]$$

$$+\frac{\partial V_r}{\partial\eta}\left[vG\left(\frac{V2G}{3}-\frac{r_\xi}{3r}\right)+\frac{\partial v}{\partial\xi}\left(r_\xi z_\eta-\frac{2}{3}z_\xi r_\eta\right)+\frac{\partial v}{\partial\eta}\left(\frac{2}{3}z_\xi r_\xi-r_\xi z_\xi\right)\right]\Bigg] \tag{A.18}$$

The terms which depend only on the grid coordinates do not change during the simulation and so they can be computed once and then stored. Combining them into coefficients the expression can be simplified somewhat as

$$S_z=\frac{1}{G^2}\Bigg[v\left(S_{z1}\frac{\partial^2V_z}{\partial\xi^2}+S_{z2}\frac{\partial V_z}{\partial\eta^2}-2S_{z3}\frac{\partial^2V_z}{\partial\xi\partial\eta}-S_{z10}\frac{\partial^2V_r}{\partial\eta^2}-S_{z11}\frac{\partial^2V_r}{\partial\xi^2}+\frac{G}{3}\frac{\partial^2V_r}{\partial\eta\partial\xi}\right)$$

$$+\frac{\partial V_z}{\partial\eta}\left(vS_{z4}+\frac{\partial v}{\partial\eta}S_{z2}-\frac{\partial v}{\partial\xi}S_{z3}\right)+\frac{\partial V_z}{\partial\xi}\left(vS_{z5}-\frac{\partial v}{\partial\eta}S_{z3}+\frac{\partial v}{\partial\xi}S_{z1}\right)+\frac{\partial V_r}{\partial\eta}\left(vS_{z8}+\frac{\partial v}{\partial\xi}S_{z9}-\frac{\partial v}{\partial\eta}S_{z10}\right)$$

$$+\frac{\partial V_r}{\partial\xi}\left(vS_{z6}+\frac{\partial v}{\partial\eta}S_{z7}-\frac{\partial v}{\partial\xi}S_{z11}\right)-\frac{2GV_r}{3r}\left(r_\eta\frac{\partial v}{\partial\xi}-r_\xi\frac{\partial v}{\partial\eta}\right)\Bigg] \tag{A.19}$$

The $S_{z1,2,...}$ terms are functions of the grid coordinates and are given by

$$S_{z1}=\frac{4}{3}r_\eta^2+z_\eta^2$$

$$S_{z2}=\frac{4}{3}r_\xi^2+z_\xi^2$$

$$S_{z3} = \frac{4}{3} r_\xi r_\eta + z_\xi z_\eta$$

$$S_{z4} = \frac{4}{3} \eta_{zz} G^2 + \eta_{rr} G^2 + \frac{z_\xi G}{r}$$

$$S_{z5} = \frac{4}{3} \xi_{zz} G^2 + \xi_{rr} G^2 - \frac{z_\eta G}{r}$$

$$S_{z6} = \frac{V1 G^2}{3} + \frac{r_\eta G}{3r}$$

$$S_{z7} = z_\xi r_\eta - \frac{2}{3} r_\xi z_\eta$$

$$S_{z8} = \frac{V2 G^2}{3} - \frac{r_\xi G}{3r}$$

$$S_{z9} = z_\eta r_\xi - \frac{2}{3} r_\eta z_\xi$$

$$S_{z10} = \frac{r_\xi z_\xi}{3}$$

$$S_{z11} = \frac{r_\eta z_\eta}{3}$$

The same procedure must be performed for the source term in the radial momentum equation.

$$S_r = v \left[\frac{4}{3} \left(\frac{1}{G^2} \left(z_\xi^2 \frac{\partial^2 V_r}{\partial \eta^2} - 2 z_\xi z_\eta \frac{\partial^2 V_r}{\partial \xi \partial \eta} + z_\eta^2 \frac{\partial^2 V_r}{\partial \xi^2} \right) + \eta_{rr} \frac{\partial V_r}{\partial \eta} + \xi_{rr} \frac{\partial V_r}{\partial \xi} \right) \right.$$

$$+ \frac{1}{G^2} \left[r_\eta^2 \frac{\partial^2 V_r}{\partial \xi^2} - 2 r_\xi r_\eta \frac{\partial^2 V_r}{\partial \xi \partial \eta} + r_\xi^2 \frac{\partial^2 V_r}{\partial \eta^2} \right] + \eta_{zz} \frac{\partial V_r}{\partial \eta} + \xi_{zz} \frac{\partial V_r}{\partial \xi} + \frac{1}{3} \left[\frac{1}{G^2} \left[G \frac{\partial^2 V_z}{\partial \eta \partial \xi} - r_\xi z_\xi \frac{\partial^2 V_z}{\partial \eta^2} - z_\eta r_\eta \frac{\partial^2 V_z}{\partial \xi^2} \right] \right.$$

$$\left. + V1 \frac{\partial V_z}{\partial \xi} + V2 \frac{\partial V_z}{\partial \eta} \right] + \frac{4}{3} \frac{1}{G^2} \left(z_\xi \frac{\partial V_r}{\partial \eta} - z_\eta \frac{\partial V_r}{\partial \xi} \right) \left(\frac{vG}{r} + z_\xi \frac{\partial v}{\partial \eta} - z_\eta \frac{\partial v}{\partial \xi} \right)$$

$$+ \frac{1}{G^2} \left[\left(r_\eta \frac{\partial V_r}{\partial \xi} - r_\xi \frac{\partial V_r}{\partial \eta} \right) \left(r_\eta \frac{\partial v}{\partial \xi} - r_\xi \frac{\partial v}{\partial \eta} \right) + \left(z_\xi \frac{\partial V_z}{\partial \eta} - z_\eta \frac{\partial V_z}{\partial \xi} \right) \left(r_\eta \frac{\partial v}{\partial \xi} - r_\xi \frac{\partial v}{\partial \eta} \right) \right.$$

$$\left. \left. - \frac{2}{3} \left(r_\eta \frac{\partial V_z}{\partial \xi} - r_\xi \frac{\partial V_z}{\partial \eta} \right) \left(z_\xi \frac{\partial v}{\partial \eta} - z_\eta \frac{\partial v}{\partial \xi} \right) - \frac{2GV_r}{3r} \left(z_\xi \frac{\partial v}{\partial \eta} - z_\eta \frac{\partial v}{\partial \xi} + 2 \frac{vG}{r} \right) \right] \right. \quad \text{(A.20)}$$

Rearranging,

$$S_r = \frac{v}{G^2} \left[\left(\frac{4}{3} z_\xi^2 + r_\xi^2 \right) \frac{\partial^2 V_r}{\partial \eta^2} + \left(\frac{4}{3} z_\eta^2 + r_\eta^2 \right) \frac{\partial^2 V_r}{\partial \xi^2} - 2 \left(\frac{4}{3} z_\xi z_\eta + r_\eta r_\xi \right) \frac{\partial^2 V_r}{\partial \eta \partial \xi} \right.$$

$$+\frac{1}{3}\left(G\frac{\partial^2 V_z}{\partial\xi\partial\eta}-r_\xi z_\xi\frac{\partial^2 V_z}{\partial\eta^2}-z_\eta r_\eta\frac{\partial^2 V_z}{\partial\xi^2}\right)\Bigg]$$

$$+\frac{\partial V_r}{\partial\eta}\left[v(\frac{4}{3}\eta_{rr}+\eta_{zz}+\frac{4z_\xi}{3rG})+\frac{1}{G^2}\left(\frac{\partial v}{\partial\eta}(\frac{4}{3}z_\xi^2+r_\xi^2)-\frac{\partial v}{\partial\xi}(\frac{4}{3}z_\xi z_\eta+r_\xi r_\eta)\right)\right]$$

$$+\frac{\partial V_r}{\partial\xi}\left[v(\frac{4}{3}\xi_{rr}+\xi_{zz}-\frac{4z_\eta}{3rG})-\frac{1}{G^2}\left(\frac{\partial v}{\partial\eta}(\frac{4}{3}z_\xi z_\eta+r_\xi r_\eta)+\frac{\partial v}{\partial\xi}(\frac{4}{3}z_\eta^2+r_\eta^2)\right)\right]$$

$$+\frac{\partial V_z}{\partial\eta}\left[\frac{1}{3}vV2+\frac{1}{G^2}\left(\frac{\partial v}{\partial\xi}(z_\xi r_\eta-\frac{2}{3}r_\xi z_\eta)+\frac{\partial v}{\partial\eta}(\frac{2}{3}r_\xi z_\xi-r_\xi z_\xi)\right)\right]$$

$$+\frac{\partial V_z}{\partial\xi}\left[\frac{1}{3}vV1+\frac{1}{G^2}\left(\frac{\partial v}{\partial\eta}(r_\xi z_\eta-\frac{2}{3}r_\eta z_\xi)+\frac{\partial v}{\partial\xi}(\frac{2}{3}r_\eta z_\eta-r_\eta z_\eta)\right)\right]$$

$$-\frac{2V_r}{3r}\left[\frac{2v}{r}+\frac{1}{G}(z_\xi\frac{\partial v}{\partial\eta}-z_\eta\frac{\partial v}{\partial\xi})\right] \qquad \text{(A.21)}$$

Further simplification yields

$$S_r=\frac{1}{G^2}\left[v\left(S_{r1}\frac{\partial^2 V_r}{\partial\eta^2}+S_{r2}\frac{\partial^2 V_r}{\partial\xi^2}-2S_{r3}\frac{\partial^2 V_z}{\partial\xi\partial\eta}-S_{z10}\frac{\partial^2 V_z}{\partial\eta^2}-S_{z11}\frac{\partial^2 V_z}{\partial\xi^2}\right)+\frac{G}{3}\frac{\partial^2 V_z}{\partial\eta\partial\xi}\right.$$

$$+\frac{\partial V_r}{\partial\eta}\left(vS_{r4}+\frac{\partial v}{\partial\eta}S_{r1}-\frac{\partial v}{\partial\xi}S_{r3}\right)+\frac{\partial V_r}{\partial\xi}\left(vS_{r5}-\frac{\partial v}{\partial\eta}S_{r3}+\frac{\partial v}{\partial\xi}S_{r2}\right)+\frac{\partial V_z}{\partial\eta}\left(vS_{r6}+\frac{\partial v}{\partial\xi}S_{z7}-\frac{\partial v}{\partial\eta}S_{z10}\right)$$

$$\left.+\frac{\partial V_z}{\partial\xi}\left(vS_{r8}+\frac{\partial v}{\partial\eta}S_{z9}-\frac{\partial v}{\partial\xi}S_{z11}\right)-V_r\left(\frac{4vG^2}{3r^2}+\frac{2G}{3r}\left(z_\xi\frac{\partial v}{\partial\eta}-z_\eta\frac{\partial v}{\partial\xi}\right)\right)\right] \qquad \text{(A.22)}$$

The $S_{r1,2,...}$ terms are functions of the grid coordinates and are given by

$$S_{r1}=\frac{4}{3}z_\xi^2+r_\xi^2$$

$$S_{r2}=\frac{4}{3}z_\eta^2+r_\eta^2$$

$$S_{r3}=\frac{4}{3}z_\xi z_\eta+r_\xi r_\eta$$

$$S_{r4}=\frac{4}{3}\eta_{rr}G^2+\eta_{zz}G^2+\frac{4z_\xi G}{3r}$$

$$S_{r5}=\frac{4}{3}\xi_{rr}G^2+\xi_{zz}G^2-\frac{4z_\eta G}{3r}$$

$$S_{r6}=\frac{V2G^2}{3}$$

$$S_{r8} = \frac{V1G^2}{3}$$

For the viscous terms in the heavy species energy equation each of the first order derivatives is computed in physical space using the formulas of Section 4.3.

Appendix B

One Fluid Characteristic Theory

One of the more common techniques for deriving boundary conditions for CFD solutions to hyperbolic systems is the use of characteristic theory. The characteristics show which direction information is propagating in and what information is being propagated in that direction. Unfortunately, the system of equations being solved for this research is not hyperbolic. Also, even neglecting the magnetic field equation and the non-hyperbolic terms of the other equations, the system of equations is too complex to readily find its eigenvalues and eigenvectors, a necessity for applying characteristic techniques. Therefore, each fluid is treated somewhat independently to derive the boundary conditions described below.

B.1 Side Walls

K. W. Thompson [69] describes a generalized formulation for deriving characteristic based boundary conditions for hyperbolic systems. This formalism was used to derive the boundary condition for electron number density at the insulating side wall. The equations used to find the boundary condition are given by

$$\frac{\partial \mathbf{U}}{\partial t} + \mathbf{W}\frac{\partial U}{\partial r} = -\mathbf{C} \tag{B.1}$$

where

$$\mathbf{U} = \left\{ \begin{array}{c} \rho_i \\ V_{ir} \\ V_{iz} \end{array} \right\}$$

and

$$\mathsf{W} = \left\{ \begin{array}{ccc} V_{ir} & \rho_i & 0 \\ k(T_e + T_g) & V_{ir} & 0 \\ 0 & 0 & V_{ir} \end{array} \right\}$$

The eigenvalues of W are given by $\Lambda = V_{ir}, V_{ir} + a_i, V_{ir} - a_i$, where $a_i = \sqrt{\frac{k}{m_i}(T_e + T_g)}$. The left eigenvectors are given by $l_1 = [0, 0, 1], l_2 = [\frac{a_i}{\rho_i}, 1, 0]$, and $l_3 = [-\frac{a_i}{\rho_i}, 1, 0]$. The right eigenvectors are given by $r_3^T = [-\frac{\rho_i}{a_i}, 1, 0], r_2^T = [0, 0, 1]$, and $r_3^T = [\frac{\rho_i}{a_i}, 1, 0]$. Thompson's L quantities are then given by

$$L_1 = [\frac{a_i^2}{\rho_i} - \frac{V_{ir} a_i}{\rho_i}]\frac{\partial \rho_i}{\partial r} + (V_{ir} - a_i)\frac{\partial V_{ir}}{\partial r},$$

$$L_2 = V_{ir}\frac{\partial V_{iz}}{\partial r},$$

and

$$L_3 = [\frac{a_i^2}{\rho_i} + \frac{V_{ir} a_i}{\rho_i}]\frac{\partial \rho_i}{\partial r} + (V_{ir} + a_i)\frac{\partial V_{ir}}{\partial r},$$

and, at the boundary,

$$\frac{\partial \rho_i}{\partial t} - \frac{\rho_i}{a_i} L_1 + \frac{\rho_i}{a_i} L_3 + C_1 = 0 \tag{B.2}$$

Since V_{ir} and $V_{ir} + a_i$ are both positive, L_2 and L_3 are both determined by interior differencing. From the boundary condition $V_{ir} = V_{bohm} = a_i$, $L_1 = 0$. So,

$$\frac{\partial \rho_i}{\partial t} = -C_1 - 2(V_{ir}\frac{\partial \rho_i}{\partial r} + \rho_i \frac{\partial V_{ir}}{\partial r}) \tag{B.3}$$

where the gradients are determined by one sided differences into the interior of the computational grid.

B.2 Exit Boundary Conditions

To find the exit boundary conditions, the methods described by P. A. Thompson [70] were used. The one fluid equations used at the exit are

$$\frac{\partial \mathbf{U}}{\partial t} + \mathsf{W}\frac{\partial U}{\partial z} = 0 \tag{B.4}$$

where

$$\mathbf{U} = \begin{Bmatrix} \rho_s \\ V_{sz} \\ T_s \end{Bmatrix}$$

and

$$\mathsf{W} = \begin{Bmatrix} V_{sz} & \rho_s & 0 \\ \frac{kT_s}{m_i\rho_s} & V_{sz} & \frac{k}{m_i} \\ 0 & \frac{2}{3}T_s & V_{sz} \end{Bmatrix}$$

where s is an index for the different species. The eigenvalues of W give the characteristic directions at the exit. They are $\Lambda = V_z, V_z + \sqrt{\frac{5}{3}\frac{kT_s}{m_s}}, V_z - \sqrt{\frac{5}{3}\frac{kT_s}{m_s}},$. The characteristic equations are found by taking the determinant of a matrix derived from combining two of the rows of W with a row of the derivatives along the characteristic directions of the three variables, and

$$\mathsf{X} = \begin{Bmatrix} \Lambda - V_z & -\frac{kT}{m_i\rho} & 0 \\ -\rho & \Lambda - V_z & -\frac{2}{3}T \\ \frac{d\rho}{dx} & \frac{dV_z}{dx} & \frac{dT}{dx} \end{Bmatrix}$$

where x is a length along the characteristic direction. So, the characteristic equation is given by

$$(\Lambda - V_z)\left[(\Lambda - V_z)\frac{dT}{dx} + \frac{2}{3}T\frac{dV_z}{dx}\right] = \frac{kT}{m_i\rho}(-\rho\frac{dT}{dx} + \frac{2}{3}T\frac{d\rho}{dx}). \tag{B.5}$$

Along the direction $\Lambda = V_z$ (from inside),

$$\frac{1}{\rho}\frac{d\rho}{dx} = \frac{3}{2T}\frac{dT}{dx} \tag{B.6}$$

and along the direction $\Lambda = V_z + a$ (from inside),

$$\frac{dV_z}{dx} = \frac{-k}{am_i}\left[\frac{T}{\rho}\frac{d\rho}{dx} + \frac{dT}{dx}\right]. \tag{B.7}$$

So, the information which propagates from inside is

$$\rho(i, NZ) = \rho(i, NZ-1)\left(\frac{T(i, NZ)}{T(i, NZ-1)}\right)^{\frac{3}{2}} \tag{B.8}$$

and

$$V_z(i, NZ) = V_z(i, NZ-1) - \frac{5}{2}\frac{k}{m_i a}(T(i, NZ) - T(i, NZ-1)) \tag{B.9}$$

Appendix C

Damping Terms

The terms used to damp all of the radial and some of the axial fluxes are quite complex. They are also one of the important factors in keeping the simulation accurate but stable and allowing it to reach a convergent solution.

C.1 Magnitude

Manipulating the magnitude of the damping terms was of great importance in obtaining a stable and convergent solution. Unfortunately, damping also leads to errors in the solution. This errors were minimized by attempting to keep the damping terms as small as possible. The damping terms were also modified to limit their cumulative effect on the solution. Since the damping is conservative, the contribution of the radial damping to integral quantities such as massflow and momentum depends on the damping fluxes at the electrodes. As shown in the following section,the damping terms in the ion and neutral density equations are set to zero at both electrodes and the damping term in the ion radial momentum equation is set to zero at the anode. The magnitude of the radial damping in the ion density equation at a given radial location was shown in Figure 7-7. The magnitude of the radial damping in comparison to other important terms at a given axial location in the ion radial momentum equation and the heavy species energy equation are shown in Figures C-1 and C-2 respectively.

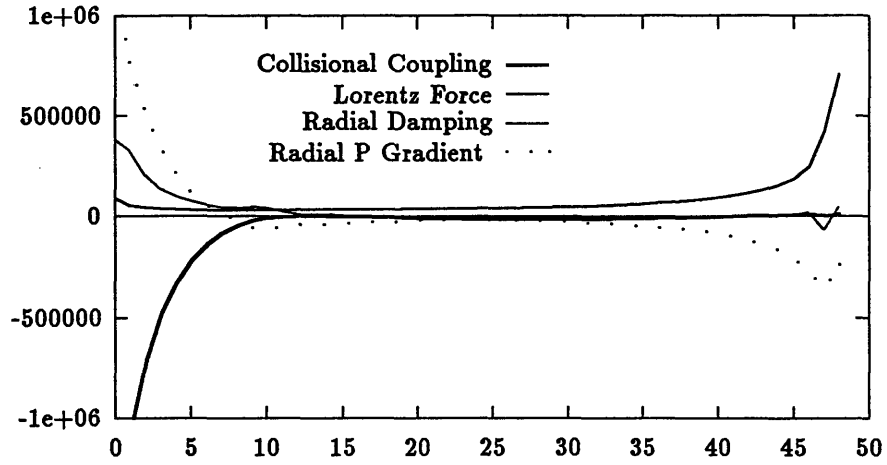

Figure C-1: Relative Magnitude of Damping in the Ion Radial Momentum Equation

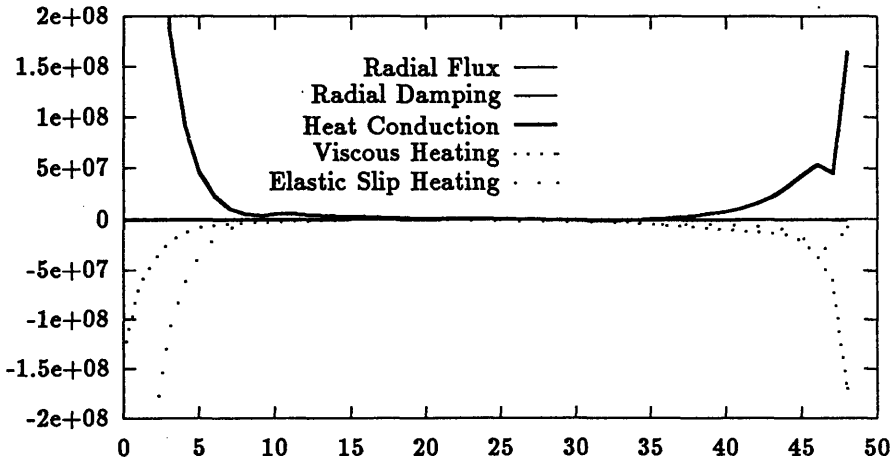

Figure C-2: Relative Magnitude of Damping in the Heavy Species Energy Equation

C.2 Form

Because of their importance, the damping terms are given here in the form they were used for calculating the results given in Chapter 6. The terms are given in pseudo-code form to make this appendix a little shorter.

The variable C is given by

$$C(j) = (\sqrt{\frac{B_\theta^2(25,j)}{2\mu_0(\rho_{25,j} + 5 \times 10^{-5})} + \frac{\gamma P(25,j)}{\rho_{25,j}}} + V_r(25,j))\Delta_z(25,j)$$

while CZ is given by

$$CZ(i,j) = \frac{1}{10}(\sqrt{\frac{B_\theta^2(i,j)}{2\mu_0(\rho_{i,j} + 5 \times 10^{-5})} + \frac{\gamma P(i,j)}{\rho_{i,j}}} + V_{iz}(i,j))\Delta_r(i,j)$$

Now, the radial damping term for the neutral continuity equation is given by

$$q'(i+\frac{1}{2},j,1) = C(j)(\rho_n(i+1,j) - \rho_n(i,j))\frac{i(NR-i-1)}{NR \times NR}.$$

The radial damping term for the neutral axial momentum is given by

$$q'(i+\frac{1}{2},j,2) = C(j)(\rho_n(i+1,j)V_{nz}(i+1,j) - \rho_n(i,j)V_{nz}(i,j))\frac{MULTN(i,j)}{20}$$

where

$$MULTN(i,j) = V_{nr}(i,j)/Max(Max(|V_{nr}(i,j)|i = 1, NR-1), 250.0).$$

The radial damping for the neutral radial momentum is given by

$$q'(i+\frac{1}{2},j,3) = \frac{C(j)}{2}(\rho_n(i+1,j)V_{nr}(i+1,j) - \rho_n(i,j)V_{nr}(i,j)).$$

The damping term for the ion continuity equation is given by

$$q'(i+\frac{1}{2},j,5) = C(j)(\rho_i(i+1,j) - \rho_i(i,j))\frac{i(NR-i-1)}{NR \times NR}.$$

The damping terms for the first ten radial points are then modified to be

$$q'(i+\frac{1}{2},j,5) = q'(i+\frac{1}{2},j,5) - q'(\frac{1}{2},j,5)\frac{10-i}{10}$$

and for the last 10 (i=NR-10 through NR-1) radial points by

$$q'(i+\frac{1}{2},j,5) = q'(i+\frac{1}{2},j,5) - q'(NR-\frac{1}{2},j,5)\frac{NR-1-i}{10}$$

The damping for the ion axial momentum equation is given by

$$q'(i+\frac{1}{2},j,7) = \frac{C(j)}{2}(\rho_i(i+1,j)V_{iz}(i+1,j) - \rho_i(i,j)V_{iz}(i,j))$$

and for the ion radial momentum by

$$q'(i+\frac{1}{2},j,8) = \frac{C(j)}{2}(V_{ir}(i+1,j) - V_{ir}(i,j))\rho_i(i,j)\frac{NR-i-1}{NR-1}$$

The radial fluxes at the first and last radial points are modified somewhat to keep the damping at the boundaries small.

The axial damping term for the ion continuity equation is given by

$$p'(i+\frac{1}{2},j,5) = \frac{CZ(i,j)+CZ(i,j+1)}{4}(\rho_i(i,j+1) - \rho_i(i,j))\frac{i}{NR}.$$

The axial damping term for the ion axial momentum equation is given by

$$p'(i+\frac{1}{2},j,7) = \frac{CZ(i,j)+CZ(i,j+1)}{4}(\rho_i(i,j+1)V_{iz}(i,j+1) - \rho_i(i,j)V_{iz}(i,j))\frac{i}{NR}$$

and for the ion radial momentum equation by

$$p'(i+\frac{1}{2},j,7) = \frac{CZ(i,25)}{2}(V_{ir}(i,j+1) - V_{ir}(i,j))\rho_i(i,j)$$

The axial damping terms at the first two axial locations are set equal to the term at the third axial point.

Appendix D

Numerical Considerations

The focus of this thesis is the use of computational tools to examine the physics of an experimental phenomenon. Nevertheless, some of the details of the computational tools need to be described in somewhat more detail. This appendix attempts to do that. In discussing these details it is important to keep in mind the nature of this work. This is the first work, numerical, experimental, or theoretical, to give detailed information about the state of the plasma inside a high power MPD thruster at more than 2 or 3 random locations. Therefore, many of the numerical aspects of this work are no where near the state of refinement of typical CFD calculations of today or even of 10 years ago. This research is therefore a foundation upon which more exact and efficient simulations can be built.

D.1 Convergence

With the many variables tracked by the simulation, each with its own inherent time scale, it is necessary to be careful in determining whether the solution has converged to a steady state value. This was done by tracking two of the conservation quantities of the equations, the total interelectrode potential drop and the mass flow. The interelectrode potential is the fastest quantity to reach steady state and the one with the quickest variation. Both the spatial variation from axial location to axial location as well as the temporal variation of the average value were tracked. The potential was

deemed to be constant when the standard deviation of the potential spatially was less than 2% of the average value and the temporal variation was less than 0.5 Volts. In general, the spatial variation settles down on time scales of 1×10^{-6} seconds, or 3% of the flow time. The temporal variation does not converge until the fluid variables converge. Convergence of the fluid variables is measured by the average mass flow error, where the mass flow error is the difference between the mass flux integrated from cathode to anode at a given axial location and the integrated mass flux at the inlet. This is the slowest quantity to reach steady state, taking a number of flow times to converge, approximately 1×10^{-4} seconds. The mass flow was assumed to be converged when the average over all axial locations of the error was below 1% and the maximum error at any axial location was below 2%.

D.2 Nonconvergence

As discussed in various sections of this thesis, one of the main problems with running the simulation was nonconvergence of the results. This nonconvergence was not due to asymptotic behaviour of the residuals or unstable runaway of the results. It was always due to an oscillation of the solution. At a given time, the mass flow would begin to rise axially, starting at the inlet or within the first 20% of the channel. The massflow would reach a maximum and then decrease to a minimum below the prescribed inlet value. One or two smaller local extrema would often be seen further downstream. These "waves" varied in height from 5% to 50% of the inlet mass flow. The wavelength was typically 20 to 40% of the electrode length. Over time, the wave would travel down the channel towards the exit, decaying in height as it traveled. The waves traveled with the flow and had periods on the order of the flow time. As one wave decayed a new one would appear, usually with an extremum of the opposite sign as the previous wave. Due to the lack of time accuracy in the simulation, the period of the waves is suspect. As the mass flow oscillated, the average potential also oscillated, although the magnitude of this oscillation varied greatly from case to case, from 1% of the average potential to 40%.

What causes these oscillations? Some attemps have been made to isolate the cause, but they have been inconclusive. Turning off the ion axial momentum equation can turn off or severely limit the oscillation. So can reducing drastically the number of magnetic time field steps taken. So, it would seem that the oscillation does rely on the magnetic field and the fluid equations interacting with each other. Turning the electron temperature equation off did not affect the oscillation at all. The magnetic field equation run on its own always converges. If the fluid variables are integrated for a given frozen magnetic field, the fluid variables go unstable because the plasma density at a few locations goes to zero. A similar convergence problem seemed to exist before ion-neutral slip was included in the simulation, so slip is probably not an important factor in the oscillation.

Is the oscillation physical or numerical? At the power levels simulated, the physical device does not seem to have oscillations of a similar frequency. However, at higher power levels the physical device does go unstable, and the physical oscillation does have some characteristics similar to those seen numerically at lower power levels. This is an open question.

D.3 Use of Dimensional Results

In ordinary fluid dynamics, the important scaling parameters of a flow are well understood and documented. Many CFD calculations are therefore done in non-dimensional variables so that the results can be generalized to many different problems with the same governing parameters. Unfortunately, the true scaling parameters of MPD flows are not well understood. A number of non-dimensional sets of equations were derived for use in this research. However, the number of non-dimensional parameters, the many different scales inherent in the problem, and the order of magnitude variation of such quantities as the viscosity coefficients and thermal conductivities all combined to make the non-dimensional equations hard to interpret and confusing. Therefore, a specific thruster with given dimensions and operating parameters was chosen to be simulated. The chosen thruster was known to exhibit experimentally the behaviour

of interest to this research at some but not all operating conditions. The numerical results of this research can only be applied with a high degree of certainty to this specific thruster at these operating conditions. Hopefully, the insights gained from this work will allow simulations of other thrusters to be performed. Also, this research will hopefully lead to better understanding of the important scaling parameters of the flow and more meaningful non-dimensional operating parameters. The results of this research could then be applied a posteriori to other thruster geometries.

D.4 Use of Damping and Limiters

In standard CFD calculations there is usually no need for limiting the physical variables or for the large amount of damping necessary in this calculation. The limiters used in this research were used to either to keep the simulation stable during transient behaviour or to enhance the convergence properties of the simulation. Those limiters which were not active in the steady state solution have little bearing on the steady state results described in this thesis. Those which were active however, could be obscuring important physics. At the lower currents simulated (23.4 kA and perhaps 27.3 kA) the lower limit on the ionization fraction is forcing the plasma to ignite where there might otherwise be no ionization. However, at the higher currents the lower limit was varied from 5% to 1% with little effect on the results. The upper limits on both electron and heavy species temperatures were only active at the highest current simulated (39.0 kA) and so should not affect the qualitative behavior of the voltage drops and starvation.

The large amounts of numerical damping used could also be obscuring physical behaviour. Damping coefficients were varied in an attempt to determine their effect. Variations in many of the coefficients had little effect on the results unless the coefficients were made an order of magnitude larger. Variation of the coefficients on the more important damping terms, particularly the ion radial momentum and the ion number density, did affect the results quantitatively, although not qualitatively. Again, increasing damping coefficients by an order of magnitude or more did make the

damping terms large enough so that they qualitatively changed the solution, showing no starvation were previous results indicated that the plasma was starved. In general, these coefficients were made as small as they could be and still have the code be stable.

D.5 Validation

In light of some of the concerns raised above, as well as the overall complexity of the code, validity of the numerical results is an issue. Unfortunately, there are no theoretical models of two dimensional thrusters to compare against. There are no computational results at similar power levels to provide comparisons. The simulation without the Hall effect, heavy species heat conduction, and viscosity was compared to results from a one dimensional code which had itself been compared to simpler analytical results. Good agreement was found. Another standard technique, variation of grid spacing, was not attempted because the grid spacing is already at the limit of what can reasonably be simulated on a Cray class supercomputer. The most potent evidence of validity comes from comparison to the experimental results. This code more accurately mimics experiment than any other existing simulation. Therefore, it is presumably more accurate than other codes.

D.6 Code Reconstruction

Although, as discussed in the conclusions of this thesis, the best way to proceed with this work would be to write a new simulation, enough details are given in this thesis to reconstruct the simulation used for this research. However, those details are located at various points in this thesis. The overall flow of the simulation, the general and specific form of the fluid and magnetic field fluxes, the general form of the damping terms, and the limiters used are all described in Section 4.1. The boundary conditions used are given in detail in Section 4.2. The transformed equations are given in Appendix A. The detailed form of the damping terms is given in Appendix

C.

D.7 Advanced Techniques

As discussed in Section 8.3, the best approach to continuing this research would probably be to create a new simulation, rather than reconstruct this one. This research takes a brute force approach to computational methods. The resulting simulation is relatively slow and only first order accurate. This research does not rely on the more elegant techniques developed for CFD in recent years, techniques using ideas such as solving the Riemann problem, diminishing the total variation, or flux corrected transport. Some of those techniques were tried for this research. However, the physics behind some of them is not complex enough to handle the governing equations. For example, many of these methods are not appropriate for equations which are driven by source terms (such as Lorentz force or Ohmic heating) rather than fluid fluxes. Now that there is some understanding of how the plasma inside an MPD thruster is behaving, a faster, more accurate simulation might be developed. This understanding will help make intelligent choices about which advanced CFD techniques might be useful, or give insight to develop new techniques specifically for MPD type flows.

Appendix E

MPDAXI

This appendix describes the actual code which comprises the axisymmetric numerical simulation, the inputs which it requires, the outputs it produces, and the plotting routines created to view the output. The code has been given a name, MPDAXI.

E.1 Input

There are four types of input to the program. The input of most of the run parameters is done through a namelist file. The variables in the namelist file, called "parms.dat" are

dt the fluid time step, in seconds

rl the length of the channel, in meters

rano the inner radius of the anode at the inlet, in meters

rcat the outer radius of the cathode at the inlet, in meters

tfinal the total simulation time, in seconds

tplot the time between screen updates of errors, in seconds

current the total applied current, in amperes,

rmassflow the inlet mass flow, in kilograms/second

The solution from which the simulation starts can be set in either of two ways. If the file "micon.f" is included in the first two lines of the make file(roe.m) then the initial solution is set by the equations in that fortran file. If the file "micon2.f" is included in the make file, the initial solution is taken from the data files "*init.dat". To copy the last saved solution into the initial data files, run the shell file "init" (by typing "sh init" on a Unix system). This shell file copies the files "al.dat", "bh.dat", "er.dat", "rh.dat", "te.dat", "tg.dat", "nr.dat", "nz.dat", "vr.dat", and "vz.dat" into corresponding initialization files.

The third type of input comes from the include files 'dims.f' and 'dims2.f'. The file 'dims.f' contains the variable "NR", the number of radial points in the simulation, "NZ" the number of axial points in the simulation, and "NEQ" the number of governing equation. The file 'dims2.f' contains the variable "NELEC", the number of axial points which make up the electrodes (assumed to have the same length). For all of the cases run for this thesis, NR = 50, NZ = 50 ,NELEC = 40, and NEQ = 8.

The fourth type of input is the grid on which the equations are solved. The grid is contained in a file "grid.dat". It is written as 2 (NR + 1) lines of NZ + 1 formatted data points, starting with the r values of the line nearest the cathode. The second line contains the z values of the same line. The r values are manipulated in a somewhat strange way to get the grid, mostly because the grid being used is a remnant of a two-dimensional formulation with the anode as the lower electrode.

E.2 Output

The main output of the program is 26 data files each containing the values of one of the flow properties. Each output file consists of NR+2 lines, the first being the time at which the simulation ended, and the rest the data for all the points. Each line gives the data along an axial line of the grid, starting at the cathode and ending at the anode. The files are written formatted. The name of all the files are a two letter prefix denoting the variable followed by ".dat". The two letter prefixes are

al ionization fraction

bh azimuthal magnetic field strength

cr transverse current density

cz axial current density

er transverse electric field

ez axial electric field

ir transverse ion velocity

iz axial ion velocity

ma massflow

mh Mach number

ne electron number density

nn neutral number density

nr transverse neutral velocity

nz axial neutral velocity

pe electron pressure

pn neutral pressure

pr fluid pressure

pt potential difference with respect to cathode

rh global mass density

sg electrical conductivity

te electron temperature

tg heavy species temperature

ur radial slip velocity

uz axial slip velocity

vr radial global velocity

vz axial global velocity

The program also outputs some diagnostic information to the screen at intervals specified in the input namelist file. This diagnostic information includes the maximum mass flow error and the j location of the point at which it occurs, the maximum fluid Courant number in the simulation, the maximum electron Courant number followed by its i,j location, the maximum ratio of the fluid diffusive time scale to the time step and its i,j location, and the average mass flow error. The simulation also periodically outputs the number of electron time steps being taken, the number of magnetic field time steps, and a measure of the stability of the magnetic field boundary condition, the maximum Hall Courant number.

E.3 Compiling, Linking, and Running the Code

The fortran files necessary for compiling and linking MPDAXI are

anode3.f Solves the anode model.

comall.f Contains the common blocks and the variable declarations.

cond.f Determine the heavy species heat conduction source terms.

constant.f Sets the physical constants.

current2.f Solves for the current for the fluid equations.

define2.f Set the local axial upwind and downwind fluxes and the transverse fluxes.

dims.f Sets the number of axial and radial points and number of governing equations.

dims2.f Sets the number of electrode points.

echeck2.f Checks and outputs the average and maximum mass flow errors.

gridgen.f Calls a routine to read the grid and set the metrics.

mag2.f Updates the magnetic field equation.

main.f The main program.

mbcon2.f Sets the boundary conditions.

micon.f Creates an initial solution.

micon2.f Reads in the initial solution from the saved solution.

msvar2.f Saves the data.

mvupd.f Updates the physical variables based on the integration variables.

nmanode.f Solves the anode model for the first pass through.

nsol.f Computes the new solution.

pcheck.f Determines the average potential and its variation.

roe.f Calls the fluid update subroutines.

rusanovn2.f Computes the damping terms.

source2.f Computes the source terms and transport coefficients.

spar.f Reads in the namelist data.

swflux.f Sets the fluid fluxes.

tccheck.f Checks the time step limitations.

tcurrent2.f Computes the current for the magnetic field equation.

tefield.f Computes the electric field.

temac2.f Updates the electron energy equation.

temvu3.f Computes the electron velocities.

tesou2.f Calculates the source terms for the electron energy equation.

teste.f Determines the maximum electron energy equation time step.

teup3.f Calls the electron temperature update subroutine.

teuvu.f Limits the electron temperature.

tgnew.f Determines the viscosity source terms for the momentum and heavy species energy equations.

tgste.f Determines the maximum time step for the fluid diffusive source terms.

thomas2.f Uses Thomas algorithm to solve for electron temperature.

tmarch.f Marches the simulation forward in time.

vcoef.f Reads the grid and calculates the various metrics.

On Unix based systems the file "roe.m" is used to compile all of the necessary fortran files, producing object files labeled with the suffix ".o", and then link them together into the executable image "mpdaxi". This is done by typing "make -f roe.m". The required fortran options can be specified in the make file. Typical options are "-g" to enable debugging, "-O4" to enable optimized compiling, "-r8" to use double precision variables, and "-static" to inhibit reinitialization of local subroutine variables.

Once the program is compiled, the run parameters, mainly the run time and fluid time step, need to be set. The fluid time step should be set as high as possible without the simulation going unstable. Typical fluid times steps are on the order of 1.5×10^{-9} seconds. Time to a converged solution is one the order of 1 to 0.1 milliseconds (starting from a reasonable solution). On a Decstation 5000, 100 fluid time steps takes on the order of 3 to 15 minutes, depending on the number of magnetic field and electron temperature time steps taken for each fluid time step.

Once the input parameters are set, the code can be run by typing "mpdaxi". In order to have the screen output sent to a file, type "mpdaxi > filename". In order to have the program run in the background, type "mpdaxi > filename &". To set the priority low for long run time programs, type "nice +10 mpdaxi > filename &". These commands may be substantially different for non-Unix based systems.

Once the program is finished, the data needed to start a new run from the current time can be set by typing "sh init". The data can be plotted using the graphics program described in the Section E.5.

E.4 Strategies for Running the Code

If you use a geometry and operating conditions for which a reasonably good solution exists (and is input to the simulation), and use a short enough time step (typically so that the maximum diffusive ratio is less than 0.9 and the Courant number less than 0.15), the code may run until the final time set in the input file. Usually however, the solution will go unstable and the code will crash.

There are a number of things that can be tried when this happens. If it happens very early in a run that was started for a new geometry or operating conditions, the initial conditions may be at fault. The simulation does take into account a new total current or massflow and tries to adapt the initial condition for the new operating parameters. However, if the change is too severe the user may have to modify the initial conditions. Alternatively, particularly if the instability arises in the electron temperature or ionization fraction, taking a number of very short time steps to start the simulation may be helpful.

If the operating conditions have not been changed recently, solving the problem requires more investigation. The magnetic field or electron temperature time steps may be too large. The safety factors on these time steps can be modified by changing the variable INDEX in MAG or SSTEP respectively. If it is seen that the electron Courant number is increasing indefinitely, it may be that not enough magnetic field time steps are being taken. The number can be increased, again by modifying INDEX

in MAG. If these simple solutions do not work, damping terms must be modified. This is a fairly complex operation and should only be undertaken after one has familiarized herself or himself with the code as a whole.

E.5 Plotting Results

For systems which have the plotting package Grafic, a plotting program called MAKEPLOT has been developed. In order to compile and link MAKEPLOT, the files "plot.m", "makeplot.f", and "proutines.f" are necessary. Typing "make -f plot.m" compiles and links the plotting program. The file "plot.m" may have to be changed slightly depending on the location of the Grafic library. Typing "makeplot" runs the graphics program, which lists the variables which can be plotted and their index number. After entering the index number the program prompts for input to plot an axial cut (enter the line number), a radial cut (enter the negative of the radial line minus 1), a contour plot (enter NR + 1), a surface plot (NR+2), three axial lines (NR + 3), or five radial cuts (NR +4) . In the plot window, the standard Grafic options are available. Type "x" to exit the plot and return to the variable list. The file "title.dat" gives the title printed at the top of each plot.

Appendix F

One Dimensional Models and Results

Given that the main result of this thesis is a two dimensional model, perhaps the continued importance of one dimensional modelling should be stressed. There are some flow characteristics which can only be derived from a two dimensional model, and some which can not be found with any fluid model, even of three dimensions. However, there are other parameters which can be accurately predicted by one dimensional models. For example, Martinez-Sanchez [45] and others have shown that thrust is well predicted by even simple one dimensional calculations. Also. these models yield results quickly and can be used to generate solutions for a very wide range of geometries and operating parameters, as done by Preble [57] using the one dimensional model developed by the author. One dimensional simulations are also helpful in isolating the effects of specific changes in a model, such as a different ionization model or the inclusion of velocity slip, changes which may get lost in the complexity of a multi dimensional simulation.

As discussed in Section 2.2, a number of one dimensional models of MPD thrusters exist. These models range from simple one fluid models to complex two fluid models. To date however, the most complete one dimensional model was developed as the first stage in this research. An early version of this model is described in a Master's thesis[53] while a slightly updated version is described by Niewood and Martinez-

Sanchez [55]. This chapter describes at some length the most recent version of the one dimensional work. The governing equations are derived as simplifications of the more complete axisymmetric equations given in the previous chapter. These equations, and their deriviation, are described in the following section. Sections F.2 - F.4 detail respectively the boundary conditions, solution technique, and results for the one dimensional model.

F.1 Governing Equations

The governing equations for the quasi one dimensional model can be derived by integrating the axisymmetric equations from one side wall to the other. For example, the ion continuity equation can be integrated,

$$\int_{r_c(z)}^{r_a(z)} \left(\frac{\partial \rho_i r}{\partial t} + \frac{\partial r \rho_i V_{ir}}{\partial r} + \frac{\partial r \rho_i V_{iz}}{\partial z} - r m_i \dot{n}_e \right) dr = 0 \tag{F.1}$$

So,

$$\int_{r_c(z)}^{r_a(z)} \frac{\partial \rho_i r}{\partial t} dr + \rho_i r V_{ir} |_{r_c(z)}^{r_a(z)} + \int_{r_c(z)}^{r_a(z)} \frac{\partial \rho_i r V_{iz}}{\partial z} dr = \int_{r_c(z)}^{r_a(z)} r m_i \dot{n}_e dr \tag{F.2}$$

By defining a cross section average,

$$\overline{f} A = 2\pi \int_{r_c(z)}^{r_a(z)} r f dr$$

the above equation can be written as

$$\frac{\partial \overline{\rho_i} A}{\partial t} + 2\pi \left[\rho_i V_{ir} |_{r_a} r_a - \rho_i V_{ir} |_{r_c} r_c \right] + \frac{\partial \overline{\rho_i V_{iz}} A}{\partial z} - 2\pi \rho_i V_{iz} |_{r_a} r_a \frac{\partial r_a}{\partial z} + 2\pi \rho_i V_{iz} |_{r_c} r_c \frac{\partial r_c}{\partial z} = m_i \overline{\dot{n}_e} A \tag{F.3}$$

Since there is no bulk flow through the side walls and no flow along the side walls,

$$V_r(r = r_{a,c}) = V_z(r = r_{a,c}) = 0$$

Since the ions enter the wall at the Bohm velocity,

$$V_{ir}(r = r_{a,c}) = \pm \frac{V_b}{\sqrt{1 + (\frac{\partial r_{a,c}}{\partial z})^2}}$$

and

$$V_{iz}(r = r_{a,c}) = \frac{V_b \frac{\partial r_{a,c}}{\partial z}}{\sqrt{1 + (\frac{\partial r_{a,c}}{\partial z})^2}}$$

Using the definition of the bulk velocity yields the neutral wall velocity,

$$V_{nr}(r = r_{a,c}) = \mp \frac{\alpha}{1 - \alpha} \frac{V_b}{\sqrt{1 + (\frac{\partial r_{a,c}}{\partial z})^2}}$$

and

$$V_{nz}(r = r_{a,c}) = -\frac{\alpha}{1 - \alpha} \frac{V_b \frac{\partial r_{a,c}}{\partial z}}{\sqrt{1 + (\frac{\partial r_{a,c}}{\partial z})^2}}.$$

So,

$$\frac{\partial \overline{\rho_i} A}{\partial t} + \frac{\partial \overline{\rho_i V_{iz}} A}{\partial z} = m_i \dot{\overline{n}}_e A - 2\pi V_b \left(\rho_i|_{r_a} r_a (1 + (\frac{\partial r_a}{\partial z})^2)^{-\frac{1}{2}} + \rho_i|_{r_c} r_c (1 + (\frac{\partial r_c}{\partial z})^2)^{-\frac{1}{2}} \right) \tag{F.4}$$

Since the radial electron number density distribution is not known, it is assumed, for no particular reason, that it is parabolic with non zero density at the walls. The ambipolar ion flux into the walls must be equal to the local electron number density multiplied by the Bohm velocity, so

$$\frac{\partial n_e}{\partial r} |_{wall} = \frac{n_e V_b}{D_a} \tag{F.5}$$

Given the average electron number density at any axial location $\bar{n}_e(z)$, the radial dependence of n_e is

$$n_e(r, z) = \frac{-6\bar{n}_e}{r_a^2 + r_c^2 - 2r_a r_c + 6\frac{D_a}{V_b}(r_a - r_c)} \left(r_a r_c - \frac{D_a}{V_b}(r_a - r_c) - (r_a + r_c) r + r^2 \right) \tag{F.6}$$

So, the electron number density at the anode equals the electron number density at

the cathode and is given by

$$n_e(r_a, r_c) = \frac{6\overline{n}_e \frac{D_a}{V_b}}{r_a - r_c + 6\frac{D_a}{V_b}}.$$

The one dimensional ion continuity equation is then given by

$$\frac{\partial n_e A}{\partial t} + \frac{\partial n_e V_z A}{\partial z} = (\dot{n}_{e,I} - \dot{n}_{e,R})A - 2\pi \frac{6 D_a \overline{n}_e}{r_a - r_c + 6\frac{D_a}{V_b}} (r_a(1+(\frac{\partial r_a}{\partial z})^2)^{-\frac{1}{2}} + r_c(1+(\frac{\partial r_c}{\partial z})^2)^{-\frac{1}{2}}) \tag{F.7}$$

The other equations can be derived similarly, as shown in the following chapter, Appendix G. The quasi one dimensional neutral conservation equation is

$$\frac{\partial \overline{\rho_n} A}{\partial t} + \frac{\partial \overline{\rho_n V_{nz}} A}{\partial z} = -m_i \overline{\dot{n}_e} A + 2\pi V_b \left(\rho_i|_{r_a}(1 + (\frac{\partial r_a}{\partial z})^2)^{-\frac{1}{2}} + \rho_i|_{r_c}(1 + (\frac{\partial r_c}{\partial z})^2)^{-\frac{1}{2}} \right) \tag{F.8}$$

The derivation of the axial momentum equations assumes that each of the species pressures is constant radially, that the axial species velocities are zero at the wall, and that the axial current is zero everywhere. The resulting equations are

$$\frac{\partial \overline{\rho_n V_{nz}} A}{\partial t} + \frac{\partial \overline{\rho_n V_{nz}^2} A}{\partial z} + A\frac{\partial P_n}{\partial z} = \overline{S_{nz}} A + \overline{K_{ni}(V_{iz} - V_{nz})} A - m_i \overline{\dot{n}_{e,I} V_{nz}} A + m_i \overline{\dot{n}_{e,R} V_{iz}} A \tag{F.9}$$

and

$$\frac{\partial \overline{\rho_i V_{iz}} A}{\partial t} + \frac{\partial \overline{\rho_i V_{iz}^2} A}{\partial z} + A\frac{\partial \overline{(P_e + P_i)}}{\partial z} = 2\pi J_r(r = r_c) B(r = r_c) r_c^2 \ln(\frac{r_a}{r_c})$$

$$+ \overline{S_{iz}} A + \overline{K_{in}(V_{nz} - V_{iz})} A + \overline{\dot{n}_{e,I} V_{nz} - \dot{n}_{e,r} V_{iz}} m_i A. \tag{F.10}$$

The heavy species energy equation can be written as

$$\frac{\partial \frac{3}{2} P_g A}{\partial t} + \frac{\partial \frac{3}{2} P_g \overline{V_z} A}{\partial z} + P_g \frac{\partial \overline{V_z} A}{\partial z} = -\overline{E_l} A + \overline{(K_{in} + \frac{1}{2} m_i \dot{n}_e)(U_r^2 + U_z^2)} A$$

$$+ \frac{6(r_a^2 - r_c^2)}{(r_a - r_c)^2} \left[(v_{ii} + v_{in}) \overline{V_{iz}^2} + (v_{ni} + v_{nn}) \overline{V_{nz}^2} \right] + \overline{\kappa_g} A \tag{F.11}$$

The electron energy equation can be written as

$$\frac{\partial \frac{3}{2} P_e A}{\partial t} + \frac{\partial \frac{3}{2} P_e \overline{V_{ez}} A}{\partial z} + P_e \frac{\partial \overline{V_{ez}} A}{\partial z}$$

$$= \frac{2\pi}{\sigma} J_r^2(r_c) r_c^2 \ln(\frac{r_a}{r_c}) + \overline{E_l} A + \overline{\dot{n}_{e,I}(\frac{3}{2}kT_g - E_i)A} - \overline{\dot{n}_{e,R}(\frac{3}{2}kT_e - E_i)A}$$

$$+ \overline{\kappa_e} A - 5\pi \left[P_e V_b|_{r_a} r_a (1 + (\frac{\partial r_a}{\partial z})^2)^{-\frac{1}{2}} + P_e V_b|_{r_c} r_c (1 + (\frac{\partial r_c}{\partial z})^2)^{-\frac{1}{2}} \right]. \qquad \text{(F.12)}$$

Finally, the magnetic field equation, neglecting the Hall and electron pressure terms, is given by

$$\ln \frac{r_a}{r_c} \frac{\partial b}{\partial t} + \frac{\partial}{\partial z} \left(V_{iz} b \ln \frac{r_a}{r_c} \right) - \frac{\partial}{\partial z} \left(\frac{1}{\mu_0 \sigma} \right) \frac{\partial b}{\partial z} \ln \frac{r_a}{r_c} - \frac{1}{\mu_0 \sigma} \frac{\partial b}{\partial z} \frac{d}{dz} (\ln \frac{r_a}{r_c}) = \frac{1}{\mu_0 \sigma} \ln \frac{r_a}{r_c} \frac{\partial^2 b}{\partial z^2} \qquad \text{(F.13)}$$

where $b = b(z) = B_\theta(r, z) r$. The radial current, J_r is given by

$$J_r(r, z) = -\frac{1}{\mu_0} \frac{\partial B_\theta}{\partial z} = -\frac{1}{\mu_0 r} \frac{db}{dz} \qquad \text{(F.14)}$$

To close the system of equations, the various average quantities, both the source terms and the plasma properties, must be connected to each other. To do this, a leap of faith will be used and the variables will be assumed to be independent, so that, for example,

$$\overline{\rho V_z} = \bar{\rho} \times \bar{V}_z.$$

It will also be assumed that the various average source terms can be evaluated as functions of the average plasma properties.

F.2 Boundary Conditions

At the inlet of the thruster the mass flow, total temperature, and total applied current are given as operating parameters of the device. The applied current determines $b(0)$ as

$$I = \frac{2\pi r B_\theta(r, 0)}{\mu_0} = \frac{2\pi b(0)}{\mu_0}$$

so that

$$b(0) = \frac{\mu_0 I}{2\pi}$$

The inlet ionization fraction is assumed to be constant and small, and the density is found by a downwind difference,

$$\frac{\partial \rho(0)}{\partial t} = \frac{4\rho(1)V_z(1)A(1) - 3\rho(0)V_z(0)A(0) - \rho(2)V_z(2)A(2)}{A(0)\Delta x}$$

At the exit the magnetic field is set to zero. The other variables are found from fluid characteristic theory, just as the exit boundary conditions are found for the axisymmetric simulation, as described later in Chapter 4, except that the pressure for subsonic exit is set to some low value.

F.3 Numerical Method

The numerical method used is simply the axial portion of the axisymmetric numerical scheme described later in Chapter 4, except that the electron temperature equation is solved with the other fluid equations. The electron heat conduction term is treated separately at a faster time scale. For the results shown below, the simulation region was divided into 100 points. A time step of 5×10^{-9} seconds was used. Steady state was reached in approximately 1×10^{-4} seconds of simulation time and about 15 minutes of CPU time on a DecStation 5000 (a Unix based workstation). The fortran routines used to create program and the input and the output of the program are described in Appendix H

F.4 Results

Different versions of the one dimensional simulation have been used for a variety of purposes and documented in a number of articles, reports, and theses. The original simulation was used to show the importance of two fluid modeling, ambipolar diffusion, viscous effects, electron heat conduction, and area variation in the CAC

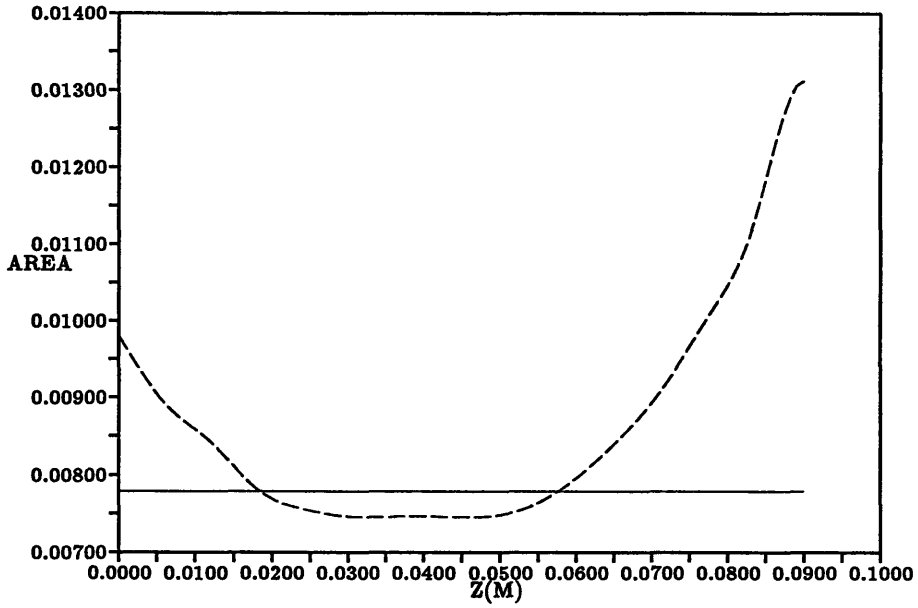

Figure F-1: Channel Cross Sectional Area in the CAC and FFC Channels.

and FFC thrusters of Heimerdinger, Kilfoyle, and Martinez-Sanchez. This form of the simulation involved a one dimensional model of a two dimensional thruster. This work is documented in a Master's thesis by the author [53]. Similar work including a model of velocity slip is described in a journal article [55]. Preble [57] used the original simulation to predict the onset of the electrothermal instability in a variety of thruster geometries over a wide range of operating conditions. A somewhat more recent version was used to model an axisymmetric dense plasma gun assuming constant average radius [54].

The current version of the one dimensional code was used to model the same thruster as modeled with the axisymmetric code, the CAC and FFC of Heimerdinger, Kilfoyle, and Martinez-Sanchez [25, 30]. For these runs the correct electrode length of 0.09 m was used. Both thrusters were modeled at a current of 31.2 kA. Both cases used a constant anode inner radius of 0.072 m. The CAC had a constant outer cathode radius of 0.052 m, while the FFC outer cathode radius was set using a fit to various points read from the FFC specifications. The channel crossectional area used for the FFC and CAC are plotted in Figure F-1.

The Mach number in both channels is shown in Figure F-2. Mach number is

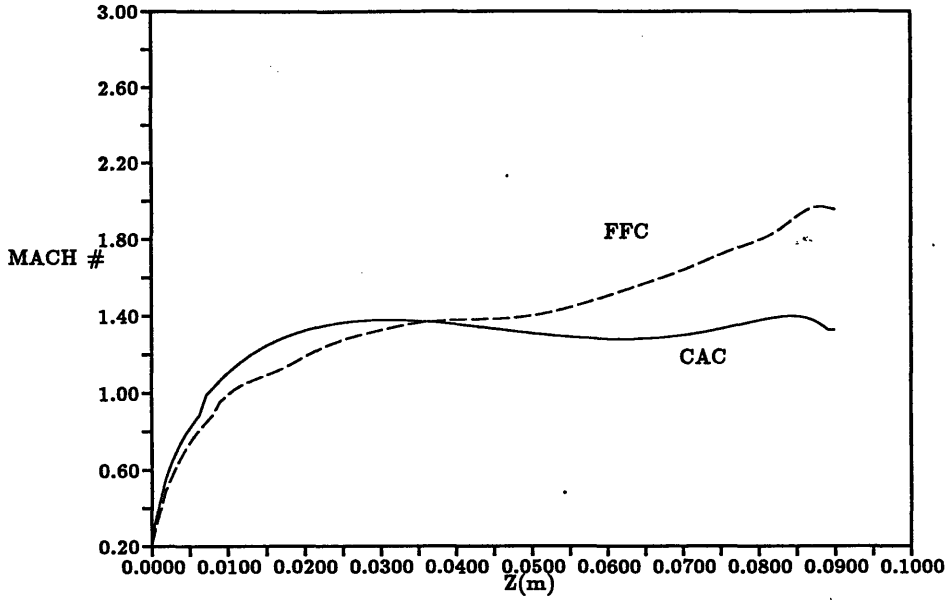

Figure F-2: Mach Number in the CAC and FFC Channels.

defined as

$$M = \frac{V_z}{\sqrt{\frac{5P}{3\rho}}}.$$

The flow in the CAC is choked due to the influence of the viscous forces. The expansion of the FFC allows the Mach number in that channel to continue to increase along its length. The velocity in the FFC is correspondingly higher, as shown in Figure F-3.

Another difference between the two channels is the magnetic field profiles and the distribution of the current. The magnetic field distribution at the cathode is shown in Figure F-4. The cathode magnetic field at the inlet of the FFC is larger than in the CAC because of the smaller radius at the cathode base in the FFC. This leads to a higher current concentration at the inlet of the FFC, as shown in the plot of cathode radial current density, Figure F-5. However, because the current wants to flow across the shortest distance between the electrodes, current in the FFC is more evenly distributed than in the CAC, and the exit current concentration is substantially smaller in the FFC.

The voltage obtained for the CAC was 7.1 Volts and for the FFC 7.8 Volts. The thrust, neglecting pressure forces, was 20.5 N in the CAC and 28.0 in the FFC. This corresponds to an efficiency of 23.7% for the CAC and 40.2% for the FFC.

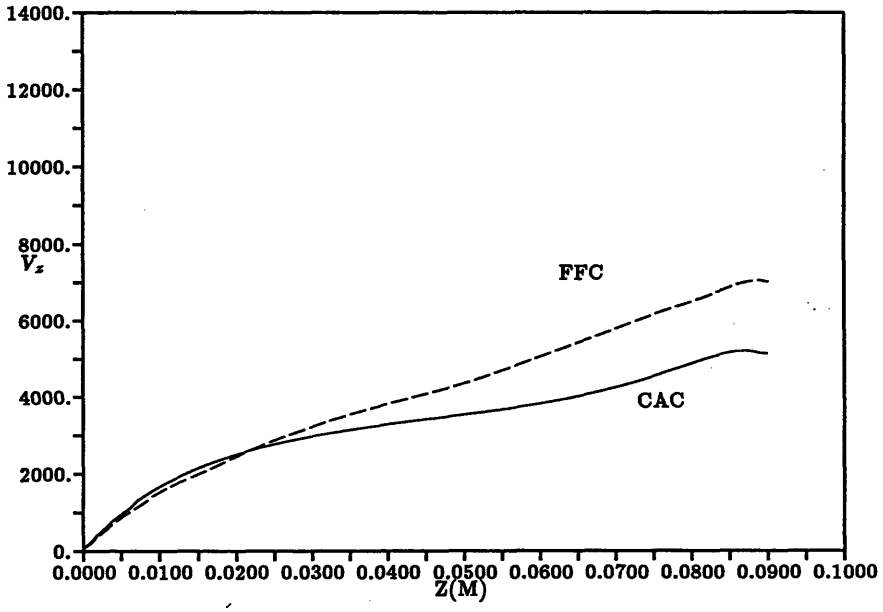

Figure F-3: Global Axial Velocity in the CAC and FFC Channels.

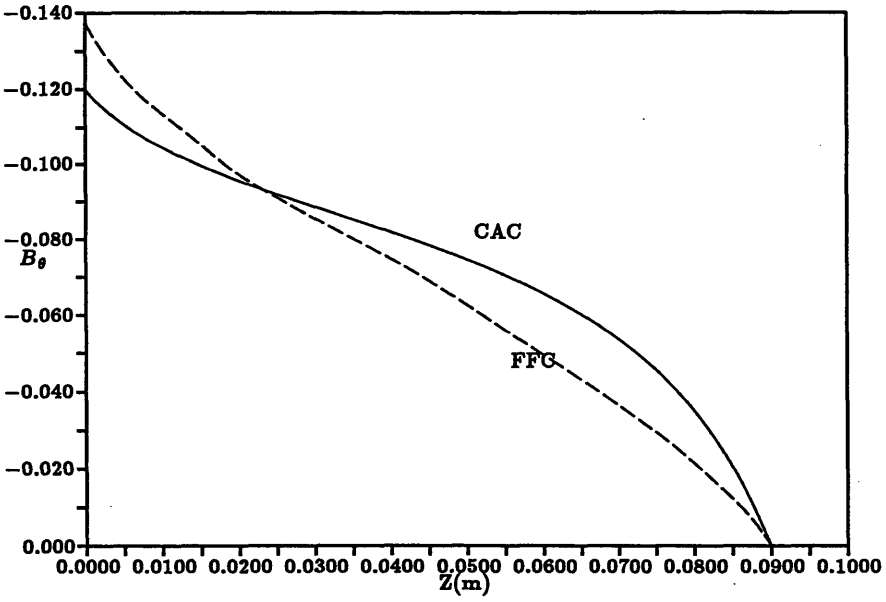

Figure F-4: Cathode Magnetic Field Strength in the CAC and FFC Channels.

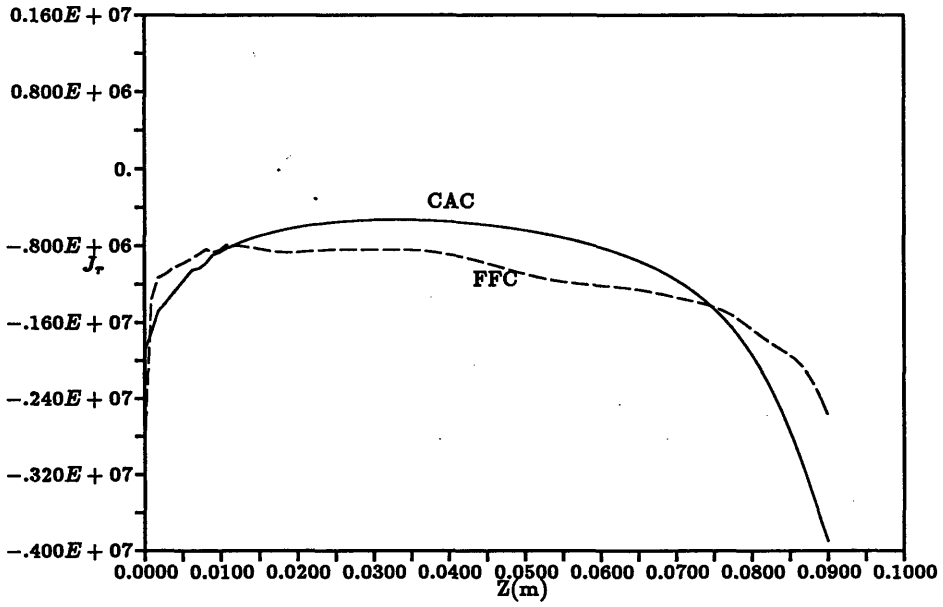

Figure F-5: Cathode Radial Current Density in the CAC and FFC Channels.

Appendix G

Detailed Derivation of Quasi One Dimensional Equations

The quasi one dimensional equations are derived by integrating the axisymmetric equations over the radial crossection. The derivation of the ion continuity equation is given in detail in the text. It relies on the relation

$$\int_{r_c}^{r_a} \frac{\partial f}{\partial z} dr = \frac{\partial}{\partial z} \int_{r_c}^{r_a} f dr - f(r_a) \frac{\partial r_a}{\partial z} + f(r_c) \frac{\partial r_c}{\partial z} \tag{G.1}$$

The details of the derivations of the other equations are given here. The quasi one dimensional neutral conservation equation is derived in the same manner as the ion continuity equation. The ambipolar axial momentum equation is found by integrating the corresponding axisymmetric equation

$$2\pi \int_{r_c}^{r_a} \left[\frac{\partial (r n_e m_i V_{iz})}{\partial t} + \frac{\partial (r n_e m_i V_{ir} V_{iz})}{\partial r} + \frac{\partial r (n_e m_i V_{iz}^2 + P_i + P_e)}{\partial z} - r J_r B_\theta \right] - r S_{iiz} - r S_{inz}$$

$$- r K_{in}(V_{nz} - V_{iz}) - r K_{en}(V_{nz} - V_{ez}) - r \dot{n}_{e,I} m_i V_{nz} + r \dot{n}_{e,R} m_i V_{iz} dr = 0 \tag{G.2}$$

Taking the integrals,

$$\frac{\partial \overline{\rho_i V_{iz} A}}{\partial t} + 2\pi r \rho_i V_{iz} V_{ir} |_{r_c}^{r_a} + \frac{\partial \overline{(\rho_i V_{iz}^2 + P_i + P_e) A}}{\partial z} - 2\pi r_a (\rho_i V_{iz}^2 + P_i + P_e)|_{r_a} \frac{\partial r_a}{\partial z}$$

$$+2\pi r_c(\rho_i V_{iz}^2 + P_i + P_e)|_{r_c}\frac{\partial r_c}{\partial z} - 2\pi\int_{r_c}^{r_a} r\left[J_r B_\theta + v_{ii}\frac{\partial^2 V_{iz}}{\partial r^2} + v_{in}\frac{\partial^2 V_{nz}}{\partial r^2}\right]dr$$

$$-\overline{(K_{in}(V_{nz}-V_{iz}) + K_{en}(V_{nz}-V_{ez}) + \dot{n}_{e,I}m_i V_{nz} - \dot{n}_{e,R}m_i V_{iz})}A = 0. \qquad \text{(G.3)}$$

It will be assumed that the current parallel to the electrodes is everywhere zero. Then the product rB_θ is constant along any radial line as is $rJ_r = \frac{-r}{\mu_0}\frac{\partial B_\theta}{\partial z}$. The cross section average of the Lorentz force is then given by

$$\overline{J_r B_\theta} = \frac{1}{r_a^2 - r_c^2}\int_{r_c}^{r_a} rJ_r B_\theta dr,$$

where

$$\int_{r_c}^{r_a} rJ_r B_\theta dr = \int_{r_c}^{r_a} r\frac{J_r(r_c)r_c}{r}\frac{B_\theta(r_c)r_c}{r}dr = r_c^2 J_r(r_c)B_\theta(r_c)\ln\frac{r_a}{r_c}$$

The axial species velocities are assumed to have parabolic distributions with zero value at the wall. The resulting velocity distribution is given by

$$V_{sz}(r,z) = 6\overline{V}_{sz}(z)\frac{(r_a - r)(r - r_c)}{(r_a - r_c)^2} \qquad \text{(G.4)}$$

So, the second derivative of the axial velocity in the radial direction is a constant,

$$\frac{\partial^2 V_{sz}}{\partial r^2} = \frac{-12\overline{V_{sz}}}{(r_a - r_c)^2}$$

With these assumptions and the no flow into the wall condition from Chapter F, the ion axial momentum equation can be rewritten as

$$\frac{\partial\overline{\rho_i V_{iz}}A}{\partial t} + 2\pi r_a\rho_i V_{iz}|_{r_a}\left(V_{iz}(r_a)\frac{\partial r_a}{\partial z} + V_b(1 + (\frac{\partial r_a}{\partial z})^2)^{-\frac{1}{2}} - V_{iz}\frac{\partial r_a}{\partial z}\right)$$

$$-2\pi r_c\rho_i V_{iz}|_{r_c}\left(V_{iz}(r_c)\frac{\partial r_c}{\partial z} - V_b(1 + (\frac{\partial r_c}{\partial z})^2)^{-\frac{1}{2}} - V_{iz}(r_c)\frac{\partial r_c}{\partial z}\right) + \frac{\partial\overline{(\rho_i V_{iz}^2 + P_i + P_e)A}}{\partial z}$$

$$-2\pi r_a(P_i + P_e)|_{r_a}\frac{\partial r_a}{\partial z} + 2\pi r_c(P_i + P_e)|_{r_c}\frac{\partial r_c}{\partial z} - 2\pi J_r(r_c)B_\theta(r_c)r_c^2\ln\frac{r_a}{r_c}$$

$$+\frac{24\pi}{(r_a - r_c)^2}(v_{ii}\overline{V_{iz}} + v_{in}\overline{V_{nz}}) - \overline{((K_{in} + K_{en})(V_{nz} - V_{iz}) + \dot{n}_{e,I}m_i V_{nz} - \dot{n}_{e,R}m_i V_{iz})}A = 0. \qquad \text{(G.5)}$$

Assuming that the axial velocity at the electrodes is zero and that the electron and ion pressures are constant radially,

$$\frac{\partial\overline{\rho_i V_{iz} A}}{\partial t} + \frac{\partial\overline{\rho_i V_{iz}^2 + P_i + P_e A}}{\partial z} - (P_i + P_e)\frac{\partial A}{\partial z} = 2\pi J_r(r_c) B_\theta(r_c) r_c^2 \ln\frac{r_a}{r_c}$$

$$-\frac{24\pi}{(r_a - r_c)^2}(v_{ii}\overline{V_{iz}} + v_{in}\overline{V_{nz}}) + \overline{(K_{in} + K_{en})(V_{nz} - V_{iz}) + \dot{n}_{e,I} m_i V_{nz} - \dot{n}_{e,R} m_i V_{iz}}. \quad \text{(G.6)}$$

The neutral momentum equation is derived similarly with the assumptions that $V_{nz}(r_a, r_c) = 0$ and that P_n is constant radially.

Taking the integral of the electron energy equation

$$2\pi \int_{r_c}^{r_a} \left[\frac{\partial(\frac{3}{2}P_e r)}{\partial t} + \frac{\partial(\frac{3}{2}P_e V_{er} r)}{\partial r} + \frac{\partial(\frac{3}{2}P_e V_{ez} r)}{\partial z} + P_e(\frac{\partial V_{er} r}{\partial r} + \frac{\partial r V_{ez}}{\partial z}) + r\left(\frac{2K_{en}}{en_e}\mathbf{J}\cdot\mathbf{U} - \frac{J^2}{\sigma} - K_{en}U^2\right.\right.$$

$$\left.\left. - K_{ei}\frac{3k}{m_n}(T_i - T_e) - K_{en}\frac{3k}{m_n}(T_n - T_e) + \dot{n}_{e,R}(\frac{3}{2}kT_e - E_i) - \dot{n}_{e,I}(\frac{3}{2}kT_e - E_i) - \kappa_e\right)\right] = 0 \quad \text{(G.7)}$$

Taking the integral yields

$$\frac{\partial(\overline{\frac{3}{2}P_e A})}{\partial t} + 2\pi\left[\frac{3}{2}P_e V_{er}|_{r_a} r_a - \frac{3}{2}P_e V_{er}|_{r_c} r_c\right] + \frac{\partial(\frac{3}{2}P_e V_{ez} A)}{\partial z} - 2\pi\frac{3}{2}\left[P_e V_{ez}|_{r_c} r_c - P_e V_{ez}|_{r_a} r_a\right]$$

$$+ 2\pi\int_{r_c}^{r_a}[P_e(\frac{\partial V_{er} r}{\partial r} + \frac{\partial r V_{ez}}{\partial z})] = \frac{J_r^2(r_c) r_c^2}{\sigma}\ln\frac{r_a}{r_c} + \overline{AK_{en}U^2 + K_{ei}\frac{3k}{m_n}(T_i - T_e)}$$

$$\overline{+ AK_{en}\frac{3k}{m_n}(T_n - T_e) - \dot{n}_{e,R}(\frac{3}{2}kT_e - E_i) + \dot{n}_{e,I}(\frac{3}{2}kT_e - E_i) + \kappa_e} \quad \text{(G.8)}$$

The radial electron velocity at the walls is given by

$$V_{er}(r_a) = V_{ir}(r_a) - \frac{J_r}{en_e} = \frac{V_b}{\sqrt{1 + (\frac{\partial r_a}{\partial z})^2}} - \frac{J_r}{en_e}$$

Since it has already been assumed that $n_e(r_a) = n_e(r_c)$ and P_e is constant radially,

$$(P_e\frac{J_r}{en_e})_{r_a} - (P_e\frac{J_r}{en_e})_{r_c} = 0$$

So,

$$\frac{\partial(\frac{3}{2}P_eA)}{\partial t} + 5\pi P_e\left[V_b(1+(\frac{\partial r_c}{\partial z})^2)^{-\frac{1}{2}} + V_b(1+(\frac{\partial r_a}{\partial z})^2)^{-\frac{1}{2}}\right] + \frac{\partial(\frac{3}{2}P_eV_{ez}A)}{\partial z}$$

$$+\frac{\partial A\overline{V_{ez}}}{\partial z} = \frac{J_r^2(r_c)r_c^2}{\sigma}\ln\frac{r_a}{r_c} + \overline{AK_{en}U^2 + K_{ei}\frac{3k}{m_n}(T_i-T_e) + K_{en}\frac{3k}{m_n}(T_n-T_e)}$$

$$\overline{+ A\dot{n}_{e,I}(\frac{3}{2}kT_e - E_i) - \dot{n}_{e,R}(\frac{3}{2}kT_e - E_i) + \kappa_e} \qquad \text{(G.9)}$$

The derivation of the heavy species equation proceeds in a similar manner except for the viscous source terms. All of the terms except the radial second derivative of the axial velocity are neglected, so that

$$\int_{r_c}^{r_a}\Phi dr = \int_{r_c}^{r_a} r\left[(v_{ii}+v_{in})(\frac{\partial V_{iz}}{\partial z})^2 + (v_{ni}+v_{nn})(\frac{\partial V_{nz}}{\partial z})^2\right]dr$$

From the velocity profile given above,

$$\frac{\partial V_{sz}}{\partial z} = 6\overline{V_{sz}}\frac{r_a+r_c-2r}{(r_a-r_c)^2}$$

So

$$\int_{r_c}^{r_a} r(\frac{\partial V_{sz}}{\partial z})^2 dr = \frac{36\overline{V}_{sz}^2}{(r_a-r_c)^4}\int_{r_c}^{r_a} r[(r_a+r_c)^2 - 4r(r_a+r_c) + 4r^2]dr$$

$$= \frac{36\overline{V}_{sz}^2}{(r_a-r_c)^4}\left[\frac{1}{2}(r_a+r_c)^2(r_a^2-r_c^2) - \frac{4}{3}(r_a+r_c)(r_a^3-r_c^3) + r_a^4 - r_c^4\right] = \frac{6\overline{V}_{sz}^2(r_a^2-r_c^2)}{(r_a-r_c)^2}$$

So,

$$\int_{r_c}^{r_a}\Phi dr = \frac{6(r_a^2-r_c^2)}{(r_a-r_c)^2}\left[(v_{ii}+v_{in})\overline{V}_{iz}^2 + (v_{ni}+v_{nn})\overline{V}_{nz}^2\right]$$

Neglecting the Hall and electron pressure terms, the axial and radial components of the electric field are given by

$$E_r = V_{iz}B_\theta + \frac{J_r}{\sigma} \qquad \text{(G.10)}$$

and

$$E_z = -V_{ir}B_\theta + \frac{J_z}{\sigma} \qquad \text{(G.11)}$$

So, the magnetic field equation is

$$\frac{\partial B_\theta}{\partial t} + \frac{\partial}{\partial z}\left[V_{iz}B_\theta - \frac{1}{\mu_0\sigma}\frac{\partial B_\theta}{\partial z}\right] - \frac{\partial}{\partial r}\left[-V_{ir}B_\theta + \frac{J_z}{\sigma}\right] = 0 \qquad \text{(G.12)}$$

Integrating over the cross section

$$\frac{\partial}{\partial t}\int_{r_c}^{r_a} B_\theta dr + \frac{\partial}{\partial z}\int_{r_c}^{r_a} V_{iz}B_\theta dr - V_{iz}B|_{r_a}\frac{dr_a}{dz} + V_{iz}B_\theta|_{r_c}\frac{dr_c}{dz}$$

$$-\frac{1}{\mu_0\sigma}\left[\frac{\partial}{\partial z}\int_{r_c}^{r_a}\frac{\partial B_\theta}{\partial z}dr - \frac{\partial B_\theta}{\partial z}|_{r_a}\frac{dr_a}{dz} + \frac{\partial B_\theta}{\partial z}\frac{dr_c}{dz}\right]$$

$$-\frac{\partial}{\partial z}\frac{1}{\mu_0}\sigma\int_{r_c}^{r_a}\frac{\partial B_\theta}{\partial z}dr + V_{ir}B_\theta|_{r_c}^{r_a} - \left(\frac{1}{r\mu_0\sigma}\frac{\partial r B_\theta}{\partial r}\right)_{r_c}^{r_a} = 0 \qquad \text{(G.13)}$$

Since there is no current at the electrodes parallel to the electrodes,

$$J_z(r_a, r_c) = -J_r(r_a, r_c)\frac{dr_{a,c}}{dz}$$

So

$$\frac{\partial B_\theta}{\partial z}|_{r_a}\frac{dr_a}{dz} - \frac{1}{r_a}\frac{\partial r B_\theta}{\partial r}|_{r_a} = 0.$$

Incorporating the assumptions that $rB_\theta = b(z)$, that there is no flow through the wall, and making the somewhat contradictory assumption that $V_{iz} = f(z)$,

$$\frac{\partial b}{\partial t}\ln\frac{r_a}{r_c} + \frac{\partial}{\partial z}\left(V_{iz}b\ln\frac{r_a}{r_c}\right) - \frac{1}{\mu_0\sigma}\frac{\partial}{\partial z}\left(\frac{\partial b}{\partial z}\ln\frac{r_a}{r_c}\right) - \frac{\partial}{\partial z}\left(\frac{1}{\mu_0\sigma}\right)\frac{\partial b}{\partial z}\ln\frac{r_a}{r_c} = 0 \qquad \text{(G.14)}$$

So, the magnetic field equation is given by

$$\ln\frac{r_a}{r_c}\frac{\partial b}{\partial t} + \frac{\partial}{\partial z}\left(V_{iz}b\ln\frac{r_a}{r_c}\right) - \frac{\partial}{\partial z}\left(\frac{1}{\mu_0\sigma}\right)\frac{\partial b}{\partial z}\ln\frac{r_a}{r_c} - \frac{1}{\mu_0\sigma}\frac{\partial b}{\partial z}\frac{d}{dz}(\ln\frac{r_a}{r_c}) = \frac{1}{\mu_0\sigma}\ln\frac{r_a}{r_c}\frac{\partial^2 b}{\partial z^2} \qquad \text{(G.15)}$$

Appendix H

Description of MPD1D

MPD1D, originally developed to simulate MPD thrusters, is a quasi one dimensional simulation of plasma flow in a channel consisting of concentric electrodes. The govering equations of the simulation were described in Appendix F. The input to the simulation, the output it produces, and the computer code which makes up the simulation are described herein.

H.1 Input

There are four types of input to the program. The input of most of the run parameters is done through a namelist file. The variables in the namelist file, called "parms.dat" are

dt the fluid time step, in seconds

rl the length of the electrodes, in meters

rano the inner radius of the anode at the inlet, in meters

rcat the outer radius of the cathode at the inlet, in meters

tfinal the total simulation time, in seconds

tplot the time between screen updates of errors, in seconds

current the total applied current, in amperes,

rmassflow the inlet mass flow, in kilograms/second

The solution from which the simulation starts can be set in either of two ways. If the file "micon.f" is included in the make file (oned.m) then the initial solution is set by the equations in that fortran file. If the file "micon2.f" is included in the make file, the initial solution is taken from the data files "*init.dat". To copy the last saved solution into the initial data files, run the shell file "init" (by typing "sh init" on a Unix system).

The third type of input is the geometry of the electrodes. Except for the data mentioned above, all of the geometry data, namely the interelectrode separation and the area at each axial location must be set in the fortran file "gridgen.f" by setting the variables RCAT and RANO, the cathode and anode radii at each axial location.

The fourth input is the number of simulation points, specified by the variable NZ in the file 'dims.f'. N_EQ in this file is the number of fluid equations being integrated.

H.2 Output

The main output of the program is 18 data files each containing the values of one of the flow properties at each axial location. Each output file consists of two lines, the first being the time at which the simulation ended, and the second the data for all the points. The files are written formatted. The name of all the files are a two letter prefix denoting the variable followed by ".dat". The two letter prefixes are

al ionization fraction

ar interelectrode area

bh azimuthal magnetic field strength

cr transverse current density

ef transverse electric field

la electron thermal conductivity

md local mass flow

mh mach number

pr fluid pressure

pt electrode potential difference

rh global mass density

sg electrical conductivity

te electron temperature

tg heavy species temperature

vi axial ion velocity

vn axial neutral velocity

vz axial global velocity

vs ion-ion viscosity coefficient

The program also outputs some diagnostic information to the screen at intervals specified in the input namelist file. This diagnostic information includes the maximum mass flow error and the number of the point at which it occurs, the average mass flow error, and the maximum courant number.

H.3 Flow Charts

The logical flow of the program is depicted in a series of flow charts. There are six flow charts altogether, showing the overall flow and the flow in various subroutines. Subroutine names are indicated in the parantheses following a brief description of what is done in the subroutine. The flow charts are shown in Figures H-1 - H-4.

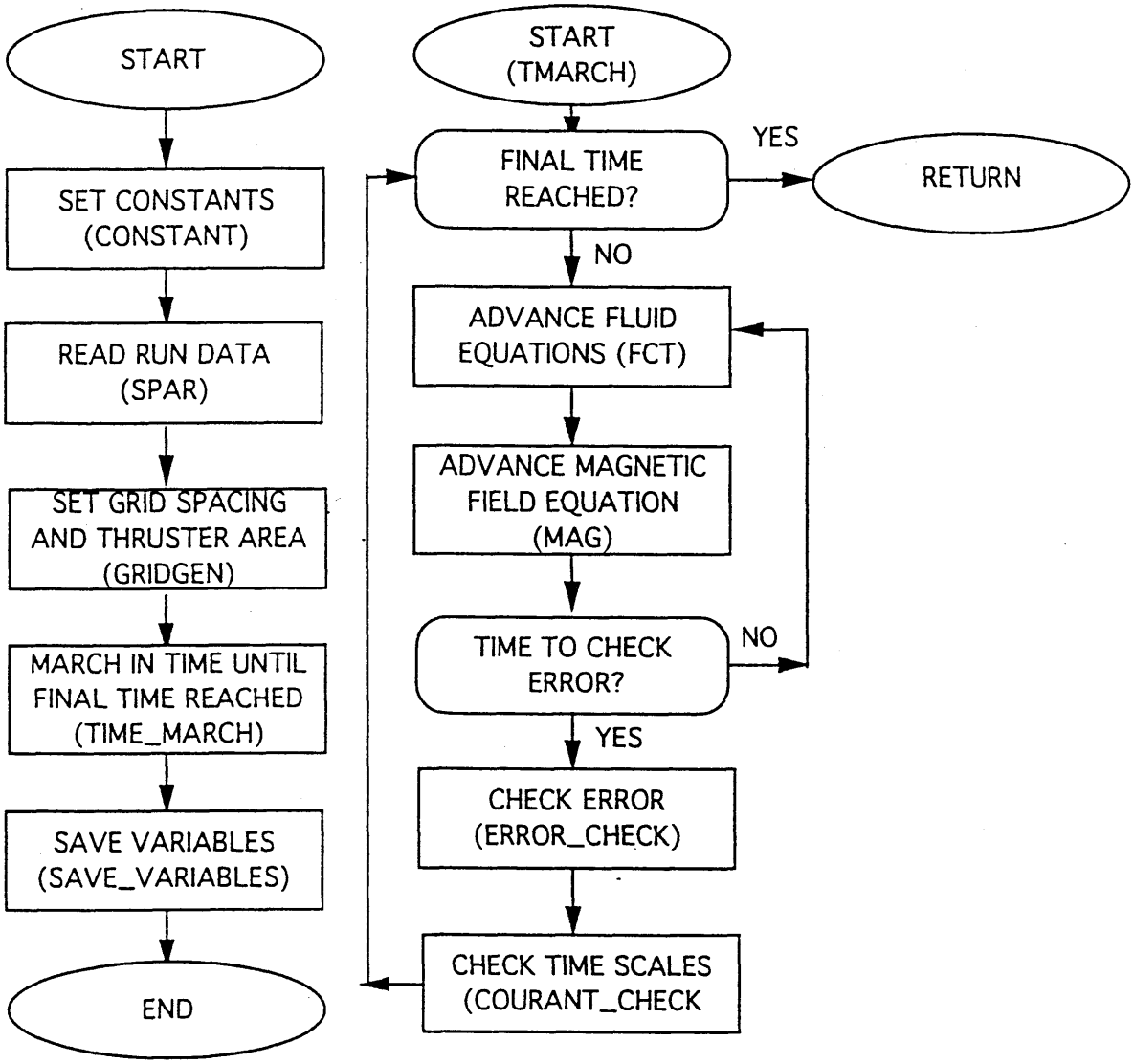

Figure H-1: MPD1D Flowchart, I

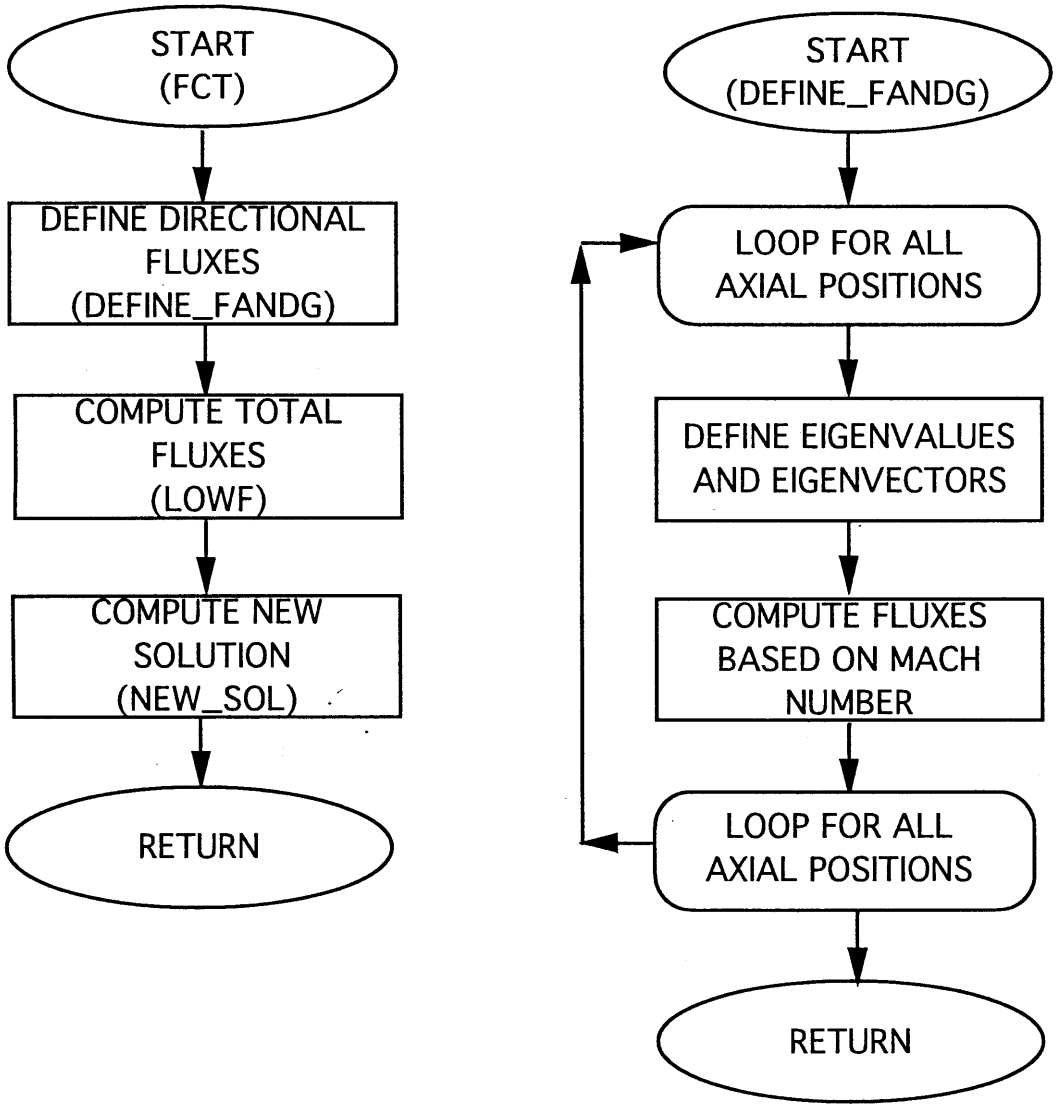

Figure H-2: MPD1D Flowchart, II

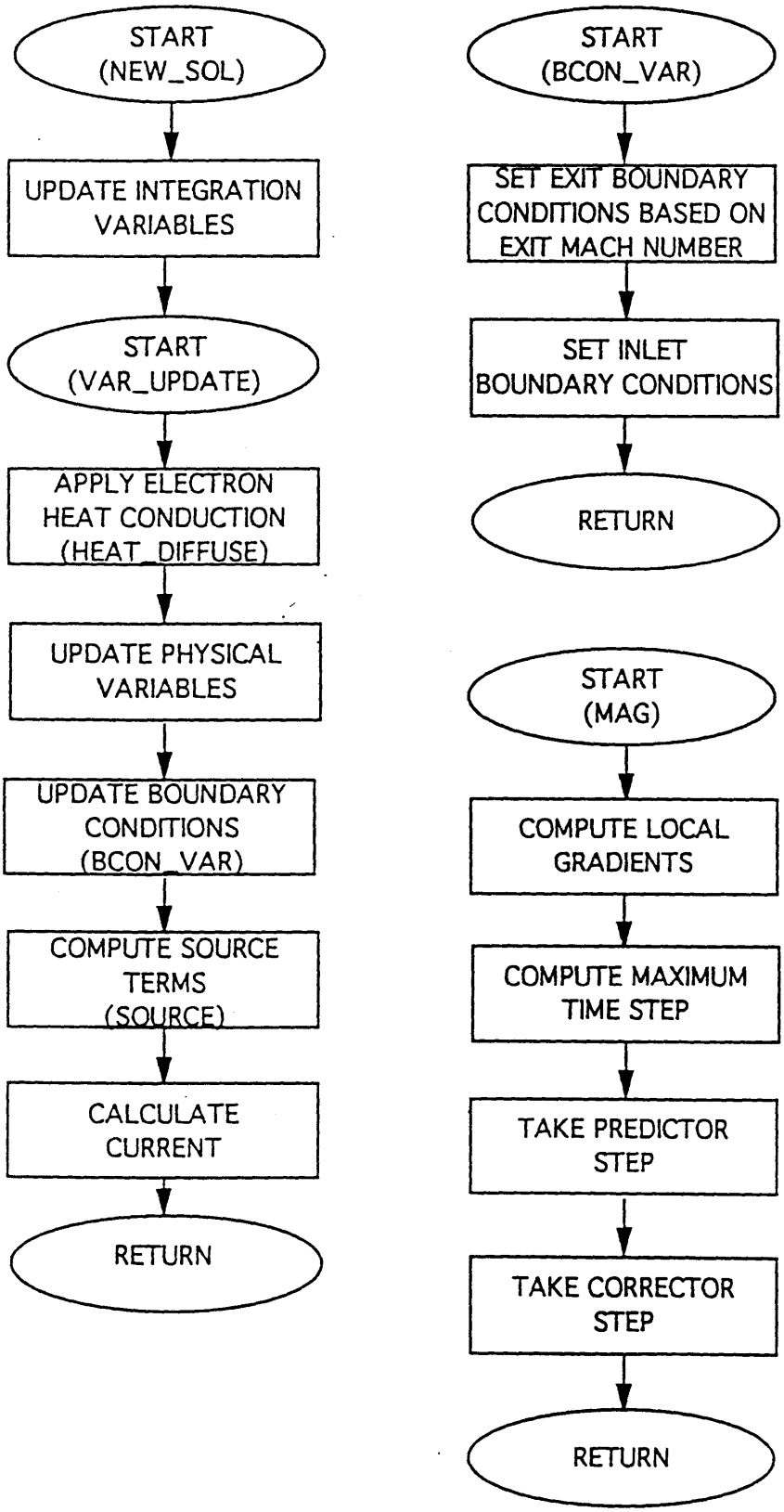

Figure H-3: MPD1D Flowchart, III

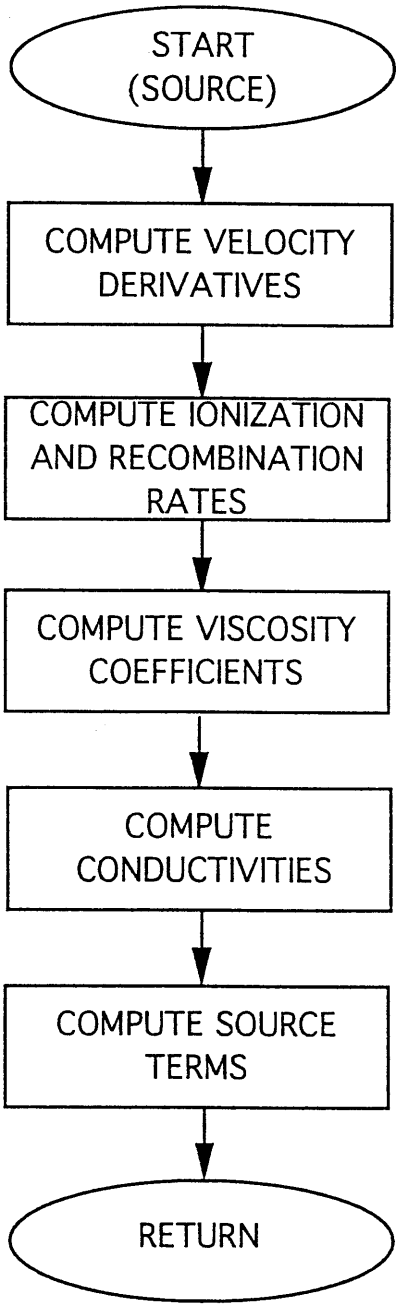

Figure H-4: MPD1D Flowchart, IV

H.4 Compiling, Linking, and Running the Code

The fortran files necessary for compiling and linking MPD1D are

constant.f Sets the physical constants.

echeck.f Checks and outputs the average and maximum mass flow errors.

dims.f Sets the number of axial points.

fct.f Calls subroutines to set the fluxes and compute the new solution.

gridgen.f Set the geometry and spatial step data.

mag2d1.f Updates the magnetic field equation.

main.f The main program.

mbcon.f Sets the inlet and exit boundary conditions.

mdfandg2.f Set the local upwind and downwind fluxes.

micon2.f Reads in the initial solution from the saved solution.

msvar.f Save the data.

mvupd.f Updates the physical variables based on the integration variables.

nsol.f Computes the new solution.

source2.f Computes the source terms and transport coefficients.

spar.f Reads in the namelist data.

tccheck.f Checks the time step limitations.

te1.f Updates the heat conduction part of the electron energy equation.

tmarch.f Marches the simulation forward in time.

lowf.f Computes the local total fluxes.

On Unix based systems the file "oned.m" is used to compile all of the necessary fortran files, producing object files labeled with the suffix ".o", and then link them together into the executable image "mpd1d". This is done by typing "make -f oned.m". The required fortran options can be specified in the make file. Typical options are "-g" to enable debugging, "-O2" to enable optimized compiling, "-r8" to use double precision variables, and "-static" to inhibit reinitialization of local subroutine variables.

Once the program is compiled, the run parameters, mainly the run time and fluid time step need to be set. The fluid time step should be set as high as possible without the simulation going unstable. Typical fluid times steps are on the order of 0.1 microseconds. Time to a converged solution is one the order of 1 to 0.1 milliseconds (starting from a reasonable solution). On a Decstation 5000, 10 microseconds of simulation time takes on the order of 0.5 to 1 minute. These numbers will vary substantially with varying input parameters.

Once the input parameters are set, the code can be run by typing "mpd1d". In order to have the screen output sent to a file, type "mpd1d > filename". In order to have the program run in the background, type "mpd1d > filename &". To set the priority low for long run time programs, type "nice +10 mpd1d > filename &". These commands may be substantially different for non-Unix based systems.

Once the program is finished, the data needed to start a new run from the current time can be set by typing "sh init". The data can be plotted using the graphics program described in the next section.

H.5 Plotting Results

For systems which have the plotting package Grafic, a plotting program called MAKEPLOT has been developed. In order to compile and link MAKEPLOT, the files "plot.m", "makeplot.f", and "proutines.f" are necessary. Typing "make -f plot.m" compiles and links the plotting program. The file "plot.m" may have to be changed slightly depending on the location of the Grafic library. Typing "makeplot" runs

the graphics program, which lists the variables which can be plotted and their index number. Type the index number and return to see the variable. In the plot window, the standard Grafic options are available. Type "x" to exit the plot and return to the variable list. The file "title.dat" gives the title printed at the top of each plot.

Bibliography

[1] D.A. Anderson, J.C. Tannehill, and R.H. Pletcher. *Computational Fluid Mechanics and Heat Transfer.* Hemisphere Publishing Corporation, New York, 1984.

[2] T. Ao and T Fujiwara. "Numerical and Experimental Study of an MPD Thruster". In *17th International Electric Propulsion Conference, Tokyo.* JSASS/AIAA/DGLR, July 1984. IEPC Paper No. 84-08.

[3] M. Auweter-Kurtz, H.L. Kurtz, H.O. Schrade, and P.C. Sleziona. "Numerical Modeling of the Flow Discharge in MPD Thrusters". *Journal of Propulsion and Power*, 5(1):49–55, January-February 1989.

[4] F.G. Bakhst, B. Ya. Moizhes, and A.B. Rybakov. "Critical Regime of a Plasma Accelerator". *Soviet Physics:Technical Physics*, 18(12):1613–1616, June 1974.

[5] J.A. Bittencourt. *Fundamentals of Plasma Physics.* Pergamon Press, Oxford, 1986.

[6] M.J. Boyle, K. E. Clark, and R. G. Jahn. "Flow Field Characteristics and Performance Limitations of Quasi-Steady Magnetoplasmadynamic Accelerators". In *AIAA 11th Electric Propulsion Conference, New Orleans*, March 1975. AIAA 75-414.

[7] K.V. Brushlinskii and A.I. Morozov. Calculation of Two-Dimensional Plasma Flows in Channels. In M.A. Leontovich, editor, *Reviews of Plasma Physics*, pages 105–198. Consultants Bureau, 1980. Volume 8.

[8] J.M. Burgers. *Flow Equations for Composite Gases.* Academic Press, New York, 1969.

[9] G. Caldo, E.Y. Choueiri, A.J. Kelly, and R.G. Jahn. "An MPD Code with Anomalous Transport ". In *22nd International Electric Propulsion Conference, Viareggio, Italy.* AIDAA/AIAA/DGLR/JSASS, Oct 1991. IEPC-91-102.

[10] G. Caldo, E.Y. Choueiri, A.J. Kelly, and R.G. Jahn. "Numerical Simulation of MPD Thruster Flows with Anomalous Transport ". In *28th Joint Propulsion Conference, Nashville, TN.* AIAA/SAE/ASME/ASEE, July 1992. AIAA-92-3738.

[11] J.M. Chanty and M. Martinez-Sanchez. "Two Dimensional Numerical Simulation of MPD Flows". In *19th International Electric Propulsion Conference, Colorado.* AIAA/DGLR/JSASS, MAY 1987. AIAA Paper No. 87-1090.

[12] J.M.G. Chanty. *Numerical Simulation of a Plasma Accelerator.* Master's thesis, Massachusetts Institute of Technology, September 1986.

[13] E.Y. Choueiri. *Electron-Ion Streaming Instabilities of an Electromagnetically Accelerated Plasma.* PhD thesis, Princeton University, October 1991.

[14] J. Fernandez de la Mora and R. Fernandez-Feria. "Two-Fluid Chapman-Enskog Theory for Binary Gas Mixtures". *Physics of Fluids*, 30(7):2063–2072, July 1987.

[15] J.H. Ferziger and H.G. Kaper. *Mathematical Theory of Transport Processes in Gases.* Americal Elsevier Publishing Company, New York, 1972.

[16] A.D. Gallimore. Report 1776.30 Dept. of Mechanical and Aerospace Engineering, Princeton University, 1991.

[17] A.D. Gallimore. *Anode Power Deposition in Coaxial MPD Thrusters.* PhD thesis, Princeton University, October 1992.

[18] A.D. Gallimore, A.J. Kelly, and R.G. Jahn. "Anode Power Deposition in Quasi-Steady MPD Thrusters". In *21st International Electric Propulsion Conference, Orlando, FL.* AIAA/DGLR/JSASS, July 1990. AIAA-90-2668.

[19] A.D. Gallimore, A.J. Kelly, and R.G. Jahn. "Anode Power Deposition in MPD Thrusters". In *22nd International Electric Propulsion Conference, Italy.* AIDAA/AIAA/DGLR/JSASS, October 1991. IEPC 91-125.

[20] A.D. Gallimore, R.M. Myers, A.J. Kelly, and R.G. Jahn. "Anode Power Deposition in an Applied-Field Segmented Anode MPD Thruster". In *27th Joint Propulsion Conference, Scacramento CA.* AIAA/SAE/ASME/ASEE, June 1991. AIAA-91-2343.

[21] M. Giles and E. Murman. Class Notes from Advanced Computational Fluid Dynamics, 1988.

[22] S.D. Grishin, A.K. Litvak, S.N. Ogordnikov, and V.N. Stepanov. "Intermediate-Power Steady-State Plasma Accelerator". *Soviet Physics Technical Physics*, 22(2):280–283, Feb. 1977.

[23] D.J. Heimerdinger. *An Approximate Two-Dimensional Analysis of an MPD Thruster.* Master's thesis, Massachusetts Institute of Technology, June 1984.

[24] D.J. Heimerdinger and M. Martinez-Sanchez. "Fluid Mechanics in a Magnetoplasmadynamic Thruster". In *20th International Electric Propulsion Conference, West Germany.* DGLR/AIAA/JSASS, October 1988. IEPC-88-039.

[25] D.J. Heimerdinger. *Fluid Mechanics in a Magnetoplasmadynamic Thruster.* PhD thesis, Massachusetts Institute of Technology, January 1988.

[26] D.J. Heimerdinger, D.B. Kilfoyle, and M. Martinez-Sanchez. "Experimental Characterization of Contoured Magnetoplasmadynamic Thrusters". In *24th Joint Propulsion Conference, Boston.* AIAA/ASME/SAE/ASEE, July 1988. AIAA Paper 88-3205.

[27] E. Hinnov and J.G. Hirschberg. "Electron-Ion Recombination in Dense Plasmas". *Physical Review*, 125(3):795–801, Feburary 1, 1962.

[28] J.O. Hirschfelder, C.F. Curtiss, and R.B. Bird. *Molecular Theory of Gases and Liquids.* John Wiley and Sons, Inc., New York, 1954.

[29] H. Hugel. "Effect of Self-Magnetic Forces on the Anode Mechanism of a High Discharge". *IEEE Transactions of Plasma Science*, PS-8(4):437–442, December 1980.

[30] D.B. Kilfoyle, M. Martinez-Sanchez, D.J. Heimerdinger, and E.J. Sheppard. "Spectroscopic Investigation of the Exit Plane of an MPD Thruster". In *20th International Electric Propulsion Conference, West Germany.* DGLR/AIAA/JSASS, October 1988. IEPC-88-027.

[31] D.Q. King. *Magnetoplasmadynamic Channel Flow for Design of Coaxial MPD Thrusters.* PhD thesis, Princeton University, December 1981.

[32] A. Ya. Kislov, P.E. Kovrov, A.I. Morozov, G.N. Tilinin, L.G. Tokarev, G. Ya Schepkin, A.K. Vinogadova, and Yu. P. Donzov. "Experimental Study of Current and Potential Distributions Between Coaxial Electrodes in a Quasi-Steady-State High Current Gas Discharge". In *Proceedings of the Eighth International Conference on Phenomena in Ionized Gases*, 1967. Panel 3.1.11.

[33] A. Ya. Kislov, A.I. Morozov, and G.N. Tilinin. "Distribution of Potential in a Quasistationary Coaxial Plasma Injector". *Soviet Physics Technical Physics*, 13(6):736–738, Dec. 1968.

[34] A.G. Korsun. "Current Limiting by Self Magnetic Field in a Plasma Accelerator". *Soviet Physics Technical Physics*, 19(1):124–126, July 1974.

[35] P.E. Kovrov, A.I. Morozov, L.G. Tokarev, and G. Ya. Shchepkin. "Magnetic Field Distribution in a Coaxial Plasma Injector". *Soviet Physics "Doklady"*, 12:155–157, 1967.

[36] Y. Kunii and K. Kuriki. "Multipole MPD Arcjet". In *18th International Electric Propulsion Conference, Virginia.* AIAA/DGLR/JSASS, September 1985. AIAA Paper 85-2055.

[37] K. Kuriki, M. Onishi, and S. Morimoto. "Thrust Measurement of K III MPD Arcjet". In *15th International Electric Propulsion Conference, Las Vegas, Nevada.* AIAA/JSASS/DGLR, April 1981. AIAA Paper 81-0683.

[38] K. Kuriki, Y. Kunii, and Y. Shimizu. "Idealized Model for Plasma Acceleration in an MHD Channel". *AIAA Journal*, 21(3):322–326, March 1983.

[39] M.R. LaPointe. "Numerical Simulation of Self-Field MPD Thrusters". In *27th Joint Propulsion Conference, Sacramento CA.* AIAA/SAE/ASME/ASEE, June 1991. AIAA-91-2341.

[40] M.R. LaPointe. "Numerical Simulation of Geometric Scale Effects in Cylndrical Self-Field MPD Thrusters". In *28th Joint Propulsion Conference, Nashville TN.* AIAA/SAE/ASME/ASEE, July 1992. AIAA-92-3297.

[41] J.L. Lawless and V.V Subramaniam. "Theory of Onset in Magnetoplasmadynamic Thrusters". *Journal of Propulsion and Power*, 3(2):121–127, March-April 1987.

[42] G. Lefever-Button and V.V. Subramaniam. "Quasi One-Dimensional MPD Flows". In *22nd International Electric Propulsion Conference, Viareggio, Italy.* AIDAA/AIAA/JSASS/DGLR, Oct. 1991. IEPC 91-061.

[43] M.A. Lieberman and A.L. Velikovich. *Physics of Shock Waves in Gases and Plasmas.* Springer-Verlag, Berlin, 1986.

[44] M. Martinez-Sanchez. Factors for MPD Thrusters. Annual Report 83-0035A, AFOSR, 1984.

[45] M. Martinez-Sanchez. "Structure of Self Field Accelerated Plasma Flows". *Journal of Propulsion and Power*, 7(1):56–64, January-February 1991.

[46] P.G. Mikellides, P.J. Turchi, and N.F. Roderick. "Application of the MACH2 Code to Magnetoplasmadynamic Arcjets". In *28th Joint Propulsion Conference, Nashville, TN.* AIAA/SAE/ASME/ASEE, July 1992. AIAA-92-3740.

[47] S. Miller. *Viscous and Diffusive Effects in Magnetoplasmadynamic Flows.* Master's thesis, Massachusetts Institute of Technology, June 1990.

[48] S. Miller and M. Martinez-Sanchez. "Viscous and Diffusive Effects in MPD Flows". In *21st International Electric Propulsion Conference, Orlando, FL.* AIAA/DGLR/JSASS, 1990. AIAA-90-2686.

[49] S. Miller and M. Martinez-Sanchez. "Viscous and Diffusive Effects in Electrothermal and MPD Arcjet Thrusters". In *22nd International Electric Propulsion Conference, Viareggio, Italy.* AIDAA/AIAA/DGLR/JSASS, 1991. IEPC-91-060.

[50] H. Minakuchi and K. Kuriki. "Magnetoplasmadynamic Analysis of Plasma Acceleration". In *17th International Electric Propulsion Conference, Japan.* AIAA/DGLR/JSASS, 1984. IEPC-84-06.

[51] M. Mitchner and C. Kruger. *Partially Ionized Gases.* John Wiley and Sons, New York, 1973.

[52] A.I. Morozov, K.V. Brushlinski, N.I. Gerlach, A.P. Shubin, and I.V. Kurchatov. "Theoretical and Numerical Analysis of Physical Processes in a Stationary High Current Gas Discharge between the Coaxial Electrodes". In *Proceedings of the Eighth International Conference on Phenomena in Ionized Gases*, 1967. Panel 3.1.11.

[53] E.H. Niewood. *Transient One Dimensional Numerical Simulation of Magnetoplasmadynamic Thrusters.* Master's thesis, Massachusetts Institute of Technology, February 1989.

[54] E.H. Niewood and M. Martinez-Sanchez. "Preliminary Design of a Dense Plasma Gun". Contractor report, Physical Sciences Inc., December 1992.

[55] E.H. Niewood and M. Martinez-Sanchez. "Quasi One Dimensional Numerical Simulation of Magnetoplasmadynamic Thrusters". *Journal of Propulsion and Power*, 8(5):1031–1039, Sept.-Oct. 1992.

[56] W.T. Park and D.I. Choi. "Two Dimensional Model of the Plasma Thruster". *Journal of Propulsion and Power*, 4(2):127–132, March-April 1988.

[57] J.C. Preble. *Magnetoplasmadynamic Thrusters: A Model of an Electrothermal Instabilty.* Master's thesis, Massachusetts Institute of Technology, May 1990.

[58] V.V. Rusanov. "The Calculation of the Interaction of Non-Stationary Shock Waves and Obstacles". *Zhur. Vychislitel'noi Mathematicheskoi Fiziki*, 1(2):267–279, 1961.

[59] E. Sheppard. Doctoral Thesis Research.

[60] T. Shoji and I. Kimura. "Analytical Study on the Influence of Nonequilibrium Ionization for Current Flow Pattern and Flow Field fo MPD Arcjets". In *21st International Electric Propulsion Conference, Orlando, FL.* AIAA/DGLR/JSASS, July 1990. AIAA Paper 90-2609.

[61] A.P. Shubin. "Dynamic Nature of Critical Regimes in Steady-State High-Current Plasma Accelerators". *Soviet Journal of Plasma Physics*, 2(1):18–21, Jan.-Feb. 1976.

[62] P.C. Sleziona, M. Auweter-Kurtz, and H.O. Schrade. "Numerical Codes for Cylindrical MPD Thrusters". In *20th International Electric Propulsion Conference, West Germany.* DGLR/AIAA/JSASS, October 1988. AIAA Paper 88-038.

[63] P.C. Sleziona, M. Auweter-Kurtz, and H.O. Schrade. "Numerical Evaluation of MPD Thrusters". In *21st International Electric Propulsion Conference, Orlando, Florida.* AIAA/DGLR/JSASS, July 1990. AIAA Paper 90-2602.

[64] P.C. Sleziona, M. Auweter-Kurtz, and H.O. Schrade. "MPD Thruster Calculation Considering High Ionization Modes". In *22nd International Electric Propul-*

sion Conference, Viareggio, Italy. AIDAA/AIAA/DGLR/JSASS, Oct. 1991. IEPC-91-087.

[65] P.C. Sleziona, M. Auweter-Kurtz, and H.O. Schrade. "Numerical Calculation of Nozzle Type and Cylindrical MPD Thrusters". In *28th Joint Propulsion Conference, Nashville, TN.* AIAA/SAE/ASME/ASEE, July 1992. AIAA-92-3296.

[66] P.C. Sleziona, M. Auweter-Kurtz, H.O. Schrade, and T. Wegmann. "Comparison of Numerical and Experimental Investigation of Nozzle Type MPD Accelerators". In *21st International Electric Propulsion Conference, Orlando, Florida.* AIAA/DGLR/JSASS, July 1990. AIAA Paper 90-2663.

[67] J.L. Steger and R.F. Warming. "Flux Vector Splitting of the Inviscid Gasdynamic Equations with Applicaton to Finite Difference Methods". *Journal of Computational Physics*, 40:263–293, 1981.

[68] V.V. Subramaniam and J.L. Lawless. "Onset in Magnetoplasmadynamic Thrusters with Finite-Rate Ionization". *Journal of Propulsion and Power*, 4(6):526–532, November-December 1988.

[69] K.W. Thompson. "Time-Dependent Boundary Conditions for Hyperbolic Systems". *Journal of Computational Physics*, 89(2):439–461, August 1990.

[70] P. A. Thompson. *Compressible-Fluid Dynamics.* Advanced Engineering Series, 1988.

[71] L.I. Vainberg, G.A. Lyubimov, and G.G. Smolin. "High-Current Discharge Effects and Anode Damage in an End-Fire Plasma Accelerator". *Soviet Physics Technical Physics*, 23(4):439–443, April 1978.